Graduate School ETD Form 9
(Revised 12/07)

PURDUE UNIVERSITY
GRADUATE SCHOOL
Thesis/Dissertation Acceptance

This is to certify that the thesis/dissertation prepared

By Christopher Ray Jamell

Entitled LATTICE AND MOMENTUM SPACE APPROACH TO BOUND STATES AND EXCITONIC CONDENSATION VIA USER FRIENDLY INTERFACES

For the degree of Doctor of Philosophy

Is approved by the final examining committee:

Dr. Yogesh Joglekar Chair	Dr. Ricardo Decca
Dr. B. D. Nageswara Rao	Dr. Ruihua Cheng
Dr. Jiangping Hu	

To the best of my knowledge and as understood by the student in the *Research Integrity and Copyright Disclaimer (Graduate School Form 20)*, this thesis/dissertation adheres to the provisions of Purdue University's "Policy on Integrity in Research" and the use of copyrighted material.

Approved by Major Professor(s): Dr. Yogesh Joglekar

Approved by: Dr. Ricardo Decca 09/01/2010
Head of the Graduate Program Date

Graduate School Form 20
(Revised 1/10)

PURDUE UNIVERSITY
GRADUATE SCHOOL

Research Integrity and Copyright Disclaimer

Title of Thesis/Dissertation:
LATTICE AND MOMENTUM SPACE APPROACH TO BOUND STATES AND EXCITONIC CONDENSATION VIA USER FRIENDLY INTERFACES

For the degree of Doctor of Philosophy

I certify that in the preparation of this thesis, I have observed the provisions of *Purdue University Teaching, Research, and Outreach Policy on Research Misconduct (VIII.3.1)*, October 1, 2008.*

Further, I certify that this work is free of plagiarism and all materials appearing in this thesis/dissertation have been properly quoted and attributed.

I certify that all copyrighted material incorporated into this thesis/dissertation is in compliance with the United States' copyright law and that I have received written permission from the copyright owners for my use of their work, which is beyond the scope of the law. I agree to indemnify and save harmless Purdue University from any and all claims that may be asserted or that may arise from any copyright violation.

Christopher Ray Jamell
Printed Name and Signature of Candidate

10/01/2010
Date (month/day/year)

*Located at http://www.purdue.edu/policies/pages/teach_res_outreach/viii_3_1.html

LATTICE AND MOMENTUM SPACE APPROACH TO BOUND STATES AND EXCITONIC CONDENSATION VIA USER FRIENDLY INTERFACES

A Dissertation

Submitted to the Faculty

of

Purdue University

by

Christopher Ray Jamell

In Partial Fulfillment of the

Requirements for the Degree

of

Doctor of Philosophy

December 2010

Purdue University

Indianapolis, Indiana

To my mother, Patricia Jamell, who has supported everything I have done.

ACKNOWLEDGMENTS

The first person that I need to thank is of course my advisor Dr. Yogesh Joglekar. His door has always been open to me, even when it is the tenth time I have been in his office that day, and he has always taken the time to think about my questions and give me the best answers he can.

I would also like to thank Dr. Ricardo Decca for not only taking the time to serve on my committee but for also being my instructor for my first physics course. He also had to put up with me stopping by his office on multiple occasions to answer my questions.

I feel very priviledged to have had the opportunity to work with both Yogesh and Ricardo.

I would also like to thank both Dr. B.D. Nageswara Rao and Dr. Ruihua Cheng for not only serving on my committee but for also having been my teachers. And I must also thank Dr. Jiangping Hu for being on my committee and making the drive from West Lafayette.

Finally, I would like to thank all my teachers, I have enjoyed my time here at IUPUI and I believe that I am at least marginally smarter than I was before I started this journey.

TABLE OF CONTENTS

LIST OF FIGURES

Figure Page

Figure Page

ABSTRACT

Jamell, Christopher Ray Ph.D., Purdue University, December 2010. Lattice and Momentum Space Approach to Bound States and Excitonic Condensation via User Friendly Interfaces. Major Professor: Yogesh N. Joglekar.

In this thesis, we focus on two broad categories of problems, exciton condensation and bound states, and two complimentary approaches, real and momentum space, to solve these problems. In chapter 2 we begin by developing the self-consistent mean field equations, in momentum space, used to calculate exciton condensation in semiconductor heterostructures/double quantum wells and graphene. In the double quantum well case, where we have one layer containing electrons and the other layer with holes separated by a distance d, we extend the analytical solution to the two dimensional hydrogen atom in order to provide a semi-quantitative measure of when a system of excitons can be considered dilute. Next we focus on the problem of electron-electron screening, using the random phase approximation, in double layer graphene. The literature contains calculations showing that when screening is not taken into account the temperature at which excitons in double layer graphene condense is approximately room temperature. Also in the literature is a calculation showing that under certain assumptions the transition temperature is approximately mK. The essential result is that the condensate is exponentially suppressed by the number of electron species in the system. Our mean field calculations show that the condensate, is in fact, not exponentially suppressed.

Next, in chapter 3, we show the use of momentum space to solve the Schrödinger equation for a class of potentials that are not usually a part of a quantum mechanics courses. Our approach avoids the typical pitfalls that exist when one tries to discretize the real space Schrödinger equation. This technique widens the number of problems

that can presented in an introductory quantum mechanics course while at the same time, because of the ease of its implementation, provides a simple introduction to numerical techniques and programming in general to students. We have furthered this idea by creating a modular program that allows students to choose the potential they wish to solve for while abstracting away the details of how the solution is found.

In chapter 4 we revisit the single exciton and exciton condensation in double layer graphene problems through the use of real space lattice models. In the first section, we once again develop the equations needed to solve the problem of exciton condensation in a double layer graphene system. In addition to this we show that by using this technique, we find that for a non-interacting system with a finite non-zero tunneling between the layers that the on-site exciton density is proportional to the tunneling amplitude. The second section returns to the single exciton problem. In agreement with our momentum space calculations, we find that as the layer separation distance is increased the bound state wave function broadens. Finally, an interesting consequence of the lattice model is explored briefly. We show that for a system containing an electron in a periodic potential, there exists a bound state for both an attractive as well as repulsive potential. The bound state for the repulsive potential has as its energy $-E_0$ where E_0 is the ground state energy of the attractive potential with the same strength.

1. INTRODUCTION

Knowing others is wisdom, knowing yourself is enlightenment.

(Lao Tzu)

The majority of work presented in this thesis deals with trying to develop a better theoretical understanding of exciton condensation. To achieve this goal we must know what an exciton is, which will be detailed in the next chapter, and we need to develop a basic understanding of what a Bose-Einstein condensate (BEC) is which we will do now.

The theory of Bose-Einstein condensation was developed in 1924 by S. Bose [1] and extended by A. Einstein [2] in 1925. Bose was interested in determining when two photons could be considered indistinguishable. In his work he developed what we now call Bose statistics. After having his paper rejected for publication, Bose turned to Einstein for help. Following the publication of Bose's paper, Einstein became interested in the problem of applying Bose statistics to an ideal gas of atoms. What Einstein found is that for sufficiently low temperatures, a macroscopically large number of the atoms in the gas would all collect in the ground state. This collection of atoms is what we now refer to as a BEC. It was not until 75 years after these theoretical predictions that physicists were first able to experimentally observe a BEC. In 1995 Eric Cornell, Carl Wieman and associates experimentally created a BEC which consisted of approximately two thousand rubidium-87 atoms which were cooled to below 170 nK [3]. Shortly thereafter a group led by Wolfgang Ketterle at the Massachusetts Institute of Technology created a condensate out of sodium-23 [4] and another group at Rice University led by Randall Hulet created a condensate out of lithium-7 atoms [5]. The following year in 1998 Grettak *et.al.* were able to create a BEC out of atomic hydrogen [6]. In the intervening years there have been several experiments that have been performed in order to record the time evolution of the BEC in real time [7] [8] [9]. Although the phenomenon of BEC is purely a consequence of the quantum statistics of bosons the atom-atom interactions play an important role in determining most of the properties of the condensate which makes it desirable to be able to control both the magnitude and sign of the interaction. For a strong repulsive interaction the resulting BEC is stable and its size and shape is determined by the interaction energy of the gas where on the other hand an attractive interaction leads to a metastable BEC where the number of atoms is limited to a small critical value. However, the nature of the interaction is usually fixed by the choice of the type of atom used in the experiment. One method that can be used to achieve this control is to use the strong variation of the scattering length with magnetic field that occurs in the vicinity of a Feshbach resonance [10]. The use of a Feshbach resonance was key to the Wieman group being able to create a condensate of over 10^5 rubidium-85 atoms since the zero field scattering length for these types of atoms is -20 nm which would limit the condensate to around just 80 atoms [11]. Furthermore by taking advantage of the Feshbach resonance several groups have been able to experimentally observe bright solitons in a condensate of lithium-7 atoms [12] [13]. Additionally Bragg scattering experiments have been performed by Phillips *et al.* [14] and Ketterle *et al.* [9]. By using diffraction experiments it has been shown that the momentum distribution of a trapped condensate is linked to the size of the condensate by the Heisenberg uncertainty relation [15]. These are just a very small number of the many experiments that have been performed on BECs since their discovery.

To better understand the phenomenon of BEC we will loosely follow the presentation by Phillips [16] and start with the grand canonical partition function, $\mathcal{Z}$, for a non-interacting Bose gas which is given by

$$\mathcal{Z} = \prod_k \mathcal{Z}_k = \prod_k \sum_{n_k} e^{-n_k \beta (E_k - \mu)} \tag{1.1}$$

where $\beta = 1/k_b T$ with k_b being the Boltzman constant and T is the temperature, E_k is the energy of state $|\mathbf{k}\rangle$, μ is the chemical potential, and n_k is the degeneracy of state $|\mathbf{k}\rangle$. For bosons the occupations n_k are unrestricted giving

$$\mathcal{Z}_k = 1 + e^{-\beta(E_k-\mu)} + e^{-2\beta(E_k-\mu)} + \cdots = \frac{1}{1-e^{-\beta(E_k-\mu)}}. \tag{1.2}$$

The average number of particles in a given state $|\mathbf{k}\rangle$ can not be negative which requires $E_k - \mu \geq 0$ which implies $\mu \leq 0$ for $E_0 = 0$. The grand canonical potential, Ω, is defined as

$$\Omega = -\frac{1}{\beta}\ln \mathcal{Z} = \frac{1}{\beta}\sum_k \ln\left(1 - e^{-\beta(E_k-\mu)}\right) \tag{1.3}$$

which, if the energy level spacings of the system is small enough we can write

$$\Omega = \frac{1}{\beta}\int_0^\infty dE g_D(E)\ln\left(1-e^{-\beta(E-\mu)}\right) + \frac{1}{\beta}\ln\left(1-e^{\beta\mu}\right) \tag{1.4}$$

where L^D is the volume of the system and $g_D(E)$ is the density of states given by

$$g_D(E) = \left(\frac{L}{2\pi}\right)^D \frac{d^D\mathbf{k}}{dE} = \left(\frac{L}{2\pi}\right)^D 2^{D-1}\pi k^{D-1}\frac{dk}{dE} = \frac{L^D}{2\pi^{D-1}\nu A_\nu^{D/\nu}}E^{D/\nu-1}, \tag{1.5}$$

where $E = A_\nu|\mathbf{k}|^\nu$. In Eq. (1.4) we have explicitly retained the E_0 portion by including the second term since this would be omitted in the integral due to the fact that the density of states at $k = 0$ is zero. Substituting in the density of states, for a quadratically dispersing particle, we have

$$\Omega = \frac{2^{D/2-2}L^D m^{D/2}}{\pi^{D-1}\hbar^D\beta}\int_0^\infty dE\, E^{D/2-1}\ln\left(1-e^{-\beta(E-\mu)}\right) + \frac{1}{\beta}\ln\left(1-e^{\beta\mu}\right). \tag{1.6}$$

Using integration by parts we can write Ω as

$$\Omega = -\frac{2^{D/2-1}L^D m^{D/2}}{3\pi^{D-1}\hbar^D}\int_0^\infty dE\frac{E^{D/2}}{e^{-\beta(E-\mu)}-1} + \frac{1}{\beta}\ln\left(1-e^{\beta\mu}\right). \tag{1.7}$$

The Riemann zeta function is defined as

$$\zeta_n(z) = \frac{1}{\Gamma(n)} \int_0^\infty dx \frac{x^{n-1}}{z^{-1}e^x - 1} \tag{1.8}$$

where $z = e^{\beta\mu}$ is the fugacity or activity and $\Gamma(n)$ is the gamma function, which we can use to arrive at the final form for the grand canonical potential by substituting $x = \beta E$ which gives

$$\Omega = -\frac{L^D}{\lambda_D^3 \beta} \zeta_{\frac{D+2}{2}}(z) + \frac{1}{\beta} \ln(1-z). \tag{1.9}$$

where $\lambda_D = \frac{\pi^{D/3-1/2}\hbar^{D/3}\beta^{1/2}}{2^{D/6-1}m^{D/6}}$ is the thermal de Broglie wavelength. λ_D can be regarded as the position uncertainty associated with the thermal momentum distribution [17]. As the temperature is lowered λ_D increases and when its spread is comparable to the inter-atomic distances the atomic wavepackets overlap which gives rise to the BEC. Using the relationship between the total number of particles, N, and Ω we find

$$N = -\frac{\partial \Omega}{\partial \mu} = \frac{L^D}{\lambda_D^3} \zeta_{\frac{D}{2}}(z) + \frac{z}{1-z} = N_{ex} + N_0, \tag{1.10}$$

where N_{ex} is the number of particles in excited states and N_0 are the number of particles in the lowest energy state. Rewriting Eq. (1.10) as

$$\frac{N_0}{N} = 1 - \frac{N_{ex}}{N} \tag{1.11}$$

and considering the gas in the thermodynamic limit, $N \to \infty, L^D \to \infty, N/L^D = \rho =$ constant, we have for $z = 1$ an equation which is indeterminate. Otherwise if $z \neq 1$ there is a finite occupation of the ground state and in the limit $N \to \infty$ the ratio N_0/N goes to zero. Remembering from earlier that $0 \leq z \leq 1$ and knowing that $g_{\frac{D+2}{2}}(z)$ is a monotonically increasing function of z the maximum occupation of the excited states, N_{ex}^{max}, is given by

$$N_{ex}^{max} = \frac{L^D}{\lambda_D^3} \zeta_{\frac{D}{2}}(1). \tag{1.12}$$

Using this maximum occupation we can determine the fraction of atoms in the ground state

$$\frac{N_0}{N} = 1 - \frac{\zeta_{\frac{D}{2}}(1)}{\lambda_D^3}\frac{L^D}{N} = 1 - \frac{\zeta_{\frac{D}{2}}(1)}{\rho}\frac{1}{\lambda_D^3} = 1 - \left(\frac{T}{T_c}\right)^{3/2}, \tag{1.13}$$

which shows that as T moves below T_c the fractional occupation of the ground state increases until $T = 0$ where all atoms are in the ground state. The critical temperature is thus given by

$$T_c = \left(\frac{\pi^{D-3/2}\hbar^D \rho}{2^{D/2-3}\zeta_{\frac{D}{2}}(1) m^{D/2} k_b^{3/2}}\right)^{2/3}. \tag{1.14}$$

One important consequence of the form of T_c is that since it depends on $1/\zeta_{\frac{D}{2}}$, which we have seen is divergent for an argument that is less or equal to one, there can be no non-zero critical temperature for a system of dimension less than or equal to two. To examine the ground state occupancy let us look at $\mathcal{Z}_0$ from Eq. (1.2) when the chemical potential μ approaches zero

$$\mathcal{Z}_0 = \frac{1}{1 - 1 - \beta\mu - \cdots} \approx -\frac{1}{\beta\mu} = \frac{k_b T}{\mu} \gg 1 \tag{1.15}$$

where we have used the fact that T is nonzero and $\mu \to 0^-$. Equation(1.15) shows that for $\mu \to 0^-$ the occupation of the ground state goes to infinity, $\mathcal{Z}_0 \to \infty$. This tells us that once the number of particles in the gas exceeds the maximum number of particles in the excited states, N_{ex}^{max}, the remaining particles can all be accommodated in the ground state. If we check on the number of particles in the first excited state, $\mathcal{Z}_1$, we find

$$\mathcal{Z}_1 = \frac{1}{\beta\epsilon_1 - \beta\mu} \approx \frac{1}{\beta\epsilon_1 + \mathcal{Z}_0^{-1}} < \frac{k_b T}{E_1} \tag{1.16}$$

which means that the number of particles in the first excited state is finite and relatively small when compared to the ground state. This implies that *all* of the excess particles are in the ground state. This is the manifestation of Bose-Einstein condensation.

The outline of this thesis is as follows. In Chapter 2 we discuss the application of Bose-Einstein condensation to the problem of excitons in double layer systems. The treatment of this problem involves the derivation of a set of self-consistent mean field equations in momentum space. These equations are obtained for double layer systems in which the carriers within a layer are quadratically dispersing (double quantum well) or linearly dispersing (graphene). In addition to the standard mean field equations for these systems, a first attempt is made to understand the role of electron-electron screening in the suppression of the condensate using the random phase approximation. A brief look at the program used to solve this problem is given in Appendix A. In Chapter 3 we present the use of the Schrödinger equation in momentum space as it relates to the pedagogy of quantum mechanics for late undergraduate/early graduate students in physics. To further this discussion a modular computer program was designed to allow students an easy transition into computer programming while at the same time broadening the class of potentials that can be used in a quantum mechanics course. This program is shown in Appendix B. In Chapter 4 we provide a programmatic means, shown in Appendix C, for approaching both the problem of exciton condensation from Chapter 2 and finding solutions to the Schrödinger equation presented in Chapter 3 using a real space lattice model. Finally in Chapter 5 we present a short summary of the work presented herein.

Throughout this work we will present a strong focus on the use of computers for two main purposes. The first, and most obvious, is the use of the computer to numerically solve the problems at hand. Without the use of a computer the solutions presented in this work would be, for all intents and purposes, impossible to find by hand. Secondly through the development of a graphical user interface for the problems presented in this thesis it is possible for students who are not yet at a point where they can understand or code the equations needed are able to learn or participate in this research by gathering and analyzing data in a much more intuitive and easily understood manner than would be possible through a command line program.

2. EXCITON CONDENSATION IN MOMENTUM SPACE

> From a certain temperature on, the molecules 'condense' without attractive forces; that is, they accumulate at zero velocity. The theory is pretty, but is there some truth in it. (Albert Einstein)

A crystalline solid is a solid whose constituent atoms are arranged in an orderly and repeating pattern in space. There a several types of defects that are present in most, if not all, crystals. Some of these include: vacancies which are positions on the lattice that are usually occupied but are vacant, interstitials are atoms that occupy positions in the lattice which are usually unoccupied, and substitutionals which are atoms that are chemically substituted at one or more lattice sites. All of the previously mentioned defects are physical defects. There is an additional defect that we are interested in here which has become known as an exciton.

An exciton is a quantum of electronic excitation energy traveling in the periodic structure of a crystal; it is electrically neutral and hence its movement through the crystal gives rise to the transportation of energy but not charge [18]. The idea of an exciton has been around for a fairly long time. It was first conceptualized by Yakov Frenkel in 1931 [19] as 'excitation waves' that result when a photon is absorbed in a crystal and transformed into an electronic excitation which is not confined to a particular atom in the crystal. Frenkel considered the case where you have a crystal of N identical atoms with small interatomic interaction as compared to the interaction between the core of an atom and its valence electrons. When one of the N atoms has an electron that is promoted to an excited state the resulting vacancy in the former valence shell is called a hole. Due to the relative weakness of the interaction between outer shell electrons and neighboring atoms the excited electron and hole form a bound pair which is tightly localized near the atom as depicted in Fig. 2.1.

Frenkel excitons are typically found in organic materials and have a binding energy of approximately 1 eV and a radius around 10 Å.

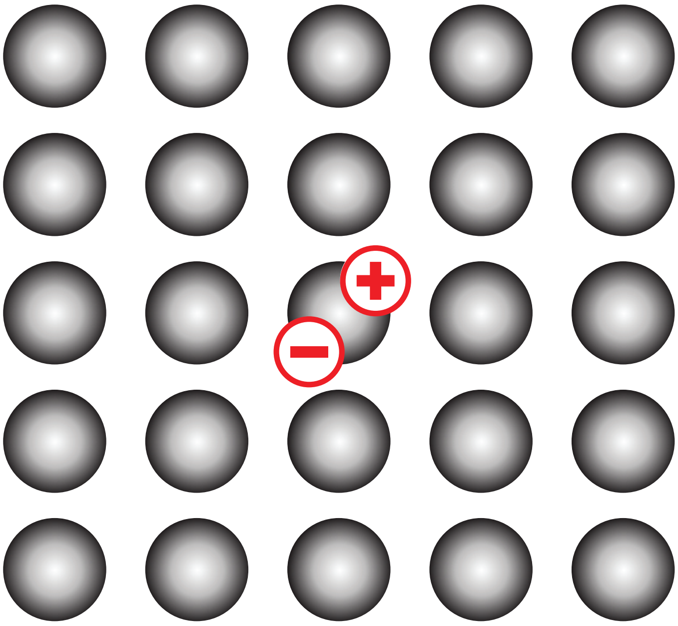

Fig. 2.1.: Diagram of a crystal containing a Frenkel exciton. The red plus represents the hole and the red minus represents the excited electron. For a Frenkel exciton the excited electron is tightly bound to an atom. The figure is not to scale.

At the opposite end from the Frenkel exciton we have the Wannier-Mott exciton. As with the Frenkel case we start with N identical atoms where one atom has an electron that is promoted to an excited state leaving behind a hole. But, in this case the interaction between valence electrons and neighboring atoms is relatively large so that the promoted electron is able to drift several lattice spacings away from its parent atom. Wannier excitons are typically found in semiconductors and have a binding energy of approximately 10 meV and a radius of around 100 Å as depicted in Fig. 2.2.

It is due to this large radius that we are able to employ the effective mass approximation (EMA) [20] [21] which is used in order to simplify the many body Schrödinger equation. In order to develop a basic understanding of the Wannier-Mott exciton we will follow the presentation in [22]. We begin with

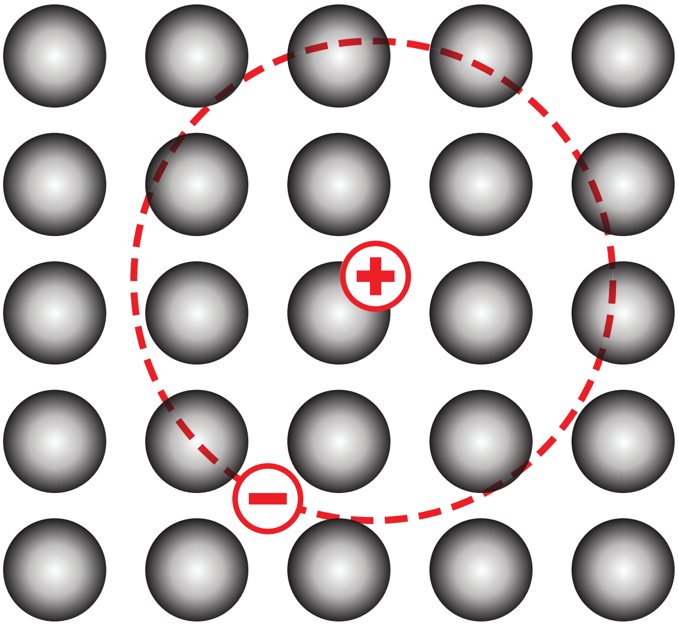

Fig. 2.2.: Diagram of a crystal containing a Wannier-Mott exciton. The red plus represents the hole and the red minus represents the excited electron. In contrast to the Frenkel case a Wannier-Mott exciton is more loosely bound to its parent atom and therefore has a larger orbital radius.

$$\left(-\frac{\hbar^2}{2m_e^*}\boldsymbol{\nabla}_e^2-\frac{\hbar^2}{2m_h^*}\boldsymbol{\nabla}_h^2-\frac{e^2}{\epsilon\mathbf{r}}\right)\boldsymbol{\Psi}_\alpha=E_\alpha\boldsymbol{\Psi}_\alpha \tag{2.1}$$

where m_e^* is the effective mass of the electron and m_h^* is the mass of the hole. The first term is the kinetic energy of the excited electron, the second term is the kinetic energy of the hole and the last term is their interaction. The simplifications used to arrive at Eq. (2.1) will be discussed in Sec. 2.1.1. We begin by separating Ψ_α as follows

$$\Psi_\alpha(\mathbf{R},\mathbf{r})=f_\alpha(\mathbf{R})g_\alpha(\mathbf{r}) \tag{2.2}$$

where $\mathbf{R}=\frac{1}{2}(\mathbf{r}_e+\mathbf{r}_h)$ and $\mathbf{r}=\mathbf{r}_e-\mathbf{r}_h$ are the average electron-hole coordinate and electron-hole separation, respectively. The gradient operators for $\mathbf{R}$ and $\mathbf{r}$ are $\boldsymbol{\nabla}_\mathbf{R}=\boldsymbol{\nabla}_e+\boldsymbol{\nabla}_h$ and $\boldsymbol{\nabla}_\mathbf{r}=\frac{1}{2}(\boldsymbol{\nabla}_e-\boldsymbol{\nabla}_h)$. When we transform into the new coordinates, Eq. (2.1) becomes

$$\left[\frac{1}{8}\left(\frac{1}{m_e^*}+\frac{1}{m_h^*}\right)p_{\mathbf{R}}^2-\frac{1}{2}\left(\frac{1}{m_e*}-\frac{1}{m_h^*}\right)\mathbf{p_R}\cdot\mathbf{p_r}\right.$$
$$\left.+\frac{1}{2}\left(\frac{1}{m_e^*}+\frac{1}{m_h^*}\right)p_{\mathbf{r}}^2-\frac{e^2}{\epsilon\mathbf{r}}\right]\Psi=E\Psi \quad (2.3)$$

where $\mathbf{p_R}=-i\hbar\boldsymbol{\nabla}_{\mathbf{R}}$ and $\mathbf{p_r}=-i\hbar\boldsymbol{\nabla}_{\mathbf{r}}$. Using $f(\mathbf{R})=e^{i\mathbf{K}\cdot\mathbf{R}}$ in Eq. (2.3)

$$\left[\frac{p_{\mathbf{r}}^2}{2\mu}-\frac{e^2}{\epsilon r_e}-\frac{\hbar}{2}\left(\frac{1}{m_h^*}-\frac{1}{m_e^*}\right)\mathbf{K}\cdot\mathbf{p_r}\right]g(\mathbf{r})=\left[E-\frac{1}{8\mu}\hbar^2\mathbf{K}^2\right] \quad (2.4)$$

where the reduced mass, μ, is defined by

$$\frac{1}{\mu}=\frac{1}{m_e^*}+\frac{1}{m_h^*}. \quad (2.5)$$

Next we apply the transform

$$g(\mathbf{r})=e^{i\alpha\mathbf{K}\cdot\mathbf{r}}G(\mathbf{r}) \quad (2.6)$$

in order to eliminate the $\mathbf{K}\cdot\mathbf{p_r}$ term in Eq. (2.4) we must require

$$\alpha=\frac{1}{2}\frac{m_e^*-m_h^*}{m_e^*+m_h^*} \quad (2.7)$$

Once this elimination is performed we find that G must satisfy the equation

$$\left(\frac{p_{\mathbf{r}}^2}{2\mu}-\frac{e^2}{\epsilon r}\right)G=\left[E-\frac{\hbar^2K^2}{2M}\right]G \quad (2.8)$$

where $M=m_e^*+m_h^*$. The solutions to Eq. (2.8) are the solutions to the hydrogen atom with effective Z of $1/\epsilon$ which means that for each value of $\mathbf{K}$ we have the following bound state energies

$$E_n(K)=-\frac{\mu e^4}{2\hbar^2\epsilon^2n^2}+\frac{\hbar^2\mathbf{K}^2}{2M}, \quad (2.9)$$

with the total wave function of the system being given by

$$\boldsymbol{\Psi}_{nlm}(\mathbf{K})=e^{i\mathbf{K}\cdot(\mathbf{R}+\alpha\mathbf{r})}G_{nlm}(\mathbf{r}). \quad (2.10)$$

where $\mathbf{R} + \alpha\mathbf{r}$ is equal to the center of mass position as expected.

Although the concept of an exciton has been around for over seventy years it wasn't until 2003 that researchers were, for the first time, able to track the motion of an exciton and a biexciton using near-field optical mapping [23]. Matsuda and his colleagues repeatedly flashed a 100 nm raised patch of gallium arsenide and recorded the light emissions when the resulting exciton and biexciton recombined. By imaging the same location several times before moving onto the next the researchers were able to build up a picture of the exciton and biexciton wave functions shown in Fig. 2.3.

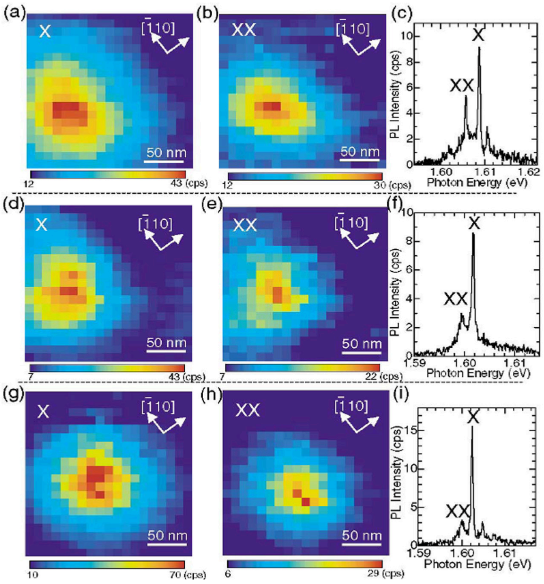

Fig. 2.3.: (a)-(i) Series of high-resolution photo-luminescence images of exciton state [(a), (d), and (g)], biexciton state [(b), (e), and (h)], and corresponding photo-luminescence spectra [(c), (f), and (i)] for three different quantum dots. Scanning area is 210×210 nm^2. Crystal axes along [110] and [$\bar{1}10$] directions are indicated. Photo-luminescence image sizes of biexciton are always smaller than those of exciton. This figure is taken from Matsuda *et al.* [23].

The larger spread in the exciton images, as compared to the biexciton images, shows that the lighter exciton was able to roam farther than the heavier biexciton before recombination. Up until this point all images of excitons showed only a point like structure. These images where possible due to the increased resolution, up to 30 nm, that Matsuda and his team were able to accomplish.

In 2008 scientists built the first computer components that use excitons [24]. Researchers were able to construct an exciton optoelectronic transistor (EXOT) out of two coupled quantum wells made out of aluminum gallium arsenide/gallium arsenide heterostructures. In operation the EXOT behaves just like a field effect transistor (FET) except that instead of controlling an electron flux, as in the case of the FET, the EXOT controls a flux of excitons. In Fig. 2.4 we see the emissions of an EXOT in the off state (D) and the on state (E). For the images the source voltage is -1.5 V, the drain voltage is -2.5 V and the gate voltage is 0V for the off state and -3V for the on state.

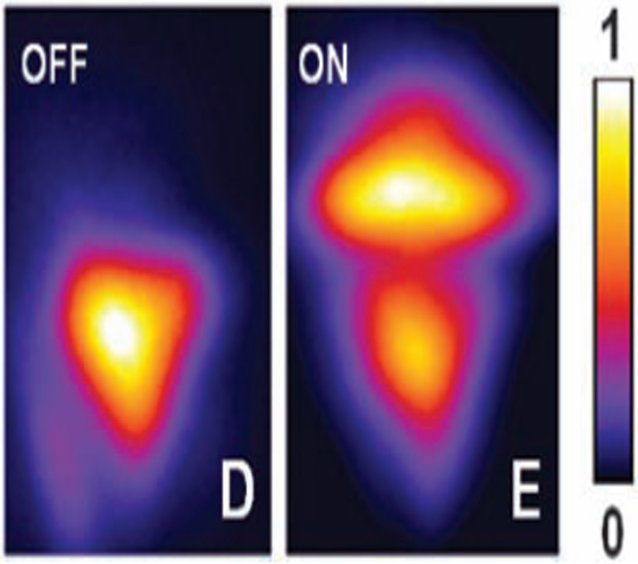

Fig. 2.4.: Emission image for an exciton optoelectronic transistor (EXOT). The left image (D) shows the EXOT in the off configuration and the right image (E) in the on configuration. The source voltage is -1.5 V, the drain voltage is -2.5 V and the gate voltage is 0 V for the off state and -3 V for the on state. This figure is taken from L.V. Butov *et al.* [24].

Next we will combine our understanding of a BEC with what we have just discussed about excitons to explore exciton condensation in double layer systems.

2.1 Double Quantum Well / GaAs/$\mathbf{Al_xGa_{1-x}As}$

> It was not so very long ago that people thought that semiconductors were part-time orchestra leaders and microchips were very, very small snack foods. (Geraldine A. Ferraro)

Before we talk about the specifics of exciton condensation we will first take a moment to understand some basic properties of gallium arsenide (GaAs) and aluminum gallium arsenide ($Al_xGa_{1-x}As$) which are typical materials used to create semiconductor heterostructures. GaAs is a type III/IV semiconductor that is used as the chief component in many different devices such as integrated circuits, infrared light-emitting diodes, and solar cells. The manufacturing of GaAs is performed using any of number of different techniques ranging from vapor phase epitaxy to create thin films [25] to molecular beam epitaxy to create heterostructures. In Fig. 2.5 we see the zinc blende configuration of the unit cell for GaAs with a lattice constant of 5.6533 Å.

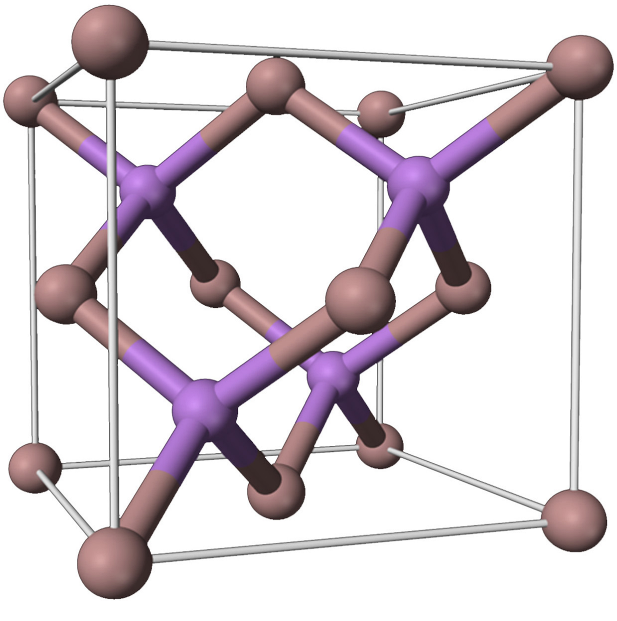

Fig. 2.5.: Figure shows the zinc blende crystal structure of GaAs which can be created by using two interpenetrating face-centered cubic lattices of Gallium and Arsenide. This figure is taken from Wikipedia [26].

The zinc blende structure is created by two interpenetrating face-centered cubic lattices of gallium and arsenide and leads to a first Brillouin zone shown in Fig. 2.6 with the high symmetry points labeled.

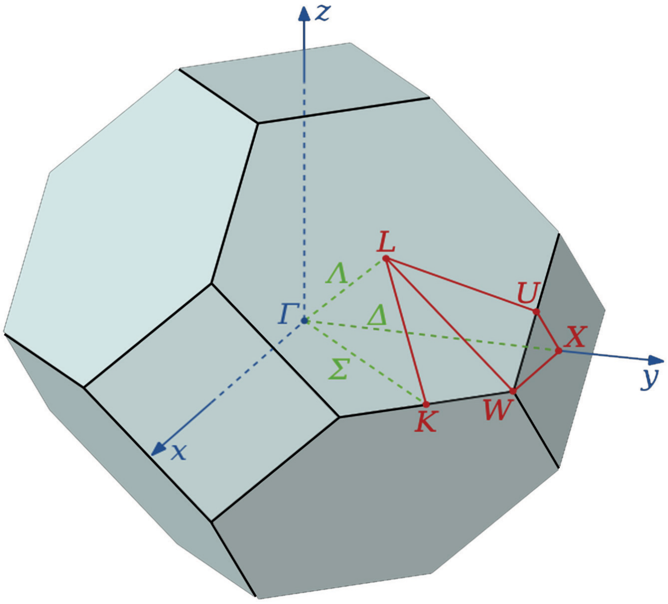

Fig. 2.6.: Figure shows the first Brillouin zone for a zinc blende crystal with its high symmetry points labeled. We will be most interested in the Γ point which lies at the center of the band or **k** = 0 position. This figure is taken from Wikipedia [27].

The following lists some of the relevant quantities for GaAs and $\mathrm{Al}_x\mathrm{Ga}_{1-x}\mathrm{As}$ as relative to the Γ-point [28] which is the location of the peak of the valence band and minimum of the conduction band. At 300 K the band gap for GaAs is 1.424 eV. The effective masses are, for the electron $m^* = 0.063m_e$ where m_e is the free electron mass, for the heavy holes $m_{hh} = 0.51m_e$, and for the light holes $m_{lh} = 0.082m_e$. The bulk electron mobility is $8500\,\mathrm{cm}^2/(\mathrm{Vs})$. In Eq. (2.1) the presence of the different hole masses is accounted for in the effective hole mass. These different hole masses are a result of spin-orbit coupling where the total angular momentum is equal to 3/2. There is one final hole band, the split-off band, with total angular momentum of 1/2 which is neglected due to its band maximum being displaced from that of the light hole and heavy hole by -0.34 eV. At the hole carrier densities that we are considering the split-off hole band is not relevant. The carrier densities for GaAs are: conduction band $\sim 4.7 \times 10^{17}\,\mathrm{cm}^{-3}$, and valence band $\sim 9.0 \times 10^{18}\,\mathrm{cm}^{-3}$. $\mathrm{Al}_x\mathrm{Ga}_{1-x}\mathrm{As}$ is a semiconductor, where x ranges from zero to one indicating the alloy, with a lattice constant from 5.6533 Å, for $x = 0$ or GaAs, to 5.6611 Å, for $x = 1$ or AlAs. For $\mathrm{Al}_x\mathrm{Ga}_{1-x}\mathrm{As}$ the band gap ranges from 1.424 eV for $x = 0$ to 2.168 eV for $x = 1$. With its very similar lattice constant and greater band gap $\mathrm{Al}_x\mathrm{Ga}_{1-x}\mathrm{As}$ is used as an insulator between GaAs layers when creating a semiconductor heterostructure. Next we turn to a discuss of the band structure of electrons in a two dimensional electron gas (2DEG) that forms between the layers of GaAs and $\mathrm{Al}_x\mathrm{Ga}_{1-x}\mathrm{As}$.

2.1.1 Band Structure

When we talk about the band structure of a material what we are talking about is the relationship between the momentum of a charge carrier in the material and its energy or in other words its dispersion relation. There are many different models that can be used when one wishes to calculate the band structure. They range from the nearly free electron model, where interactions between the electrons are ignored, to the tight binding model, where the electrons in a crystal are assumed to be tightly bound to the ionic cores of the crystal.

Obtaining the eigenstates and eigenvalues of an electron in a realistic crystal is a very difficult and complex many-body problem. In order for us to make any progress we must begin with a few simplifying approximations. We begin by using the Born-Oppenheimer approximation (BOA) which states that since the valence electrons are so much lighter and move so much faster than the ionic cores of the crystal we can treat the cores as located at fixed points which allows us to solve the problem separately for the electrons and the cores.

When we apply the BOA we use a static periodic attractive coulomb potential, which represents the attraction due to the ionic cores, and a repulsive coulomb potential, which represents the electron-electron interaction, which results in the many-body electron Hamiltonian

$$H = -\frac{\hbar^2}{2m}\sum_i \nabla_i^2 - Ze^2 \sum_i \sum_{\mathbf{R}} \frac{1}{|\mathbf{r}_i - \mathbf{R}|} + \frac{1}{2}e^2 \sum_{i \neq j} \frac{1}{|\mathbf{r}_i - \mathbf{r}_j|} \tag{2.11}$$

where $\mathbf{r}_i$ are the locations of the electrons and $\mathbf{R}$ are the locations of the ionic cores. In Eq. (2.11) the first term represents the kinetic energy of the electrons, the second term is the interaction between the electrons and the ionic cores, and the final term is the electron-electron interaction. Owing to the electron-electron interaction term in Eq. (2.11) the equation $H\psi_\alpha = E_\alpha \psi_\alpha$ is still too difficult to solve. One way to proceed from here is to apply the Hartree-Fock approximation (HFA) which assumes that each electron moves in an averaged potential due to every other electron. In addition to this averaging, which is the Hartree part of the approximation, we also take into account an electron correlation effect called the exchange interaction. The overall effect of the exchange interaction is lower the energy of our electrons due to the fact that same-spin electrons tend to keep themselves apart from one another thereby lowering their energy.

In order to proceed further we will make the assumption that the ground state wavefunction in the HFA can be expressed as a Slater determinate of single particle wavefunctions

$$\Psi = \begin{vmatrix} \psi_1(\mathbf{r}_1, s_1) & \psi_1(\mathbf{r}_2, s_2) & \cdots & \psi_1(\mathbf{r}_N, s_N) \\ \psi_2(\mathbf{r}_1, s_1) & \psi_2(\mathbf{r}_2, s_2) & \cdots & \psi_2(\mathbf{r}_N, s_N) \\ \vdots & \vdots & \ddots & \vdots \\ \psi_N(\mathbf{r}_1, s_1) & \psi_N(\mathbf{r}_2, s_2) & \cdots & \psi_N(\mathbf{r}_N, s_N) \end{vmatrix}. \tag{2.12}$$

This representation naturally encodes the anti-symmetry of the overall many-body wavefunction that is required due to the fermionic nature of electrons. Our goal is to find the particular $\psi_i(\mathbf{r}_i, s_i)$ that minimizes the energy

$$E = \frac{\langle \Psi | H | \Psi \rangle}{\langle \Psi | \Psi \rangle}. \tag{2.13}$$

The solution that is able to accomplish this will be given by

$$-\frac{\hbar^2}{2m}\nabla^2\psi_i(\mathbf{r}_i,s_i) - Ze^2\sum_R \frac{1}{|\mathbf{r}-\mathbf{R}|}\psi_i(\mathbf{r}_i,s_i) + e^2\sum_j \frac{|\psi_j(\mathbf{r}_j,s_j)|^2}{|\mathbf{r}-\mathbf{r}'|}d\mathbf{r}'\psi_i(\mathbf{r}_i,s_i)$$
$$-e^2\sum_j\int \frac{\psi_j^*(\mathbf{r}_j,s_j)\psi_i^*(\mathbf{r}_i,s_i)\psi_i(\mathbf{r}_i,s_i)\psi_j(\mathbf{r}_j,s_j)}{|\mathbf{r}-\mathbf{r}'|}d\mathbf{r}'\delta_{s_i,s_j} = E_i\psi_i(\mathbf{r}_i,s_i). \quad (2.14)$$

It has been shown that it is possible to modify the potential to include all electron correlation effects [29] [30] [31] which means that it should be possible in principle to recast the many electron problem into an equivalent single body problem of electrons moving in a static potential while still taking into account the electron-electron interactions. This is currently not possible since the form of the exchange correlation function is unknown. The energy eigenvalues, E_i, of Eq. (2.14) form the band structure of our crystal using the HFA.

There are, of course, other approaches to solving the band structure of a crystal that take into account all electron-electron correlation effects but these techniques are beyond the scope of this discussion. To gain a very basic understanding of the band structure for a 2D electron gas (2DEG) we start by considering a square lattice model depicted in Fig. 2.7. The lattice consists of an array of atoms separated by a uniform lattice constant. Each atom has exactly four nearest neighbors.

The resulting tight binding model for an electron hopping on such a lattice is

$$H = -t\sum_{\mathbf{R}_j}\sum_{<>_j}\left[c^\dagger_{\mathbf{R}_j}c_{<>_j} + c^\dagger_{<>_j}c_{\mathbf{R}_j}\right] \quad (2.15)$$

where $c_{\mathbf{R}_j}$ $\left(c^\dagger_{\mathbf{R}_j}\right)$ destroys (creates) an electron at site j and $c_{<>_j}$ $\left(c^\dagger_{<>_j}\right)$ destroys (creates) an electron at a nearest neighbor of site j. We now define the Fourier transform of our operators as

$$c_{\mathbf{R}_j} = \frac{1}{\sqrt{N}}\sum_{\mathbf{k}} e^{-i\mathbf{k}\cdot\mathbf{R}_j}c_{\mathbf{k}} \quad c_{<>_j} = \frac{1}{\sqrt{N}}\sum_{\mathbf{k}} e^{-i\mathbf{k}\cdot(\mathbf{R}_j+\boldsymbol{\delta}_n)}c_{\mathbf{k}}. \quad (2.16)$$

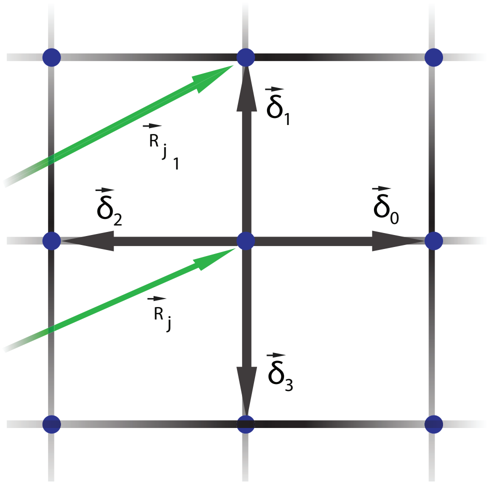

Fig. 2.7.: A lattice with a constant lattice spacing with each atom having exactly four nearest neighbors. The image shows the position vector $\mathbf{R}_j$ as well as the position vector of the nearest neighbor with a 1 label, $\mathbf{R}_{j_1}$.

where the $\boldsymbol{\delta}_n$ are the nearest neighbor displacement vectors of site j shown in Fig. 2.7. By using these transforms our Hamiltonian becomes

$$
\begin{aligned}
H = & -t \sum_{\mathbf{R}_j} \left[\frac{1}{N} \sum_{\mathbf{k}} e^{i\mathbf{k}\cdot\mathbf{R}_j} c^{\dagger}_{\mathbf{k}} \sum_{\mathbf{k}'} \sum_{n} e^{-i\mathbf{k}'\cdot(\mathbf{R}_j+\boldsymbol{\delta}_n)} c_{\mathbf{k}'} + \text{h.c.} \right] \\
= & -t \sum_{\mathbf{k},\mathbf{k}'} \left[\frac{1}{N} \sum_{\mathbf{R}_j} e^{i(\mathbf{k}-\mathbf{k}')\cdot\mathbf{R}_j} \sum_{n} e^{-i\mathbf{k}\cdot\boldsymbol{\delta}_n} c^{\dagger}_{\mathbf{k}} c_{\mathbf{k}'} + \text{h.c.} \right] \\
= & -t \sum_{\mathbf{k}} \left[\sum_{n} e^{-i\mathbf{k}\cdot\boldsymbol{\delta}_n} c^{\dagger}_{\mathbf{k}} c_{\mathbf{k}} + \text{h.c.} \right], \qquad (2.17)
\end{aligned}
$$

where the sum over $\mathbf{k}$ is understood to be over only the first Brillouin zone, h.c. stands for the hermitian conjugate of the first term in the brackets and $\phi(\mathbf{k}) = t\sum_n e^{-i\mathbf{k}\cdot\boldsymbol{\delta}_n}$ is the band structure. Due to the symmetry of the problem we have $\delta_0 = -\delta_2$ and $\delta_1 = -\delta_3$ which leaves us with $\phi(\mathbf{k}) = 2t\cos(k_x a) + 2t\cos(k_y a)$, where a is the lattice spacing, for our band structure. In Fig. 2.8 (a) we show a plot of $\phi(\mathbf{k})$ and in (b) we show an enlarged view of a contour plot of $\phi(\mathbf{k})$.

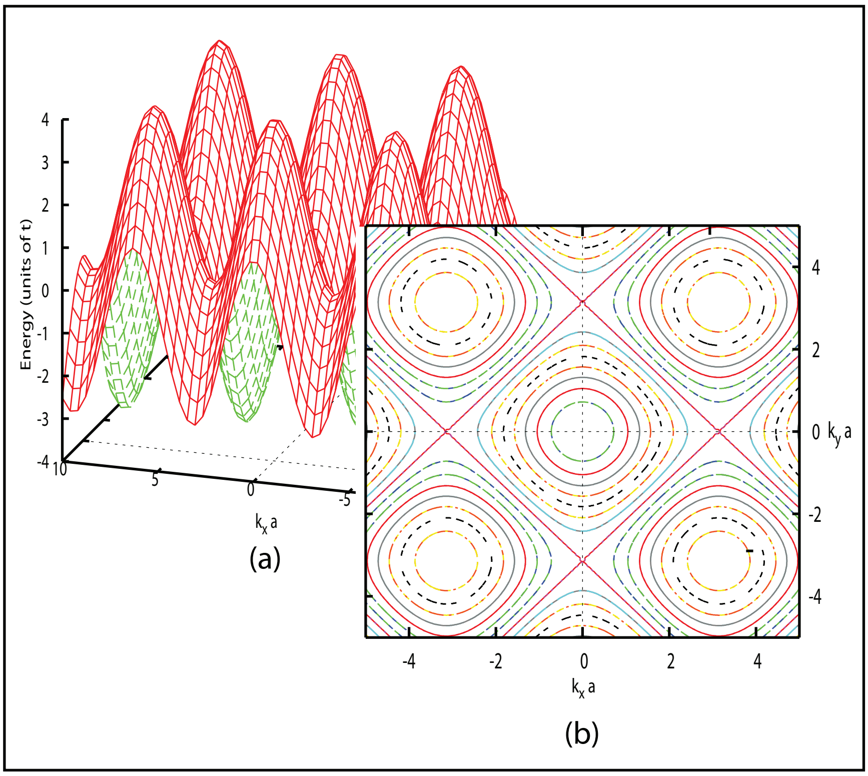

Fig. 2.8.: (a) Shows the plot of band structure, $\phi(\mathbf{k}) = 2\cos(k_x a) + 2\cos(k_y a)$, for a square lattice with a lattice constant, a. (b) Shows a plot of the contours of $\phi(\mathbf{k})$.

For small $\mathbf{k}$ at the zone center we see that the dispersion relation is quadratic in the momentum. Now that we know the dispersion relation we are in a position to derive the equations for exciton condensation using a self-consistent mean field approach.

2.1.2 Mean-Field Approximation

In this section we wish to determine a set of self-consistent mean field equations that govern the behavior of the exciton condensate in a double layer quadratically dispersing system such as two coupled quantum wells. Such a system can be constructed using two layers of GaAs separated by $\mathrm{Al}_x\mathrm{Ga}_{1-x}\mathrm{As}$ as in Fig. 2.9. In this schematic we show that we have one GaAs layer (upper) that is n-doped and one GaAs layer (bottom) that is p-doped with front and back gates to drive the charge carriers to the interfaces between these layers and the $\mathrm{Al}_x\mathrm{Ga}_{1-x}\mathrm{As}$ layer through independent contacts to each layer.

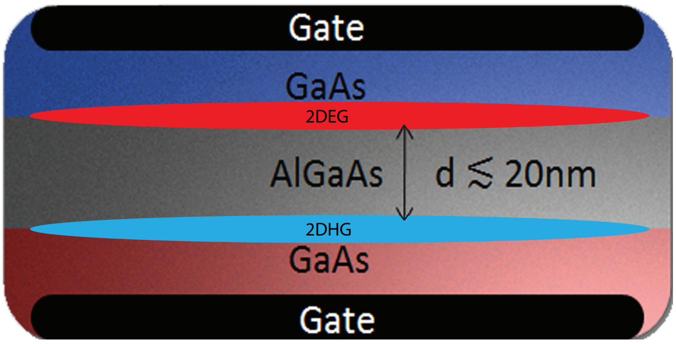

Fig. 2.9.: Cartoon depicting the stacking of GaAs and $\mathrm{Al}_x\mathrm{Ga}_{1-x}\mathrm{As}$ layers to form a heterostructure. The interface between the GaAs and AlGaAs layers forms a quantum well that is used to contain either a two dimensional electron gas (2DEG) or a two dimensional hole gas (2DHG).

We begin by writing our total hamiltonian as a sum of two components

$$\hat{H} = \hat{H}_0 + \hat{H}_{int} \tag{2.18}$$

where $\hat{H}_0(\hat{H}_{int})$ are the non-interacting (interacting) pieces.

$$\begin{aligned}\hat{H} = \sum_{\mathbf{k},\Omega,\sigma} c^{\dagger}_{\Omega,\sigma}(\mathbf{k})\varepsilon_{\Omega,\sigma}(\mathbf{k})c_{\Omega,\sigma}(\mathbf{k}) + \\ \frac{1}{2}\sum_{\mathbf{q},\mathbf{k},\mathbf{k}'}\sum_{\Omega,\Omega'}\sum_{\sigma,\sigma'} c^{\dagger}_{\Omega,\sigma}(\mathbf{k}+\mathbf{q})c^{\dagger}_{\Omega',\sigma'}(\mathbf{k}'-\mathbf{q})\mathcal{V}_{\zeta}(\mathbf{q})c_{\Omega',\sigma'}(\mathbf{k}')c_{\Omega,\sigma}(\mathbf{k})\end{aligned} \tag{2.19}$$

At this point we need to take a moment to understand what Eq. (2.19) means. To begin σ represents the spin of the particle, giving $\dim(\sigma) = 2$. Next we have Ω which represents all the extrinsic quantum numbers for our system. An example of these would be, in a double layer linearly dispersing system, the lattice index ν, $\dim(\nu) = 4$, and the valley index τ, $\dim(\tau) = 2$, which would give $\dim(\Omega) = 8$. Now we turn to ε which is the kinetic energies associated with Ω, σ and k. Finally we have ζ which is a combination of $\Omega, \Omega', \sigma, \sigma'$, and q that is used to determine which potential energy matrix element, $\mathcal{V}$, we are interested in. We note that in Eq. (2.19) we have already assumed that the interaction preserves σ and Ω and conserves $\mathbf{k}$ by transferring momentum $\mathbf{q}$ from one particle to another.

Non-Interacting Components

We will begin by first working with the non-interacting portion of the hamiltonian,

$$\hat{H}_0 = \sum_{\mathbf{k}} \sum_{\nu} \sum_{\sigma} c^{\dagger}_{\nu,\sigma}(\mathbf{k}) \mathcal{K}_{\nu,\sigma}(\mathbf{k}) c_{\nu,\sigma}(\mathbf{k}). \tag{2.20}$$

With the choice of this basis we have a kinetic energy matrix $\mathcal{K}_{\nu,\sigma}$ of the form

$$\mathcal{K}_{\nu,\sigma} = \begin{bmatrix} \varepsilon_{T,\uparrow} & 0 & 0 & 0 \\ 0 & \varepsilon_{B,\uparrow} & 0 & 0 \\ 0 & 0 & \varepsilon_{T,\downarrow} & 0 \\ 0 & 0 & 0 & \varepsilon_{B,\downarrow} \end{bmatrix}. \tag{2.21}$$

where $T(B)$ indicate the top (bottom) layers. Since we can write $\varepsilon_{\nu,\sigma} = \varepsilon_{\nu}$ we can rewrite the non-interacting hamiltonian as

$$\hat{H}_0 = \sum_{\mathbf{k}} \begin{pmatrix} c^{\dagger}_T(\mathbf{k}) & c^{\dagger}_B(\mathbf{k}) \end{pmatrix} \begin{bmatrix} \varepsilon_T & 0 \\ 0 & \varepsilon_B \end{bmatrix} \begin{pmatrix} c_T(\mathbf{k}) \\ c_B(\mathbf{k}) \end{pmatrix} \tag{2.22}$$

where we have eliminated the multiplicative factor 2 since it will also appear in H_{int} because the Coulomb interaction is spin preserving.

Interacting Components

We next turn our attention to the interacting components of our hamiltonian given by

$$\hat{H}_{int} = \frac{1}{2}\sum_{\mathbf{q},\mathbf{k},\mathbf{k}'}\sum_{\nu,\nu'}\sum_{\sigma,\sigma'} c^{\dagger}_{\nu,\sigma}(\mathbf{k}+\mathbf{q})c^{\dagger}_{\nu',\sigma'}(\mathbf{k}'-\mathbf{q})\mathcal{V}_{\zeta}(\mathbf{q})c_{\nu',\sigma'}(\mathbf{k}')c_{\nu,\sigma}(\mathbf{k}). \tag{2.23}$$

We can best understand this interaction, and its simplification through Wick contractions, using Feynman diagrams. In Fig. (2.10) we see the general diagram which shows that we have two particles that begin with momenta $\mathbf{k}$ and $\mathbf{k}'$, they interact by transferring momentum $\mathbf{q}$ from one to the other, and end up with momenta $\mathbf{k}+\mathbf{q}$ and $\mathbf{k}-\mathbf{q}$ respectively due to momentum conservation.

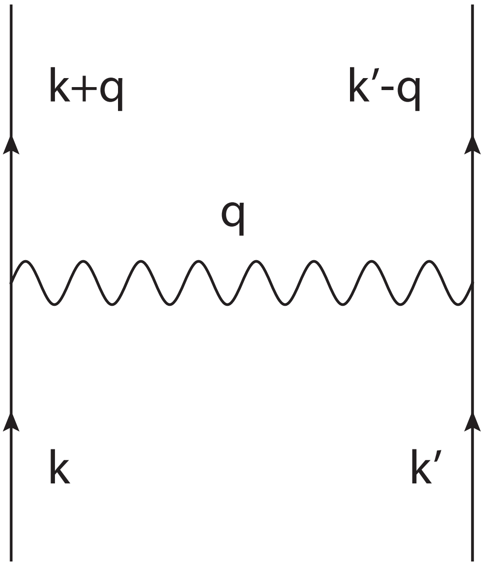

Fig. 2.10.: This picture shows a basic two particle interaction. Two particles are destroyed, one with momentum $\mathbf{k}$ the other with $\mathbf{k}'$, and two particles are created, one with momentum $\mathbf{k}+\mathbf{q}$ and the other with $\mathbf{k}'-\mathbf{q}$, thus maintaining momentum conservation with an overall momentum transfer of $\mathbf{q}$.

As we have said before our interaction preserves spin so we will drop our sum over σ leaving us with

$$\hat{H}_{int} = \frac{1}{2}\sum_{\mathbf{q},\mathbf{k},\mathbf{k}'}\sum_{\nu,\nu'} c^{\dagger}_{\nu}(\mathbf{k}+\mathbf{q})c^{\dagger}_{\nu'}(\mathbf{k}'+\mathbf{q})\mathcal{V}_{\zeta}(\mathbf{q})c_{\nu'}(\mathbf{k}')c_{\nu}(\mathbf{k}). \tag{2.24}$$

The number of interaction elements will be $\dim(\nu)^2 \times \dim(\nu)^2 = 4 \times 4 = 16$ since each entry will contain a product of two creation and two annihilation operators. The following list shows all 16 combinations.

$$\begin{array}{ll}
c_T^\dagger(\mathbf{k}+\mathbf{q})c_T^\dagger(\mathbf{k}'-\mathbf{q})c_T(\mathbf{k}')c_T(\mathbf{k}) & c_B^\dagger(\mathbf{k}+\mathbf{q})c_T^\dagger(\mathbf{k}'-\mathbf{q})c_T(\mathbf{k}')c_T(\mathbf{k}) \\
c_T^\dagger(\mathbf{k}+\mathbf{q})c_T^\dagger(\mathbf{k}'-\mathbf{q})c_T(\mathbf{k}')c_B(\mathbf{k}) & c_B^\dagger(\mathbf{k}+\mathbf{q})c_T^\dagger(\mathbf{k}'-\mathbf{q})c_T(\mathbf{k}')c_B(\mathbf{k}) \\
c_T^\dagger(\mathbf{k}+\mathbf{q})c_T^\dagger(\mathbf{k}'-\mathbf{q})c_B(\mathbf{k}')c_T(\mathbf{k}) & c_B^\dagger(\mathbf{k}+\mathbf{q})c_T^\dagger(\mathbf{k}'-\mathbf{q})c_B(\mathbf{k}')c_T(\mathbf{k}) \\
c_T^\dagger(\mathbf{k}+\mathbf{q})c_T^\dagger(\mathbf{k}'-\mathbf{q})c_B(\mathbf{k}')c_B(\mathbf{k}) & c_B^\dagger(\mathbf{k}+\mathbf{q})c_T^\dagger(\mathbf{k}'-\mathbf{q})c_B(\mathbf{k}')c_B(\mathbf{k}) \\
c_T^\dagger(\mathbf{k}+\mathbf{q})c_B^\dagger(\mathbf{k}'-\mathbf{q})c_T(\mathbf{k}')c_T(\mathbf{k}) & c_B^\dagger(\mathbf{k}+\mathbf{q})c_B^\dagger(\mathbf{k}'-\mathbf{q})c_T(\mathbf{k}')c_T(\mathbf{k}) \\
c_T^\dagger(\mathbf{k}+\mathbf{q})c_B^\dagger(\mathbf{k}'-\mathbf{q})c_T(\mathbf{k}')c_B(\mathbf{k}) & c_B^\dagger(\mathbf{k}+\mathbf{q})c_B^\dagger(\mathbf{k}'-\mathbf{q})c_T(\mathbf{k}')c_B(\mathbf{k}) \\
c_T^\dagger(\mathbf{k}+\mathbf{q})c_B^\dagger(\mathbf{k}'-\mathbf{q})c_B(\mathbf{k}')c_T(\mathbf{k}) & c_B^\dagger(\mathbf{k}+\mathbf{q})c_B^\dagger(\mathbf{k}'-\mathbf{q})c_B(\mathbf{k}')c_T(\mathbf{k}) \\
c_T^\dagger(\mathbf{k}+\mathbf{q})c_B^\dagger(\mathbf{k}'-\mathbf{q})c_B(\mathbf{k}')c_B(\mathbf{k}) & c_B^\dagger(\mathbf{k}+\mathbf{q})c_B^\dagger(\mathbf{k}'-\mathbf{q})c_B(\mathbf{k}')c_B(\mathbf{k})
\end{array}$$

This list can be greatly reduced if we ignore the scattering from one layer to the other. Once we do this we are left with

$$\begin{array}{ll}
c_T^\dagger(\mathbf{k}+\mathbf{q})c_T^\dagger(\mathbf{k}'-\mathbf{q})c_T(\mathbf{k}')c_T(\mathbf{k}) & c_B^\dagger(\mathbf{k}+\mathbf{q})c_T^\dagger(\mathbf{k}'-\mathbf{q})c_T(\mathbf{k}')c_B(\mathbf{k}) \\
c_T^\dagger(\mathbf{k}+\mathbf{q})c_B^\dagger(\mathbf{k}'-\mathbf{q})c_B(\mathbf{k}')c_T(\mathbf{k}) & c_B^\dagger(\mathbf{k}+\mathbf{q})c_B^\dagger(\mathbf{k}'-\mathbf{q})c_B(\mathbf{k}')c_B(\mathbf{k}).
\end{array}$$

Our interaction hamiltonian becomes

$$\begin{aligned}
\hat{H}_{int} = \frac{1}{2}\sum_{\mathbf{q},\mathbf{k},\mathbf{k}'} \Big[& c_T^\dagger(\mathbf{k}+\mathbf{q})c_T^\dagger(\mathbf{k}'-\mathbf{q})\mathcal{V}_{TT}(\mathbf{q})c_T(\mathbf{k}')c_T(\mathbf{k}) + \\
& 2c_T^\dagger(\mathbf{k}+\mathbf{q})c_B^\dagger(\mathbf{k}'-\mathbf{q})\mathcal{V}_{TB}(\mathbf{q})c_B(\mathbf{k}')c_T(\mathbf{k}) + \\
& c_B^\dagger(\mathbf{k}+\mathbf{q})c_B^\dagger(\mathbf{k}'-\mathbf{q})\mathcal{V}_{BB}(\mathbf{q})c_T(\mathbf{k}')c_B(\mathbf{k}) \Big]
\end{aligned} \tag{2.25}$$

where we have used $\mathcal{V}_{TB}(\mathbf{q}) = \mathcal{V}_{BT}(-\mathbf{q})$. It is this set of operators that we will perform our Wick contractions on. In order to do this we start with a group of the form

$$c^{\dagger}_{\alpha}(\mathbf{k}+\mathbf{q})c^{\dagger}_{\beta}(\mathbf{k}'-\mathbf{q})c_{\beta}(\mathbf{k}')c_{\alpha}(\mathbf{k}) \tag{2.26}$$

where for this discussion $\alpha, \beta \in \{T, B\}$. When we perform the contractions we will place the set being contracted in a box above its contractions. For this first group we will also provide the corresponding Feynman diagrams in Fig. (2.11).

$$\boxed{c^{\dagger}_{\alpha}(\mathbf{k}+\mathbf{q})c^{\dagger}_{\beta}(\mathbf{k}'-\mathbf{q})c_{\beta}(\mathbf{k}')c_{\alpha}(\mathbf{k})}$$

$$\left\langle c^{\dagger}_{\alpha}(\mathbf{k}+\mathbf{q})c^{\dagger}_{\beta}(\mathbf{k}'-\mathbf{q})\right\rangle c_{\beta}(\mathbf{k}')c_{\alpha}(\mathbf{k}) \qquad \left\langle c_{\beta}(\mathbf{k}')c_{\alpha}(\mathbf{k})\right\rangle c^{\dagger}_{\alpha}(\mathbf{k}+\mathbf{q})c^{\dagger}_{\beta}(\mathbf{k}'-\mathbf{q})$$

(a) (b)

$$\left\langle c^{\dagger}_{\beta}(\mathbf{k}'-\mathbf{q})c_{\beta}(k')\right\rangle c^{\dagger}_{\alpha}(\mathbf{k}+\mathbf{q})c_{\alpha}(\mathbf{k}) \qquad \left\langle c^{\dagger}_{\alpha}(\mathbf{k}+\mathbf{q})c_{\alpha}(k)\right\rangle c^{\dagger}_{\beta}(\mathbf{k}'-\mathbf{q})c_{\beta}(\mathbf{k}')$$

(c) (d)

$$-\left\langle c^{\dagger}_{\beta}(\mathbf{k}'-\mathbf{q})c_{\alpha}(k)\right\rangle c^{\dagger}_{\alpha}(\mathbf{k}+\mathbf{q})c_{\beta}(\mathbf{k}') \qquad -\left\langle c^{\dagger}_{\alpha}(\mathbf{k}+\mathbf{q})c_{\beta}(k')\right\rangle c^{\dagger}_{\beta}(\mathbf{k}'-\mathbf{q})c_{\alpha}(\mathbf{k})$$

(e) (f)

The first evaluation we will make is to require the expectation values in (a) and (b) to be equal to zero which we do since they do not preserve particle number. Next we have the Hartree terms, (c) and (d), that require $\mathbf{q} = 0$. Finally, we have the Fock or exchange terms, (e) and (f) where we need to ask ourselves what type of a solution are we interested finding. We do this by deciding the functional form of the remaining two expectation values. For the current problem we are interested in looking for uniform real space solutions which means in momentum space we will have delta functions over the momenta, implying $\delta_{\mathbf{k}+\mathbf{q},\mathbf{k}'}$ and $\delta_{\mathbf{k}'-\mathbf{q},\mathbf{k}} \Rightarrow \mathbf{q} = \mathbf{k}' - \mathbf{k}$. Using these considerations the contractions we have are

$$\boxed{c^{\dagger}_{\alpha}(\mathbf{k}+\mathbf{q})c^{\dagger}_{\beta}(\mathbf{k}'-\mathbf{q})c_{\beta}(\mathbf{k}')c_{\alpha}(\mathbf{k})}$$

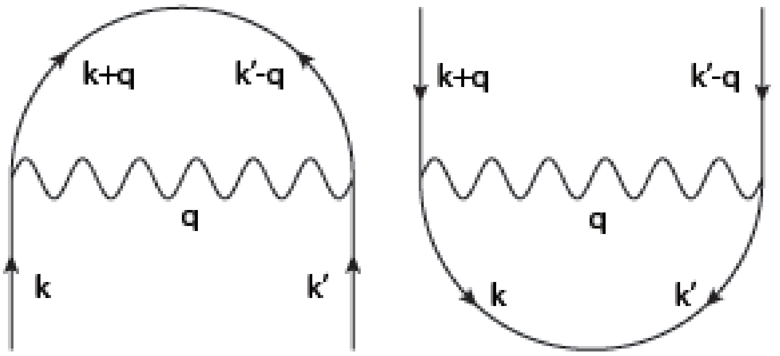

(a) BCS (b) BCS

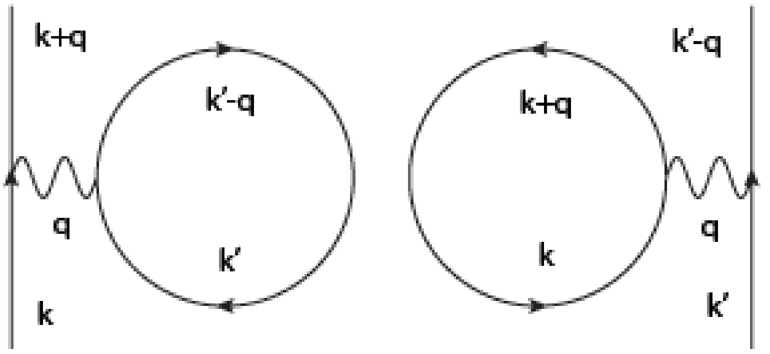

(c) Hartree (d) Hartree

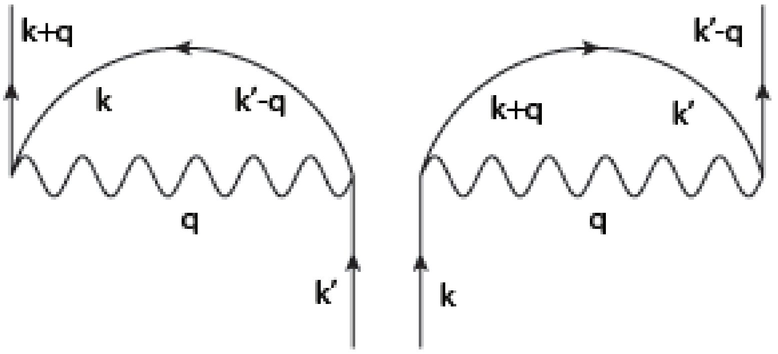

(e) Exchange (f) Exchange

Fig. 2.11.: Feynman diagrams showing the possible contractions for a two body interaction. Diagrams (a) and (b) are removed since they do not preserve particle number. Diagrams (c) and (d) are the Hartree diagrams for which the momentum transfer is equal to zero. Diagrams (e) and (f) are the Fock diagrams.

$$
\begin{aligned}
\left\langle c_{\beta}^{\dagger}(\mathbf{k}'-\mathbf{q})c_{\beta}(\mathbf{k}')\right\rangle c_{\alpha}^{\dagger}(\mathbf{k}+\mathbf{q})c_{\alpha}(\mathbf{k}) &\quad\Rightarrow\quad & n_{\beta\beta}(\mathbf{k}')\left(c_{\alpha}^{\dagger}(\mathbf{k})c_{\alpha}(\mathbf{k})\right)\\
\left\langle c_{\alpha}^{\dagger}(\mathbf{k}+\mathbf{q})c_{\alpha}(\mathbf{k})\right\rangle c_{\beta}^{\dagger}(\mathbf{k}'-\mathbf{q})c_{\beta}(\mathbf{k}') &\quad\Rightarrow\quad & n_{\alpha\alpha}(\mathbf{k})\left(c_{\beta}^{\dagger}(\mathbf{k}')c_{\beta}(\mathbf{k}')\right)\\
-\left\langle c_{\beta}^{\dagger}(\mathbf{k}'-\mathbf{q})c_{\alpha}(\mathbf{k})\right\rangle c_{\alpha}^{\dagger}(\mathbf{k}+\mathbf{q})c_{\beta}(\mathbf{k}') &\quad\Rightarrow\quad & -n_{\beta\alpha}(\mathbf{k})\left(c_{\alpha}^{\dagger}(\mathbf{k}')c_{\beta}(\mathbf{k}')\right)\\
-\left\langle c_{\alpha}^{\dagger}(\mathbf{k}+\mathbf{q})c_{\beta}(\mathbf{k}')\right\rangle c_{\beta}^{\dagger}(\mathbf{k}'-\mathbf{q})c_{\alpha}(\mathbf{k}) &\quad\Rightarrow\quad & -n_{\alpha\beta}(\mathbf{k}')\left(c_{\beta}^{\dagger}(\mathbf{k})c_{\alpha}(\mathbf{k})\right)
\end{aligned}
$$

It is important to remember that each of these contractions gets weighted by the appropriate interaction matrix element. That includes not only making sure to use the right element based upon the indices of the operators but we also have to make sure to apply the corresponding momentum constraints which means that we have to make sure to require that $\mathbf{q}=0$ for the Hartree contractions and that $\mathbf{q}=\mathbf{k}'-\mathbf{k}$ for the Fock contractions. Using these results we can quickly evaluate the contractions for all sets of operators.

$$\boxed{c_{T}^{\dagger}(\mathbf{k}+\mathbf{q})c_{T}^{\dagger}(\mathbf{k}'-\mathbf{q})c_{T}(\mathbf{k}')c_{T}(\mathbf{k})}$$

$$
\begin{aligned}
\left\langle c_{T}^{\dagger}(\mathbf{k}'-\mathbf{q})c_{T}(\mathbf{k}')\right\rangle c_{T}^{\dagger}(\mathbf{k}+\mathbf{q})c_{T}(\mathbf{k}) &\quad\Rightarrow\quad & n_{TT}(\mathbf{k}')\left(c_{T}^{\dagger}(\mathbf{k})c_{T}(\mathbf{k})\right)\\
\left\langle c_{T}^{\dagger}(\mathbf{k}+\mathbf{q})c_{T}(\mathbf{k})\right\rangle c_{T}^{\dagger}(\mathbf{k}'-\mathbf{q})c_{T}(\mathbf{k}') &\quad\Rightarrow\quad & n_{TT}(\mathbf{k})\left(c_{T}^{\dagger}(\mathbf{k}')c_{T}(\mathbf{k}')\right)\\
-\left\langle c_{T}^{\dagger}(\mathbf{k}'-\mathbf{q})c_{T}(\mathbf{k})\right\rangle c_{T}^{\dagger}(\mathbf{k}+\mathbf{q})c_{T}(\mathbf{k}') &\quad\Rightarrow\quad & -n_{TT}(\mathbf{k})\left(c_{T}^{\dagger}(\mathbf{k}')c_{T}(\mathbf{k}')\right)\\
-\left\langle c_{T}^{\dagger}(\mathbf{k}+\mathbf{q})c_{T}(\mathbf{k}')\right\rangle c_{T}^{\dagger}(\mathbf{k}'-\mathbf{q})c_{T}(\mathbf{k}) &\quad\Rightarrow\quad & -n_{TT}(\mathbf{k}')\left(c_{1}^{\dagger}(\mathbf{k})c_{1}(\mathbf{k})\right)
\end{aligned}
$$

$$\boxed{c_{T}^{\dagger}(\mathbf{k}+\mathbf{q})c_{B}^{\dagger}(\mathbf{k}'-\mathbf{q})c_{B}(\mathbf{k}')c_{T}(\mathbf{k})}$$

$$\begin{aligned}
\left\langle c_B^\dagger(\mathbf{k}'-\mathbf{q})c_B(\mathbf{k}')\right\rangle c_T^\dagger(\mathbf{k}+\mathbf{q})c_T(\mathbf{k}) \quad &\Rightarrow \quad n_{BB}(\mathbf{k}')\Big(c_T^\dagger(\mathbf{k})c_T(\mathbf{k})\Big)\\
\left\langle c_T^\dagger(\mathbf{k}+\mathbf{q})c_T(\mathbf{k})\right\rangle c_B^\dagger(\mathbf{k}'-\mathbf{q})c_B(\mathbf{k}') \quad &\Rightarrow \quad n_{TT}(\mathbf{k})\Big(c_B^\dagger(\mathbf{k}')c_B(\mathbf{k}')\Big)\\
-\left\langle c_B^\dagger(\mathbf{k}'-\mathbf{q})c_T(\mathbf{k})\right\rangle c_T^\dagger(\mathbf{k}+\mathbf{q})c_B(\mathbf{k}') \quad &\Rightarrow \quad -n_{BT}(\mathbf{k})\Big(c_T^\dagger(\mathbf{k}')c_B(\mathbf{k}')\Big)\\
-\left\langle c_T^\dagger(\mathbf{k}+\mathbf{q})c_B(\mathbf{k}')\right\rangle c_B^\dagger(\mathbf{k}'-\mathbf{q})c_T(\mathbf{k}) \quad &\Rightarrow \quad -n_{TB}(\mathbf{k}')\Big(c_B^\dagger(\mathbf{k})c_T(\mathbf{k})\Big)
\end{aligned}$$

$$\boxed{c_B^\dagger(\mathbf{k}+\mathbf{q})c_B^\dagger(\mathbf{k}'-\mathbf{q})c_B(\mathbf{k}')c_B(\mathbf{k})}$$

$$\begin{aligned}
\left\langle c_B^\dagger(\mathbf{k}'-\mathbf{q})c_B(\mathbf{k}')\right\rangle c_B^\dagger(\mathbf{k}+\mathbf{q})c_B(\mathbf{k}) \quad &\Rightarrow \quad n_{BB}(k')\Big(c_B^\dagger(\mathbf{k})c_B(\mathbf{k})\Big)\\
\left\langle c_B^\dagger(\mathbf{k}+\mathbf{q})c_B(\mathbf{k})\right\rangle c_B^\dagger(\mathbf{k}'-\mathbf{q})c_B(\mathbf{k}') \quad &\Rightarrow \quad n_{BB}(\mathbf{k})\Big(c_B^\dagger(\mathbf{k}')c_B(\mathbf{k}')\Big)\\
-\left\langle c_B^\dagger(\mathbf{k}'-\mathbf{q})c_B(\mathbf{k})\right\rangle c_B^\dagger(\mathbf{k}+\mathbf{q})c_B(\mathbf{k}') \quad &\Rightarrow \quad -n_{BB}(\mathbf{k})\Big(c_B^\dagger(\mathbf{k}')c_B(\mathbf{k}')\Big)\\
-\left\langle c_B^\dagger(\mathbf{k}+\mathbf{q})c_B(\mathbf{k}')\right\rangle c_B^\dagger(\mathbf{k}'-\mathbf{q})c_B(\mathbf{k}) \quad &\Rightarrow \quad -n_{BB}(\mathbf{k}')\Big(c_B^\dagger(\mathbf{k})c_B(\mathbf{k})\Big)
\end{aligned}$$

This is of course only part of the story. In addition to knowing the different combinations, and their contractions, of operators we also need to know the matrix elements that go with them. We start by using the general form of our two body operators to define our matrix element as follows

$$c_\alpha^\dagger(\mathbf{k}+\mathbf{q})c_\beta^\dagger(\mathbf{k}'-\mathbf{q})c_\beta(\mathbf{k}')c_\alpha(\mathbf{k}) \Rightarrow \langle \mathbf{k}+\mathbf{q},\mathbf{k}'-\mathbf{q}|V_{\alpha\beta}(\mathbf{q})|\mathbf{k},\mathbf{k}'\rangle\,. \tag{2.27}$$

Using this definition we are able to calculate the matrix elements

$$\begin{aligned}
\langle \mathbf{k}+\mathbf{q},\mathbf{k}'-\mathbf{q}|V_{TT}(q)|\mathbf{k},\mathbf{k}'\rangle &= \frac{2\pi e^2}{\epsilon q}\\
\langle \mathbf{k}+\mathbf{q},\mathbf{k}'-\mathbf{q}|V_{BB}(q)|\mathbf{k},\mathbf{k}'\rangle &= \frac{2\pi e^2}{\epsilon q}\\
\langle \mathbf{k}+\mathbf{q},\mathbf{k}'-\mathbf{q}|V_{TB}(q)|\mathbf{k},\mathbf{k}'\rangle &= \frac{2\pi e^2}{\epsilon q}e^{-qd}\\
\langle \mathbf{k}+\mathbf{q},\mathbf{k}'-\mathbf{q}|V_{BT}(q)|\mathbf{k},\mathbf{k}'\rangle &= \frac{2\pi e^2}{\epsilon q}e^{-qd}.
\end{aligned}$$

Now we are ready to combine what we know for the different interaction matrix elements

$$\begin{aligned}
&2V_{TT}(0)n_{TT}(\mathbf{k})c_T^{\dagger}(\mathbf{k}')c_T(\mathbf{k}') - 2V_{TT}(|\mathbf{k}-\mathbf{k}'|)n_{TT}(\mathbf{k})c_T^{\dagger}(\mathbf{k}')c_T(\mathbf{k}')\\
&2V_{BB}(0)n_{BB}(\mathbf{k})c_B^{\dagger}(\mathbf{k}')c_B(k') - 2V_{BB}(|\mathbf{k}-\mathbf{k}'|)n_{BB}(\mathbf{k})c_B^{\dagger}(\mathbf{k}')c_B(\mathbf{k}')\\
&V_{TB}(0)n_{BB}(\mathbf{k})c_T^{\dagger}(\mathbf{k}')c_T(\mathbf{k}') + V_{TB}(0)n_{TT}(\mathbf{k})c_B^{\dagger}(\mathbf{k}')c_B(\mathbf{k}') -\\
&V_{TB}(|\mathbf{k}-\mathbf{k}'|)n_{TB}(\mathbf{k})c_B^{\dagger}(\mathbf{k}')c_T(\mathbf{k}') - V_{TB}(|\mathbf{k}-\mathbf{k}'|)n_{BT}(\mathbf{k}).c_T^{\dagger}(\mathbf{k}')c_B(\mathbf{k}')
\end{aligned}$$

Next we want to group our terms into three sets based upon the index of the operators in each term. The first grouping will contain operators with the index T, the next the operators with index B, and finally we will group the mixed operators on their own.

$$\begin{aligned}
2\left[V_{TT}(0)n_{TT}(\mathbf{k}) + V_{TB}(0)n_{BB}(\mathbf{k}) - V_{TT}(|\mathbf{k}-\mathbf{k}'|)n_{TT}(\mathbf{k})\right] c_T^{\dagger}(\mathbf{k}')c_T(\mathbf{k}')\\
2\left[V_{BB}(0)n_{BB}(\mathbf{k}) + V_{TB}(0)n_{TT}(\mathbf{k}) - V_{BB}(|\mathbf{k}-\mathbf{k}'|)n_{BB}(\mathbf{k})\right] c_B^{\dagger}(\mathbf{k}')c_B(\mathbf{k}')\\
-2V_{TB}(|\mathbf{k}-\mathbf{k}'|)n_{TB}(\mathbf{k})c_B^{\dagger}(\mathbf{k}')c_T(\mathbf{k}') - 2V_{TB}(|\mathbf{k}-\mathbf{k}'|)n_{BT}(\mathbf{k})c_T^{\dagger}(\mathbf{k}')c_B(\mathbf{k}')
\end{aligned}$$

We are finally in a position to write our interaction hamiltonian in its bilinear form as follows

$$\begin{aligned}
\hat{H}_{int} =& \sum_{\mathbf{k}'}\left[V_{TT}(0)n_{TT} + V_{TB}(0)n_{BB} - \sum_{\mathbf{k}} V_{TT}(|\mathbf{k}-\mathbf{k}'|)n_{TT}(\mathbf{k})\right] c_T^{\dagger}(\mathbf{k}')c_T(\mathbf{k}') +\\
&\sum_{\mathbf{k}'}\left[V_{BB}(0)n_{BB} + V_{TB}(0)n_{TT} - \sum_{\mathbf{k}} V_{BB}(|\mathbf{k}-\mathbf{k}'|)n_{BB}(\mathbf{k})\right] c_B^{\dagger}(\mathbf{k}')c_B(\mathbf{k}') -\\
&\sum_{\mathbf{k}'}\left[V_{TB}(|\mathbf{k}-\mathbf{k}'|)n_{TB}(\mathbf{k})c_B^{\dagger}(\mathbf{k}')c_T(\mathbf{k}') + V_{TB}(|\mathbf{k}-\mathbf{k}'|)n_{BT}(\mathbf{k})c_T^{\dagger}(\mathbf{k}')c_B(\mathbf{k}')\right],
\end{aligned} \tag{2.28}$$

where $\sum_{\mathbf{k}} n_{TT}(\mathbf{k}) = n_{TT}$ and $\sum_{\mathbf{k}} n_{BB}(\mathbf{k}) = n_{BB}$. It is time for us to combine the interacting and non-interacting components from Eq. (2.22) and Eq. (2.28).

$$\begin{aligned}\hat{H} =& \sum_{\mathbf{k}} \left[\varepsilon_T + V_{TT}(0)n_{TT} + V_{TB}(0)n_{BB} - \sum_{\mathbf{k}'} V_{TT}(|\mathbf{k}-\mathbf{k}'|)n_{TT}(\mathbf{k}')\right] c_T^\dagger(\mathbf{k})c_T(\mathbf{k}) + \\ & \sum_{\mathbf{k}} \left[\varepsilon_B + V_{BB}(0)n_{BB} + V_{TB}(0)n_{TT} - \sum_{\mathbf{k}'} V_{BB}(|\mathbf{k}-\mathbf{k}'|)n_{BB}(\mathbf{k}')\right] c_B^\dagger(\mathbf{k})c_B(\mathbf{k}) - \\ & \sum_{\mathbf{k}\mathbf{k}'} \left[V_{TB}(|\mathbf{k}-\mathbf{k}'|)n_{TB}(\mathbf{k}')c_B^\dagger(\mathbf{k}')c_T(\mathbf{k}') + V_{TB}(|\mathbf{k}-\mathbf{k}'|)n_{BT}(\mathbf{k}')c_T^\dagger(\mathbf{k}')c_B(\mathbf{k}')\right]\end{aligned} \tag{2.29}$$

Up until now everything we have done has been in terms of electrons in both of the layers. At this point we want to re-write Eq. (2.29) in terms of electrons and holes. We will accomplish this by defining $e^\dagger(\mathbf{k}) \equiv h(-\mathbf{k}) \equiv c^\dagger(\mathbf{k})$ and $e(\mathbf{k}) \equiv h^\dagger(-\mathbf{k}) \equiv c_i(\mathbf{k})$ which follows due to hermiticity. Before we can complete our re-writing we must discover how the charge carrier densities transform with these new definitions

$$\begin{aligned} n_{TT} &= \frac{1}{N}\sum_{\mathbf{k}} \left\langle c_T^\dagger(\mathbf{k})c_T(\mathbf{k})\right\rangle = \frac{1}{N}\sum_{\mathbf{k}}\left\langle e^\dagger(\mathbf{k})e(\mathbf{k})\right\rangle = n_e \\ n_{BB} &= \frac{1}{N}\sum_{\mathbf{k}} \left\langle c_B^\dagger(\mathbf{k})c_T(\mathbf{k})\right\rangle = \frac{1}{N}\sum_{\mathbf{k}}\left\langle h(-\mathbf{k})h^\dagger(-\mathbf{k})\right\rangle \\ &= \frac{1}{N}\sum_{\mathbf{k}}\left\langle 1 - h^\dagger(-\mathbf{k})h(-\mathbf{k})\right\rangle = \frac{1}{N}\sum_{\mathbf{k}}^{allband} \cdots - \frac{1}{N}\sum_{\mathbf{k}}\left\langle h^\dagger(-\mathbf{k})h(-\mathbf{k})\right\rangle = 1 - n_h \\ n_{TB} &= \frac{1}{N}\sum_{\mathbf{k}} \left\langle c_T^\dagger(\mathbf{k})c_B(\mathbf{k})\right\rangle = \frac{1}{N}\sum_{\mathbf{k}}\left\langle e^\dagger(\mathbf{k})h^\dagger(-\mathbf{k})\right\rangle \\ n_{BT} &= \frac{1}{N}\sum_{\mathbf{k}} \left\langle c_B^\dagger(\mathbf{k})c_T(\mathbf{k})\right\rangle = \frac{1}{N}\sum_{\mathbf{k}}\left\langle h(-\mathbf{k})e(\mathbf{k})\right\rangle. \end{aligned}$$

where N is the number of points in the Brillouin zone. Using these operators our hamiltonian becomes

$$\begin{aligned}\hat{H} =& \sum_{\mathbf{k}} \left[\varepsilon_e + V_{ee}(0)n_e - V_{eh}(0)n_h - \sum_{\mathbf{k}'} V_{ee}(|\mathbf{k}-\mathbf{k}'|)n_{ee(\mathbf{k}')}\right] e^{\dagger}(\mathbf{k})e(\mathbf{k}) - \\ & \sum_{\mathbf{k}} \left[-\varepsilon_h + V_{hh}(0)n_h - V_{eh}(0)n_e - \sum_{\mathbf{k}'} V_{hh}(|\mathbf{k}-\mathbf{k}'|)n_{hh}(\mathbf{k}')\right] h(-\mathbf{k})h^{\dagger}(-\mathbf{k}) - \\ & \sum_{\mathbf{k},\mathbf{k}'} \left[V_{eh}(|\mathbf{k}-\mathbf{k}'|)n_{eh}(\mathbf{k}')h(-\mathbf{k})e(\mathbf{k}) + V_{eh}(|\mathbf{k}-\mathbf{k}'|)n_{he}(\mathbf{k}')e^{\dagger}(\mathbf{k})h^{\dagger}(-\mathbf{k})\right] \quad (2.30)\end{aligned}$$

Up until this point we have ignored a potential problem. It would seem that we have an infinity problem due to the fact that we have terms such as $V_{ee}(0)$ where our potential depends on the momentum transfer, $\mathbf{q}$, as $1/q$. We can resolve this apparent problem as follows

$$V_{ee}(0)n_e - V_{eh}(0)n_h = \left[\frac{n_e+n_h}{2} + \frac{n_e-n_h}{2}\right] V_{ee}(0) + \left[\frac{n_e-n_h}{2} - \frac{n_e+n_h}{2}\right] V_{eh}(0)$$

Next we regroup according to the carrier densities

$$V_{ee}(0)n_e \;-\; V_{eh}(0)n_h \;=\; \left[V_{ee}(0) - V_{eh}(0)\right]\frac{n_e+n_h}{2} \;+\; \left[V_{ee}(0) + V_{eh}(0)\right]\frac{n_e-n_h}{2}$$

To continue we need evaluate the quantities in the brackets

$$V_{ee}(0) - V_{eh}(0) = \lim_{q\to 0}\left[\frac{2\pi}{\epsilon q}\left(1-e^{-qd}\right)\right] = \lim_{q\to 0}\left[\frac{2\pi}{\epsilon q}\left(qd + O(q^2)\right)\right] = \frac{2\pi d}{\epsilon}$$

$$V_{ee}(0) + V_{eh}(0) = \lim_{q\to 0}\left[\frac{2\pi}{\epsilon q}\left(1+e^{-qd}\right)\right] = \lim_{q\to 0}\left[\frac{2\pi}{\epsilon q}\left(1 + O(q)\right)\right] = \infty.$$

We can see that a simple solution to dealing with this infinity problem is to require $n_e = n_h$ which along with $V_{hh} = V_{ee}$ means Eq. (2.30) becomes

$$\begin{aligned}\hat{H} =& \sum_{\mathbf{k}} \left[\varepsilon_e + \frac{2\pi d}{\epsilon} n - \sum_{k'} V_{ee}(|\mathbf{k}-\mathbf{k}'|) n_{ee}(\mathbf{k}')\right] e^{\dagger}(\mathbf{k}) e(\mathbf{k}) - \\ & \sum_{\mathbf{k}} \left[-\varepsilon_h + \frac{2\pi d}{\epsilon} n - \sum_{\mathbf{k}'} V_{hh}(|\mathbf{k}-\mathbf{k}'|) n_{hh}(\mathbf{k}')\right] h(-\mathbf{k}) h^{\dagger}(-\mathbf{k}) - \\ & \sum_{\mathbf{k},\mathbf{k}'} \left[V_{eh}(|\mathbf{k}-\mathbf{k}'|) n_{eh}(\mathbf{k}') h(-\mathbf{k}) e(\mathbf{k}) + V_{eh}(|\mathbf{k}-\mathbf{k}'|) n_{he}(\mathbf{k}') e^{\dagger}(\mathbf{k}) h^{\dagger}(-\mathbf{k})\right]. \quad (2.31)\end{aligned}$$

Next we turn our attention to ε_e and ε_h which for symmetric electron-hole bands we have $\varepsilon_h = -\varepsilon_e$ which we can use to further modify Eq. (2.31) giving

$$\begin{aligned}\hat{H} =& \sum_{\mathbf{k}} \left[\xi(\mathbf{k}) e^{\dagger}(\mathbf{k}) e(\mathbf{k}) - \xi(\mathbf{k}) h(-\mathbf{k}) h^{\dagger}(-\mathbf{k})\right] - \\ & \sum_{\mathbf{k}} \left[\Delta^*(\mathbf{k}) h(-\mathbf{k}) e(\mathbf{k}) + \Delta(\mathbf{k}) e^{\dagger}(\mathbf{k}) h^{\dagger}(-\mathbf{k})\right] \quad (2.32)\end{aligned}$$

where $\xi(\mathbf{k}) = \varepsilon_e + \frac{2\pi d}{\epsilon} n - \sum_{\mathbf{k}'} V_{ee}(|\mathbf{k}-\mathbf{k}'|) n_{ee}(\mathbf{k}')$ is the renormalized single particle energy and $\Delta(\mathbf{k}) = \sum_{\mathbf{k}'} V_{eh}(|\mathbf{k}-\mathbf{k}'|) n_{he}(\mathbf{k}')$ is the order parameter. Our next step is much more apparent if we once again turn to matrix notation

$$\hat{H} = \sum_{\mathbf{k}} \begin{pmatrix} e^{\dagger}(\mathbf{k}) & h(-\mathbf{k}) \end{pmatrix} \begin{bmatrix} \xi(\mathbf{k}) & \Delta(\mathbf{k}) \\ \Delta(\mathbf{k}) & -\xi(\mathbf{k}) \end{bmatrix} \begin{pmatrix} e(\mathbf{k}) \\ h^{\dagger}(-\mathbf{k}) \end{pmatrix} \quad (2.33)$$

where we have assumed $\Delta(\mathbf{k}) \in \Re$. We will find it helpful, in a moment, if we can recall some information from our previous experience with spin problem. What we need to do is to write Eq. (2.33) in terms of Pauli matrices, σ_x and σ_y,

$$\hat{H} = \begin{pmatrix} e^{\dagger}(\mathbf{k}) & h(-\mathbf{k}) \end{pmatrix} \left[\Delta(\mathbf{k})\sigma_x + \xi(\mathbf{k})\sigma_z\right] \begin{pmatrix} e(\mathbf{k}) \\ h^{\dagger}(-\mathbf{k}) \end{pmatrix}.$$

The reason for doing this is so that we are able to visualize the relationship between $\xi(\mathbf{k}), \Delta(\mathbf{k})$ and $E(\mathbf{k}) = \sqrt{\xi^2(\mathbf{k}) + \Delta^2(\mathbf{k})}$ which is depicted in Fig. 2.12.

We are now ready to diagonalize the matrix found in Eq. (2.33) which results in the following Hamiltonian (in order to save space we will omit the dependence on the momentum $\mathbf{k}$ within the matricies)

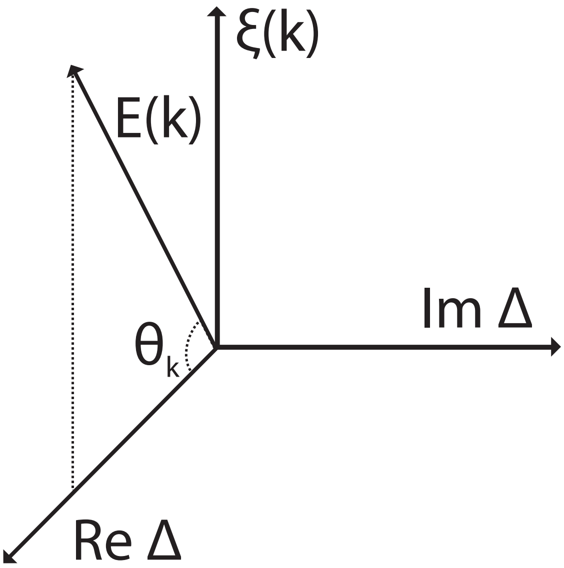

Fig. 2.12.: Shows the relationship between $\xi(\mathbf{k}), \Delta(\mathbf{k})$ and the eigenvalue $E(\mathbf{k})$ of the matrix in Eq. (2.33) showing $\cos(\theta_{\mathbf{k}}) = \xi(\mathbf{k})/E(\mathbf{k})$ and $\sin(\theta_{\mathbf{k}}) = \Delta(\mathbf{k})/E(\mathbf{k})$.

$$\begin{aligned}\hat{H} = \sum_{\mathbf{k}} \begin{pmatrix} e^{\dagger}(\mathbf{k}) & h(-\mathbf{k}) \end{pmatrix} &\begin{bmatrix} \frac{\Delta}{\sqrt{\Delta^2+(E-\xi)^2}} & -\frac{\Delta}{\sqrt{\Delta^2+(E+\xi)^2}} \\ \frac{E-\xi}{\sqrt{\Delta^2+(E-\xi)^2}} & \frac{E+\xi}{\sqrt{\Delta^2+(E+\xi)^2}} \end{bmatrix} \begin{bmatrix} E & 0 \\ 0 & -E \end{bmatrix} \times \\ &\begin{bmatrix} \frac{E+\xi}{\sqrt{\Delta^2+(E+\xi)^2}} & \frac{\Delta}{\sqrt{\Delta^2+(E+\xi)^2}} \\ -\frac{E-\xi}{\sqrt{\Delta^2+(E-\xi)^2}} & \frac{\Delta}{\sqrt{\Delta^2+(E-\xi)^2}} \end{bmatrix} \begin{pmatrix} e(\mathbf{k}) \\ h^{\dagger}(-\mathbf{k}) \end{pmatrix}. \qquad (2.34)\end{aligned}$$

We are able to simplify the above expression by using

$$\begin{aligned} \frac{\Delta}{\sqrt{\Delta^2+(E-\xi)^2}} &= \cos(\theta/2) \qquad & \frac{\Delta}{\sqrt{\Delta^2+(E+\xi)^2}} &= \sin(\theta/2) \\ \frac{E-\xi}{\sqrt{\Delta^2+(E-\xi)^2}} &= \sin(\theta/2) \qquad & \frac{E+\xi}{\sqrt{\Delta^2+(E+\xi)^2}} &= \cos(\theta/2) \qquad (2.35) \end{aligned}$$

These simplifications we now use in Eq. (2.34)

$$\hat{H} = \begin{pmatrix} e^{\dagger}(\mathbf{k}) & h(-\mathbf{k}) \end{pmatrix} \begin{bmatrix} \cos(\theta/2) & -\sin(\theta/2) \\ \sin(\theta/2) & \cos(\theta/2) \end{bmatrix} \begin{bmatrix} E & 0 \\ 0 & -E \end{bmatrix} \times$$
$$\begin{bmatrix} \cos(\theta/2) & \sin(\theta/2) \\ -\sin(\theta/2) & \cos(\theta/2) \end{bmatrix} \begin{pmatrix} e(\mathbf{k}) \\ h^{\dagger}(-\mathbf{k}) \end{pmatrix}. \tag{2.36}$$

What we have then is $\hat{H} = \Psi^{\dagger}\mathcal{M}E\mathcal{M}^{\dagger}\Psi$ where of course this is how we arrive at the quasi-particles operators, $\Psi' = \mathcal{M}^{\dagger}\Psi$, in our system given by

$$\begin{aligned} \Psi' &= \begin{bmatrix} \cos(\theta/2) & \sin(\theta/2) \\ -\sin(\theta/2) & \cos(\theta/2) \end{bmatrix} \begin{pmatrix} e(\mathbf{k}) \\ h^{\dagger}(-\mathbf{k}) \end{pmatrix} \\ \begin{pmatrix} d_{+}(\mathbf{k}) \\ d_{-}(\mathbf{k}) \end{pmatrix} &= \begin{pmatrix} \sin(\theta/2)h^{\dagger}(-\mathbf{k}) + \cos(\theta/2)e(\mathbf{k}) \\ \cos(\theta/2)h^{\dagger}(-\mathbf{k}) - \sin(\theta/2)e(\mathbf{k}) \end{pmatrix} \end{aligned} \tag{2.37}$$

and their inverse

$$\begin{aligned} \Psi &= \begin{bmatrix} \cos(\theta/2) & -\sin(\theta/2) \\ \sin(\theta/2) & \cos(\theta/2) \end{bmatrix} \begin{pmatrix} d_{+}(\mathbf{k}) \\ d_{-}(\mathbf{k}) \end{pmatrix} \\ \begin{pmatrix} e(\mathbf{k}) \\ h^{\dagger}(-\mathbf{k}) \end{pmatrix} &= \begin{pmatrix} \cos(\theta/2)d_{+}(\mathbf{k}) - \sin(\theta/2)d_{-}(\mathbf{k}) \\ \sin(\theta/2)d_{+}(\mathbf{k}) + \cos(\theta/2)d_{-}(\mathbf{k}) \end{pmatrix}. \end{aligned} \tag{2.38}$$

We have gone to all this trouble because we need to express our expectation values $\left\langle e^{\dagger}(\mathbf{k})e(\mathbf{k})\right\rangle$ and $\left\langle h^{\dagger}(-\mathbf{k})e^{\dagger}(\mathbf{k})\right\rangle$ in terms of our new operators $d_{+}(\mathbf{k})$ and $d_{-}(\mathbf{k})$.

$$\begin{aligned} \left\langle e^{\dagger}(\mathbf{k})e(\mathbf{k})\right\rangle &= \sin^{2}(\theta/2)\left\langle d_{-}^{\dagger}(\mathbf{k})d_{-}(\mathbf{k})\right\rangle = \frac{1}{2}\left(1 - \frac{\xi(\mathbf{k})}{\sqrt{\xi^{2}(\mathbf{k}) + \Delta^{2}(\mathbf{k})}}\right) \\ \left\langle h^{\dagger}(-\mathbf{k})e^{\dagger}(\mathbf{k})\right\rangle &= -\sin(\theta/2)\cos(\theta/2)\left\langle d_{-}^{\dagger}(\mathbf{k})d_{-}(\mathbf{k})\right\rangle = -\frac{1}{2}\frac{\Delta(\mathbf{k})}{\sqrt{\xi^{2}(\mathbf{k}) + \Delta^{2}(\mathbf{k})}} \end{aligned}$$

where we have thrown out all terms but $\left\langle d_{-}^{\dagger}(\mathbf{k})d_{-}(\mathbf{k})\right\rangle$ because we know that in a fermionic system only the lower energy bands will be filled. We are finally ready to write down the mean field hamiltonian [32] [33] [34]

$$H = \sum_{\mathbf{k}} \left(e^{\dagger}_{\mathbf{k}} h_{-\mathbf{k}} \right) \begin{pmatrix} \xi_{\mathbf{k}} & \Delta_{\mathbf{k}} \\ \Delta^{*}_{\mathbf{k}} & -\xi_{\mathbf{k}} \end{pmatrix} \begin{pmatrix} e_{\mathbf{k}} \\ h_{-\mathbf{k}^{\dagger}} \end{pmatrix} \tag{2.39}$$

and the associated Hartee-Fock mean field equations for a quadratically dispersing double layer system, where we have included the chemical potential, μ, [33] [34]

$$\xi(\mathbf{k}) = \varepsilon_e + \frac{2\pi d}{\epsilon} n - \mu - \frac{1}{2} \sum_{\mathbf{k}'} V_{ee}(|\mathbf{k} - \mathbf{k}'|) \left(1 - \frac{\xi(\mathbf{k}')}{\sqrt{\xi^2(\mathbf{k}') + \Delta^2(\mathbf{k}')}} \right) \tag{2.40}$$

$$\Delta(\mathbf{k}) = -\frac{1}{2} \sum_{\mathbf{k}'} V_{eh}(|\mathbf{k} - \mathbf{k}'|) \frac{\Delta(\mathbf{k}')}{\sqrt{\xi^2(\mathbf{k}') + \Delta^2(\mathbf{k}')}} \tag{2.41}$$

$$E^2(\mathbf{k}) = \xi^2(\mathbf{k}) + \Delta^2(\mathbf{k}). \tag{2.42}$$

These equations allow us to calculate the properties of a gas of non-interacting excitons. Now if the density of the excitons is reduced low enough we would have essential non-interacting excitons or in other words a single exciton problem. In the following section we discuss this problem and present a semi-quantitative measure to determine when the density of excitons is low enough for us to consider them to be non-interacting. We note, for later, that for each iteration of the above equations the renormalized single particle energy, Eq. (2.40), is essentially the Schrödinger equation in momentum space. This idea will be explored in detail in the next chapter.

2.1.3 Single Exciton Problem

We begin by presenting a short summary of the solution of a two-dimensional hydrogen atom [35]. Solving the problem of the three-dimensional (3D) hydrogen atom played a significant role in the early development of quantum mechanics in the first part of the twentieth century. Progress was initially made in the search for the solution in 1914 when Niels Bohr was able, after using a number of simplifying assumptions, to accurately obtain the spectral frequencies and thus the energy eigenvalues for the hydrogen atom. It was not until a decade later, in 1925-1926, that the full solution was found using the Schrödinger equation. For the problem of the hydrogen atom the Schrödinger equation is analytical and not only tells us the energy eigenvalues but also provides the energy eigenfunctions. If the electron and proton of the hydrogen atom are constrained to move within a two-dimensional plane we have a so called two-dimensional (2D) hydrogen atom.

We begin by writing the Schrödinger equation for the 2D hydrogen atom where the nucleus is located at the origin of the coordinate system

$$\left[-\frac{\hbar}{2m_e}\left[\frac{\partial^2}{\partial r^2}+\frac{1}{r}\frac{\partial}{\partial r}+\frac{1}{r^2}\frac{\partial^2}{\partial \phi^2}\right]-\frac{e^2}{r}\right]\psi_\alpha(r,\phi)=E_\alpha\psi_\alpha(r,\phi) \tag{2.43}$$

where m_e is the mass of the electron and r is the distance from the origin to the electron. We approach this problem in the usual way by seeking a solution using separation of variables, $\psi(r,\phi)=R(r)\Phi(\phi)$, which gives us

$$\Phi(\phi)=\frac{1}{(2\pi)^{1/2}}e^{il\phi}, \qquad l=0,\pm 1,\pm 2,\ldots \tag{2.44}$$

and

$$\frac{d^2}{dr^2}R(r)+\frac{1}{r}\frac{d}{dr}R(r)+\left[\frac{2m_e}{\hbar^2}\left[E+\frac{e^2}{r}\right]-\frac{l^2}{r^2}\right]R(r)=0. \tag{2.45}$$

Equation (2.45) contains both bound and unbound solutions. Since we are interested in the formation and behavior of excitons we will focus on the bound states (i.e. $E<0$).

Bound States

After solving our radial equation we arrive at the expression for the 2D energy eigenvalues

$$E_n=-\frac{1}{2(n-1/2)^2}\frac{m_e e^4}{\hbar^2}, \qquad n=1,2,3\ldots \tag{2.46}$$

and the normalized eigenfunctions

$$R_{nl}(r) = \frac{\beta_n}{2|l|!}\left[\frac{(n+|l|-1)!}{(2n-1)(n-|l|-1)!}\right]^{1/2}(\beta_n r)^{|l|}e^{-\beta_n r/2}$$
$$\times {}_1F_1(-n+|l|+1, 2|l|+1, \beta_n r)), \quad (2.47)$$

where $|l| = 0, 1, 2, \ldots, n-1$, $\beta_n = 2m_e e^2/(n-1/2)\hbar^2$, and ${}_1F_1$ is the confluent hypergeometric function [36]. Since we are interested in the ground state we note for future reference that $R_{10} = \beta_1 e^{-\beta_1 r/2}$ and $\beta_1 = 4m_e e^2/\hbar^2$. This of course, as stated above, is the analytical solution for the problem of an electron and proton bound together and constrained to the same 2D surface. Ultimately we are interested in the problem of an electron and hole bound together by Coulomb interaction with each particle constrained to a two dimensional surface separated by a distance d. In order to deal with the case of both particles being constrained to a 2D surface but not necessarily the same one we must modify the Coulomb interaction from $V(r) = e^2/(\varepsilon r)$ to $V(r) = e^2/(\varepsilon\sqrt{r^2+d^2})$. This change modifies Eq. (2.43) to

$$\left[-\frac{\hbar}{2m_r}\left[\frac{\partial^2}{\partial r^2}+\frac{1}{r}\frac{\partial}{\partial r}+\frac{1}{r^2}\frac{\partial^2}{\partial\phi^2}\right]-\frac{e^2}{\sqrt{r^2+d^2}}\right]\psi_\alpha(r,\phi) = E_\alpha\psi_\alpha(r,\phi), \quad (2.48)$$

where we now use the reduced mass $m_r^{-1} = m_e^{-1} + m_h^{-1}$. This small change to the interaction is enough to prevent us from solving this equation analytically. In order to solve our problem we will consider the Schrödinger equation in momentum space

$$\frac{\hbar^2 k^2}{2m_r}\psi_\alpha(\mathbf{k}) + \int_{k'} V_E(|\mathbf{k}-\mathbf{k}'|)\psi_\alpha(\mathbf{k}') = E_\alpha\psi_\alpha(\mathbf{k}) \quad (2.49)$$

where $\mathbf{k}$ is the two-dimensional wavevector, $\psi_\alpha(\mathbf{k})$ is the momentum-space eigenfunction with eigenvalue E_α, and $V_E(\mathbf{q}) = -V_A(\mathbf{q})e^{-qd}$ where $V_A(\mathbf{q}) = 2\pi e^2/\varepsilon q$ is the Fourier transform of the intralayer Coulomb interaction in 2D. Using Eq. (2.49) we focus on the zero angular momentum sector and numerically diagonalize the matrix [37]

$$H_{mn} = \frac{u_n^2}{2}\delta_{mn} + \frac{u_n\Delta u}{2\pi}\tilde{V}(u_m, u_n) = \frac{u_m}{u_n}H^*_{nm} \quad (2.50)$$

where $u_n = k_n a_0$ is the unit-less momentum with $a_0 = \varepsilon\hbar^2/me^2$ being the Bohr radius and $\tilde{V}(u_m, u_n)$ is the angular-averaged dimensionless electron-hole interaction. Since the Bohr radius for an exciton in a typically semiconductor is about 100 times larger than for the hydrogen atom and the typical dielectric constant for the insulating material is about 10 times larger than the vacuum we have an exciton binding energy of around 13.6 meV. This corresponds to approximately 100 K which means for low temperature calculations the internal states of the exciton are thermally inaccessible so we will only focus on the behavior of the ground state.

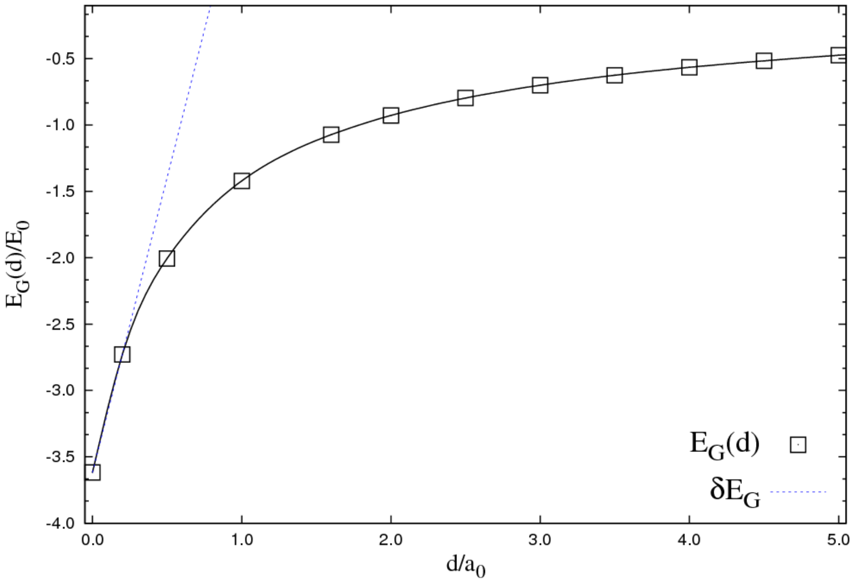

Fig. 2.13.: Excitonic ground-state energy $E_G(d)$ as a function of interlayer distance d obtained from the single-particle Schr̈dinger equation. The dotted line through $d = 0$ shows that at small d the change in the binding energy is linear $\delta E_G = 4E_0(d/a_0)$, as expected from first-order perturbation theory. The binding energy is strongly suppressed at large d.

Figure 2.13 shows the numerically obtained ground-state energy of a single exciton as a function of interlayer distance d. At $d = 0$, the numerical result deviates from the well-known analytical answer by 10%; however, we have verified that this difference is solely due to discretization errors and can be systematically suppressed [37]. When

$d/a_0 \ll 1$ first-order perturbation theory implies that the change in the ground-state energy is linear, $\delta E_G = E_G(d) - E_G(0) = 4E_0(d/a_0)$. At large d the excitonic binding energy is strongly suppressed; for example, when $d/a_0 = 10$ it is reduced to 10% of the binding energy at $d = 0$.

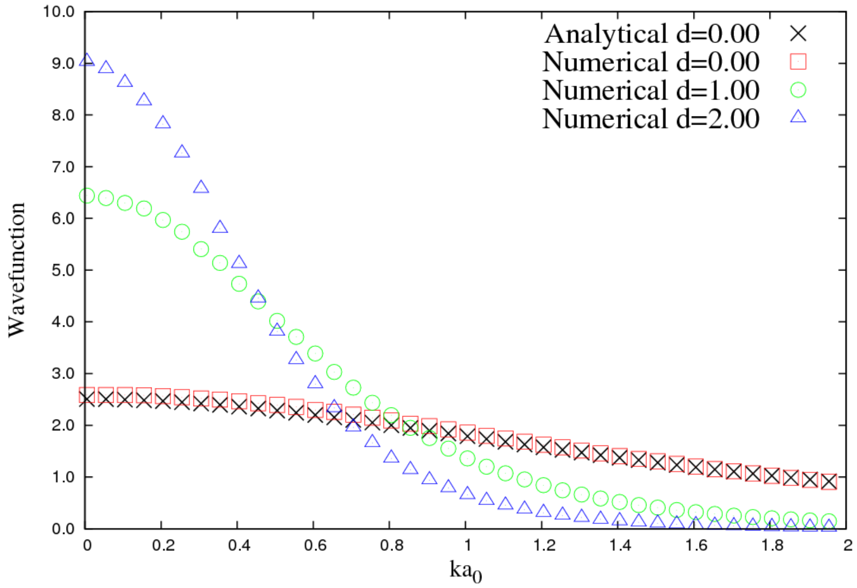

Fig. 2.14.: Ground state wave-function $\psi_G(\mathbf{k})$ for a single exciton as a function of interlayer distance d. The analytical (cross) and numerical (open square) solutions for $d = 0$ are consistent with each other. Their momentum-space width indicates that the exciton size is a_0. As d increases $\psi_G(\mathbf{k})$ sharpens and the size of the exciton, defined by the inverse width of the momentum-space wavefunction, increases.

In Fig. 2.14, we show the corresponding evolution of the ground-state wavefunction with increasing d. At $d = 0$ the normalized wavefunction is given by $\psi_G(\mathbf{k}) = \sqrt{8\pi a_0^2}/(1+k^2a_0^2)^{3/2}$ and is reproduced by our numerical calculations. As d increases, we see that the momentum-space wavefunction sharpens and shows that the single exciton size $a_{ex}(d)$ increases with d.

Mean-Field Analysis

To explore the dilute exciton limit, we recast Eq. (2.41) in terms of $\Phi(\mathbf{p}) = \Delta_{\mathbf{p}}/E_{\mathbf{p}}$, and note that for $\Delta_{\mathbf{p}} \ll \xi_{\mathbf{p}}$ Eq. (2.41) reduces to the single-exciton Shrödinger equation in momentum space, Eq. (2.49). This permits a quantitative comparison between the ground-state exciton wavefunction $\psi_G(\mathbf{p})$ and the Wannier-exciton wavefunction $\Phi(\mathbf{p})$.

Figure 2.15 compares the Wannier wavefunction $\Phi(\mathbf{p})$ at $d/a_0 = 1$ for different values of r_s with the single-exciton wavefunction $\psi_G(\mathbf{p})$. We see that as r_s increases the Wannier wavefunction approaches the single-particle result, as expected.

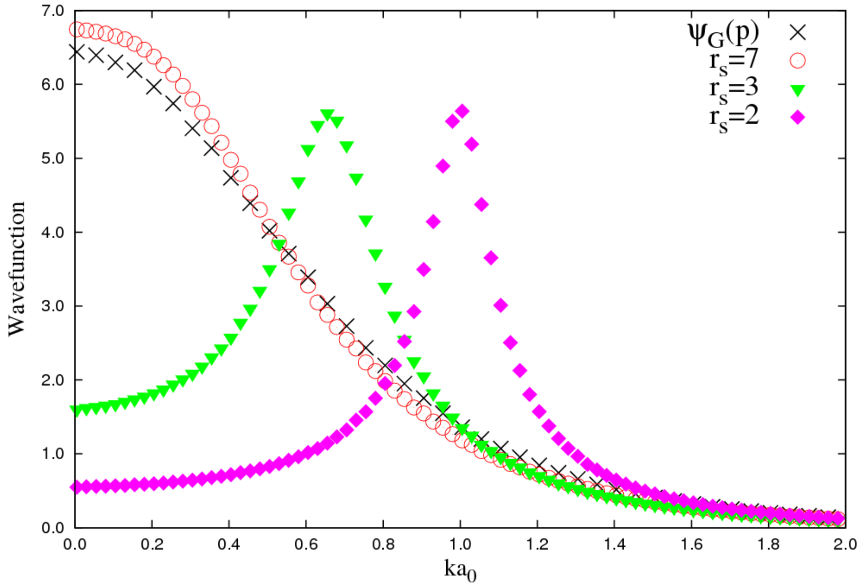

Fig. 2.15.: Comparison of the Wannier wavefunctions $\Phi(\mathbf{p}) = \Delta_{\mathbf{p}}/E_{\mathbf{p}}$ obtained from the mean-field solutions for $r_s = 7$ (circle), $r_s = 3$ (triangle), and $r_s = 2$ (diamond), with the single-exciton wavefunction $\psi_G(\mathbf{p})$ (cross) for $d/a_0 = 1$. As r_s increases the Wannier wavefunction approaches the single-exciton result.

To quantify the proximity between the Wannier and the single-exciton approach, we consider the overlap $\gamma(d/a_0, r_s)$ between the two (real) wavefunctions

$$\gamma(d/a_0, r_s) = \int \frac{d\mathbf{k}}{(2\pi)^2} \Phi^*(k)\psi_G(k). \tag{2.51}$$

A high overlap, $\gamma(d/a_0, r_{sc}) \sim 1$, allows us to define a critical value for $r_{sc}(d/a_0)$ such that for $r_s \geq r_{sc}$ the single-exciton result provides an excellent substitute for the mean-field analysis. Figure 2.16 shows the critical $r_{sc}(d)$ obtained using $\gamma = 0.90$ and $\gamma = 0.95$. We see that for typical values of d the critical r_{sc} scales linearly with d/a_0. It implies, for example, that approaching the dilute-limit at $d/a_0 = 3$ will require reducing the carrier density by a factor of 5 from the corresponding value for the dilute limit at $d/a_0 = 1$.

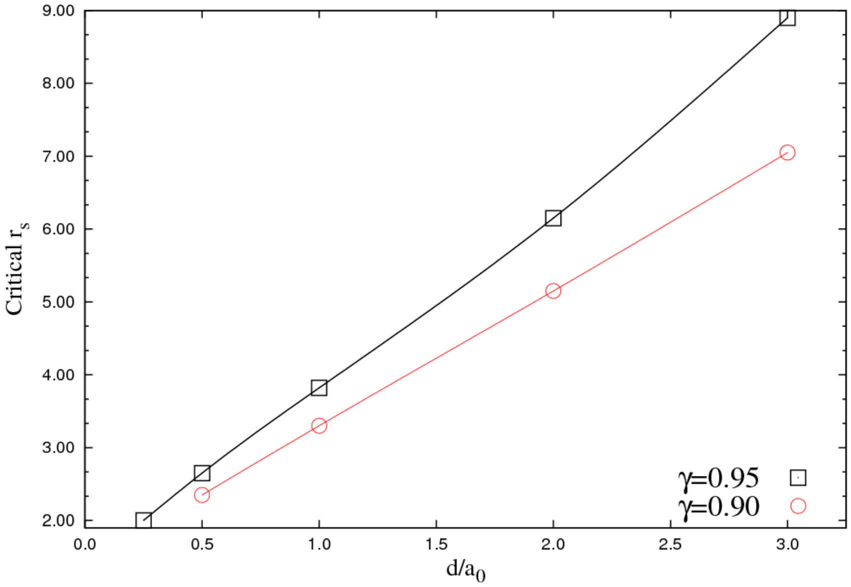

Fig. 2.16.: Interlayer-distance dependence of the critical r_s value obtained using the constraints $\gamma = 0.90$ (bottom) and $\gamma = 0.95$ (top). $r_{sc}(d)$ provides a quantitative way to characterize the diluteness of an excitonic gas by comparing the Wannier wavefunction $\Phi(\mathbf{k})$ with the single-exciton solution $\phi_G(\mathbf{k})$.

This concludes our discuss of exciton condensation in double quantum well systems. From here we follow a very similar route to develop our understanding of the same phenomenon in a two dimensional single layer of graphite which is known as graphene.

2.2 Graphene

> But in writing this book I found myself sadly hampered by the impossibility of drawing such diagrams as were necessary for my purpose: for of course, in our country of Flatland, there are no tablets but Lines, and no diagrams but Lines, all in one straight Line and only distinguishable by difference of size and brightness; so that, when I had finished my treatise (which I entitled, "Through Flatland to Thoughtland") I could not feel certain that many would understand my meaning.
>
> (Edwin A. Abbott, *Flatland: A Romance of Many Dimensions*)

Graphite is a material that we have been using, in the form of pencils, since 1564 [38]. It is made up of single layers of carbon atoms held together by van der Waals forces. It is due to this fact, that the individual layers are weakly bound together, that we are able to use graphite for writing. When we write with a pencil we are actually cleaving off stacks of graphite which we perceive as the writing on a piece of paper. The first studies of graphite and its electronic properties were carrier out in 1947 by P. Wallace [39]. Although, presumably every time we write with a pencil we are potentially leaving behind single layers of graphite [40], which we call graphene, it was not until almost 60 years after Wallace that the first experimental observations of free graphene were made in 2004 [41]. Up until this discovery it was believed that an atomically thin 2D crystal could not exist in nature due to thermodynamic instability [42] [43] [44]. In addition to this up until this point there was no experimental technique capable of sifting through the material left behind by the writing of a pencil to look for a single sheet of atomically thin graphite [45]. Graphene was only discovered in the debris after the optical interference created when a sheet of graphene is observed through a microscope on top of a silicon dioxide substrate [41]. Figure2.17 shows the result of rubbing bulk graphite onto an oxidized silicon wafer. Individual layers of graphene are found by zooming in and looking for the weakest contrasting areas [45].

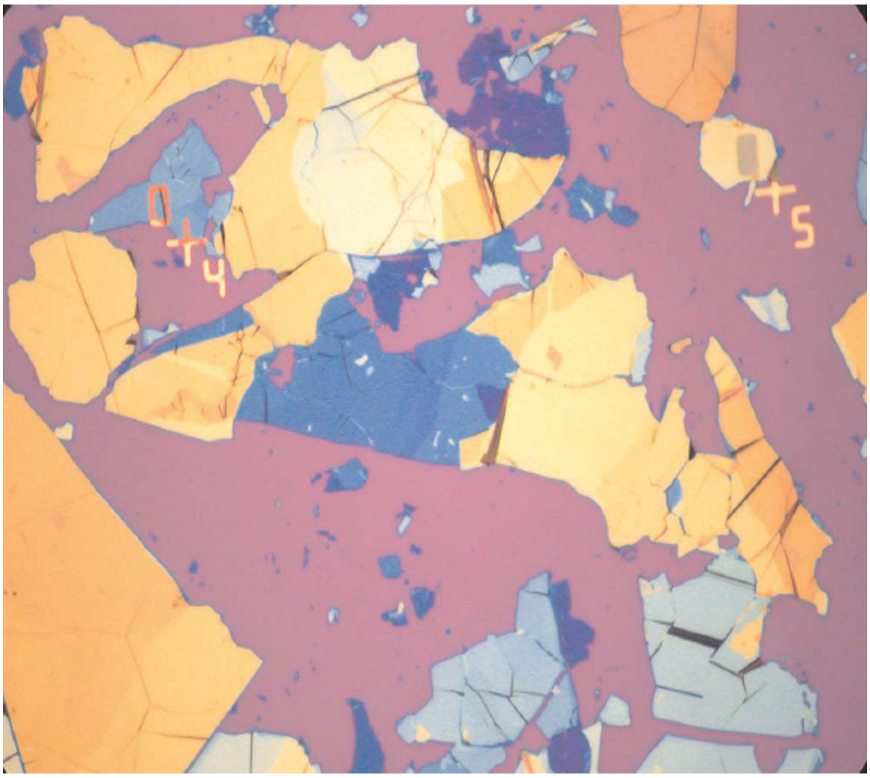

Fig. 2.17.: Figure showing the different colors seen through an optical micrograph of a 300-micron-wide sample of graphite flakes that result from rubbing bulk graphite onto the surface of an oxidized silicon waffer. This figure is taken from A. K. Geim *et al.* [45].

The hexagonal, or honeycomb, shape of the graphene lattice is shown in Fig. 2.18 (A). The hexagonal lattice is a Bravais lattice with a two point basis or we can equivalently think of it as two inter-penetrating triangular lattices which are denoted by the two different color spheres. There are two equivalent unit cells for graphene, one is a diamond which contains one atom from each sub-lattice Fig. 2.18 (B) and the other is a hexagon which contains 1/3 of 6 atoms each located at the corners of the hexagon Fig. 2.18 (C).

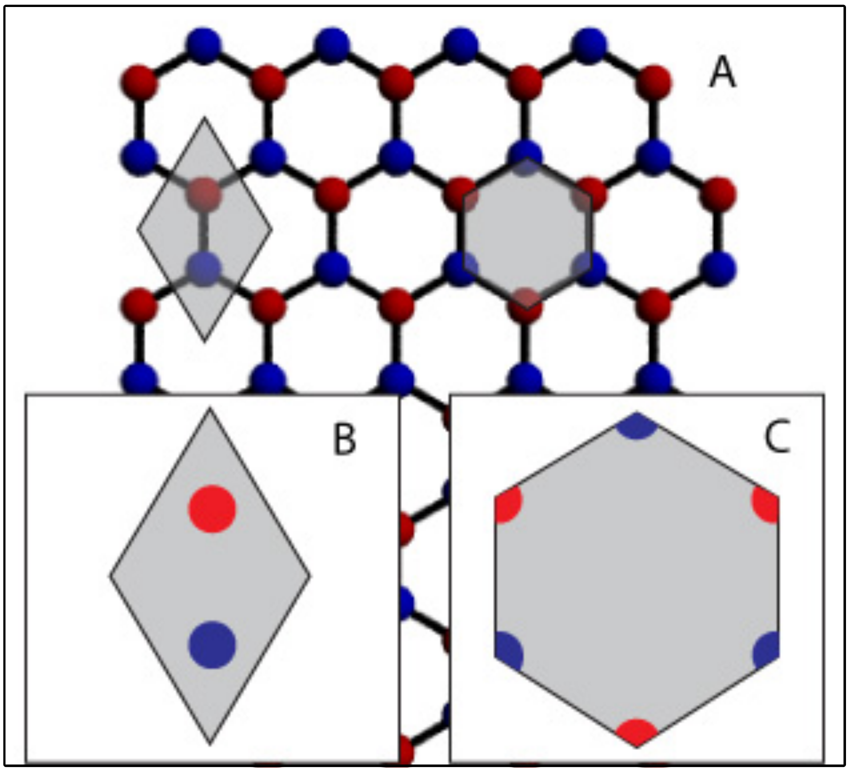

Fig. 2.18.: The hexagonal, or honeycomb, structure of the graphene lattice resulting from the sp^2 hybridization of the carbon atoms is shown in (A) along with two shapes, one a diamond and the other a hexagon, showing the two possible unit cells. The diamond (B) contains one atom from each sub-lattice while the hexagon (C) contains 1/3 of 6 atoms at each of its corners.

In order to understand why the carbon atoms in graphene are arranged in this manner we consider the electron structure of carbon and its bond formation capabilities. Using a configuration of the electronic ground state of carbon, $1s^2 2s^2 2p_x^1 2p_y^1$, we are unable to explain its ability to form two, three, and even four covalent bonds. In order to understand carbons ability to form these covalent bonds, we must understand the process of orbital hybridization. Since we are interested in graphene we will focus on sp^2 hybridization due to graphene's planar structure. For sp^2 hybridization we take the one $2s$ orbital and two of the $2p$ orbitals, say $2p_x$ and $2p_y$, as shown in Fig. 2.19(a) (A) and we hybridize them leaving the $2p_z$ orbital untouched. When these orbitals are hybridized the result is three equivalent energy orbitals with one of these orbitals shown in Fig. 2.19(a) (B). These three hybridized orbitals all lay within a single plane with a bond angle of 120 degrees. The formation of these bonds is responsible for the hexagonal structure of graphene as shown in Fig. 2.19(a) (C). These in-plane bonds are known as σ bonds, the strongest type of covalent bond, and have a bond length of 1.42 Å. The remaining p_z orbital remains untouched, as mentioned above, and is oriented perpendicular to the plane formed by the σ bonds, Fig. 2.19(b) (A). The overlap of the p_z orbital of one carbon atom with its neighbor, shown in Fig. 2.19(b) (B), is responsible for the formation of a π bond shown in Fig. 2.19(b) (C).

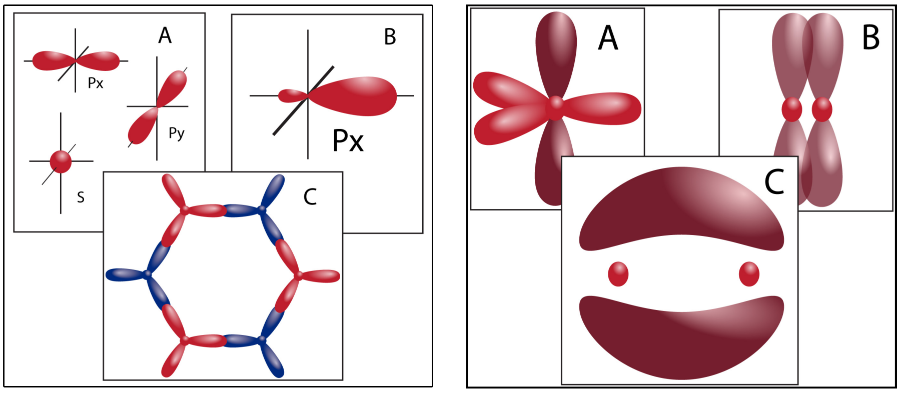

(a)

(b)

Fig. 2.19.: Cartoons depicting the results of sp^2 hybridization in graphene. (a) One s orbital and two p orbitals (A) are combined to from three hybridized orbitals, with one example shown in (B). The three hybrid orbitals all lay within a single plane with a bond angle of 120 degrees (C). These bonds, called σ bonds, are responsible for the rigidity of the lattice and form a deep valence band. (b) The remaining p_z orbital is oriented perpendicular to the plane formed by the σ bonds (A). The overlap of the p_z orbitals between two adjacent atoms (B) forms a π bond which is responsible for creating the valence (hole) and conduction (electron) bands in graphene (C).

It is the overlap of these bonds that is responsible for creating the valence (hole) band and conduction (electron) band. Since each p_z orbital has only one electron the resulting hole band is filled while conduction band is empty.

As a result of the bonding configuration mentioned above graphene is a very interesting material to study for many different reasons. One of the primary reasons is that, as mentioned above, in neutral graphene the Fermi surface crosses the intersections between the electron and hole bands, which are six points lying at the edge of Brillouin zone, called the Dirac points. They are so named because the low energy excitations in the neighborhood of these points are governed by a linear dispersion relation which means their behavior is described by the two dimensional massless Dirac equation [46] [47]. By calculating the band structure of graphene, which will be shown in the following section, we find that the Fermi velocity in graphene is approximately 300 hundred times smaller than the speed of light. This leads to the possibility of observing various quantum electrodynamics phenomena but at lower energy [48] [49].

In the following sections we will provide calculations for the electronic band structure of graphene followed by the mean field approach of the previous section, modified to account for the two component spinor nature of the graphene wave function, to describe exciton condensation in a double graphene layer system. Finally we will provide the results for an exciton condensation model that includes the effects of electron screening.

2.2.1 Band Structure

We begin with our tight binding Hamiltonian

$$H = -t \sum_{\mathbf{R}_{A_j}} \sum_{<>_j} \left[c^\dagger_{A_j} c_{B_{<>_j}} + c^\dagger_{B_{<>_j}} c_{A_j} \right] \tag{2.52}$$

where $c_{A_j}(c^\dagger_{A_j})$ destroys (creates) an electron at site A_j and $c_{B_{<>_j}}(c^\dagger_{B_{<>_j}})$ destroys (creates) an electron at one of the three nearest neighbor sites of A_j. Although our system does not posses full translational symmetry, the periodic structure of the lattice indicates that we may benefit by switching from a real space Hamiltonian to

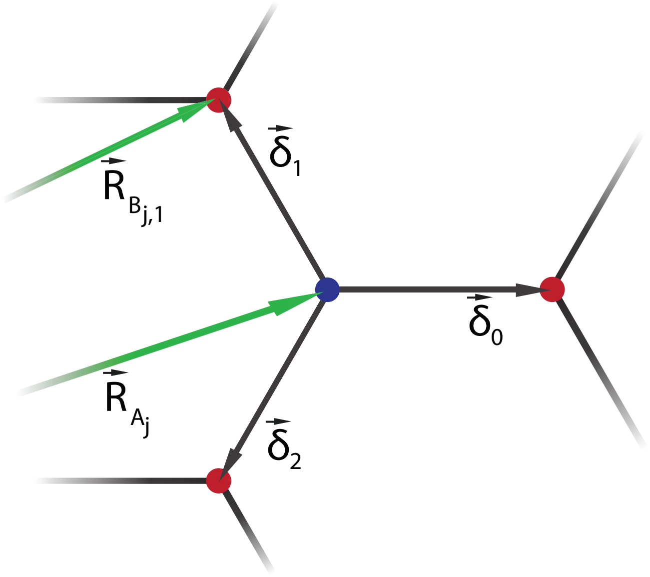

Fig. 2.20.: Image showing the relationship between the A and B sublattice sites. Here we have an A (blue) lattice site marked by the green position vector $\mathbf{R}_{A_j}$ connected to its three nearest neighbors on the B lattice (red) by the $\boldsymbol{\delta}_i$ vectors.

momentum space by using the Fourier transform. In order to perform the transform we will use the following definitions

$$c_{A_j} = \frac{1}{\sqrt{N_A}} \sum_{\mathbf{k}} e^{-i\mathbf{k}\cdot\mathbf{R}_{A_j}} c_{A_\mathbf{k}} \quad c_{B_{j,n}} = \frac{1}{\sqrt{N_B}} \sum_{\mathbf{k}} e^{-i\mathbf{k}\cdot\mathbf{R}_{B_{j,n}}} c_{B_\mathbf{k}} = \frac{1}{\sqrt{N_B}} \sum_{\mathbf{k}} e^{-i\mathbf{k}\cdot(\mathbf{R}_{A_j}+\boldsymbol{\delta}_n)} c_{B_\mathbf{k}}. \tag{2.53}$$

where $N_A(N_B)$ is the number of points on the A (B) lattice. For all subsequent calculations $N_A = N_B = N$. Using Eq. (2.53) in Eq. (2.52) we get

$$H = -t \sum_{\mathbf{R}_{A_j}} \left[\sum_{\mathbf{k}} e^{-i\mathbf{k}\cdot\mathbf{R}_{A_j}} c_{A^\dagger_\mathbf{k}} \sum_{\mathbf{k}'} \sum_{n} e^{-i\mathbf{k}'\cdot(\mathbf{R}_{A_j}+\boldsymbol{\delta}_n)} c_{B_{\mathbf{k}'}} + \text{h. c.} \right]. \tag{2.54}$$

By definition $\sum_{\mathbf{R}_{A_j}} e^{i(\mathbf{k}-\mathbf{k}')\cdot\mathbf{R}_{A_j}} = N\delta_{\mathbf{k},\mathbf{k}'}$ which gives

$$H = \sum_{\mathbf{k}} \begin{pmatrix} c^\dagger_{A_\mathbf{k}} & c^\dagger_{B_\mathbf{k}} \end{pmatrix} \begin{pmatrix} 0 & \phi(\mathbf{k}) \\ \phi^*(\mathbf{k}) & 0 \end{pmatrix} \begin{pmatrix} c_{A_\mathbf{k}} \\ c_{B_\mathbf{k}} \end{pmatrix} \tag{2.55}$$

where

$$\phi(\mathbf{k}) = -t\sum_{n=0}^{2} e^{-i\mathbf{k}\cdot\boldsymbol{\delta}_n} \tag{2.56}$$

determines the band structure of graphene and the energy eigenvalues for Eq. (2.55) are $E_{\pm,\mathbf{k}} = \pm|\phi(\mathbf{k})|$.

In order to better understand the band structure we would like to plot both the modulus and the phase of Eq. (2.56). As a first step we will start by expressing the nearest neighbor vectors in terms of their $\hat{\imath}$ and $\hat{\jmath}$ components as follows

$$\boldsymbol{\delta}_0 = a\hat{\imath} \tag{2.57}$$

$$\boldsymbol{\delta}_1 = -\frac{a}{2}\hat{\imath} + \frac{\sqrt{3}}{2}\hat{\jmath} = e^{i2\pi/3} \tag{2.58}$$

$$\boldsymbol{\delta}_2 = -\frac{a}{2}\hat{\imath} - \frac{\sqrt{3}}{2}\hat{\jmath} = e^{i4\pi/3} \tag{2.59}$$

which we can use to determine $\mathbf{k}\cdot\boldsymbol{\delta}_n$ starting with $\mathbf{k} = \mathrm{k}_x\hat{\imath} + \mathrm{k}_y\hat{\jmath}$. Using Eqs. (2.57-2.59) and the definition of $\mathbf{k}$ we have $\mathbf{k}\cdot\boldsymbol{\delta}_0 = k_x a$, $\mathbf{k}\cdot\boldsymbol{\delta}_1 = -\frac{1}{2}k_x a + \frac{\sqrt{3}}{2}k_y a$, and $\mathbf{k}\cdot\boldsymbol{\delta}_2 = -\frac{1}{2}k_x a - \frac{\sqrt{3}}{2}k_y a$ which we use to find the real and imaginary components of Eq. (2.56)

$$\Re(\phi(\mathbf{k}))/t = \cos(k_x a) + 2\cos\left(\frac{1}{2}k_x a\right)\cos\left(\frac{\sqrt{3}}{2}k_y a\right) \tag{2.60}$$

$$\Im(\phi(\mathbf{k}))/t = \sin(k_x a) - 2\sin\left(\frac{1}{2}k_x a\right)\cos\left(\frac{\sqrt{3}}{2}k_y a\right). \tag{2.61}$$

From Eq. (2.60) and Eq. (2.61) we find

$$|\phi(\mathbf{k})| = t\sqrt{1 + 4\cos\left(\frac{3}{2}k_x a\right)\cos\left(\frac{\sqrt{3}}{2}k_y a\right) + 4\cos^2\left(\frac{\sqrt{3}}{2}k_y a\right)} \tag{2.62}$$

$$\mathrm{Phase}[\phi(\mathbf{k})] = \tan^{-1}\left(\frac{\sin(k_x a) - 2\sin\left(\frac{1}{2}k_x a\right)\cos\left(\frac{\sqrt{3}}{2}k_y a\right)}{\cos(k_x a) + 2\cos\left(\frac{1}{2}k_x a\right)\cos\left(\frac{\sqrt{3}}{2}k_y a\right)}\right). \tag{2.63}$$

Figure 2.21 shows a plot the band structure of graphene, Eq. (2.62).

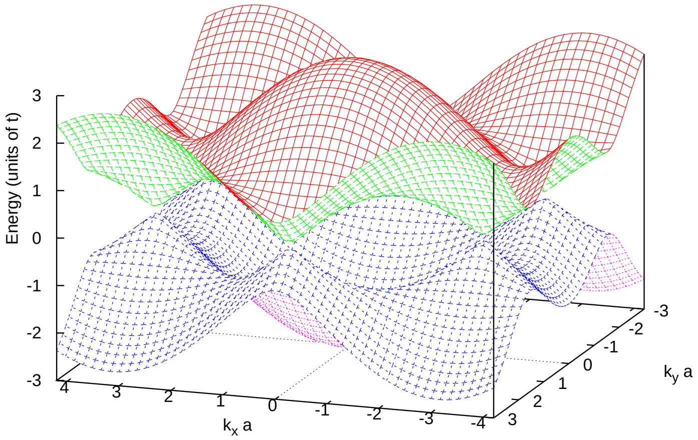

Fig. 2.21.: Electronic band structure of graphene. The top surface (red and green) represents the dispersion for the electron band while the bottom surface (blue and pink) represents the dispersion for the hole band. The figure shows that the surfaces meet at discrete points at $E = 0$. In neutral graphene, these points make up the “Fermi surface”.

From this figure we see that there are two bands. The upper (conduction) band shows the dispersion for electrons while the lower (valence) band shows the dispersion for holes. The two bands meet at a set of six discrete points at $E = 0$. For neutral graphene these six points make up the Fermi surface. In order to find the position of these points we set Eq. (2.60) and Eq. (2.61) equal to zero giving us

$$\cos(k_x a) = -2\cos\left(\frac{1}{2}k_x a\right)\cos\left(\frac{\sqrt{3}}{2}k_y a\right) \tag{2.64}$$

$$\sin(k_x a) = 2\sin\left(\frac{1}{2}k_x a\right)\cos\left(\frac{\sqrt{3}}{2}k_y a\right). \tag{2.65}$$

When we divide Eq. (2.65) by Eq. (2.64) we are left with

$$\cos(k_x a)\sin\left(\frac{1}{2}k_x a\right) + \sin(k_x a)\cos\left(\frac{1}{2}k_x a\right) = \sin\left(\frac{3}{2}k_x a\right) = 0 \tag{2.66}$$

which tells us that $k_x a = 2n\pi/3$ for $n = 0, \pm1, \pm2\ldots$. Using this result in Eq. (2.65) or Eq. (2.64) allows us to determine the points are located at $(0, \pm4\pi\sqrt{3}/9)$ and $(\pm2\pi/3, \pm2\pi\sqrt{3}/9)$. These points are located at the corners of the first Brillouin zone and are shown in Fig. 2.22(a) which means that the points corresponding to higher values of n would be located outside of the first Brillouin zone. Now although there are six points they are not all distinct. There are in fact two sets of three points where each point in a set is connected by translation along a reciprocal lattice vector, b_j, which is defined by $a_i b_j = 2\pi\delta_{ij}$ where a_i are the vectors given by Eqs. (2.57)-(2.59).

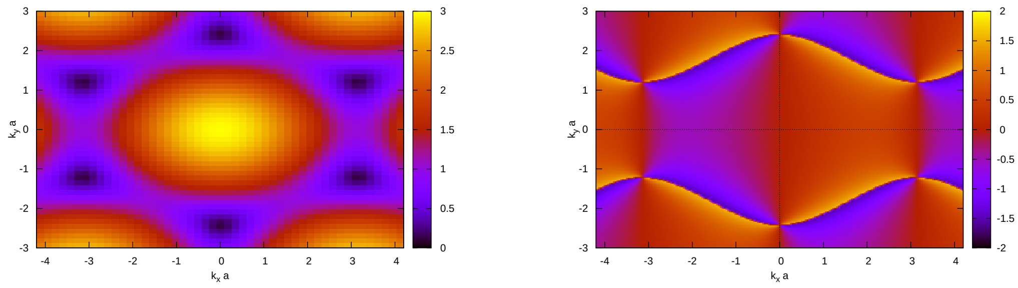

(a) (b)

Fig. 2.22.: Figures showing the modulus (a) and phase (b) of $\phi(\mathbf{k})$. Although there are six zero energy points they are not all distinct as can be shown by the grouping of points by translations along reciprocal lattice vectors.

This leaves us two distinct points which we will label as $\mathbf{K} = (2\pi/3, 2\pi\sqrt{3}/9)$ and $\mathbf{K}' = (2\pi/3, -2\pi\sqrt{3}/9)$. A way of visualizing this grouping by reciprocal lattice vectors is to plot Eq. (2.63) where we can see which points are equivalent and is shown in Fig. 2.22(b). Now that we have found where the **K** and **K**' points are we are interested in better understanding the dispersion around them. These would be the dispersion relations for low energy electrons and holes in our system and we will differentiate between the two dirac points by labeling them with a valley index. We begin by expanding Eq. (2.56) for small **k** around the **K** and **K**' points

$$\begin{aligned} \phi_{\mathbf{Q}}(\mathbf{k}) &= -\,t\sum_n e^{-i(\mathbf{Q}+\mathbf{k})\cdot\boldsymbol{\delta}_n} \qquad \mathbf{Q}\in\{\mathbf{K},\mathbf{K}'\} \\ &= -\,t\sum_n e^{-i\mathbf{Q}\cdot\boldsymbol{\delta}_n}\left[1 - i\mathbf{k}\cdot\boldsymbol{\delta}_n - \ldots\right] \end{aligned} \tag{2.67}$$

Because $\sum_{n=0}^{2} e^{-i\mathbf{Q}\cdot\boldsymbol{\delta}_n} = 0$ we have

$$\phi_{\mathbf{Q}}(\mathbf{k}) = it\mathbf{k}\cdot\sum_n \boldsymbol{\delta}_n e^{-i\mathbf{Q}\cdot\boldsymbol{\delta}_n} = it\mathbf{k}\cdot\mathbf{f}(\mathbf{Q}) \tag{2.68}$$

as the band structure for small **k** momentum around the **K** and **K**' points and

$$E = \pm t|\phi(\mathbf{k})| = \pm\frac{3}{2}at|\mathbf{k}| = \pm v_f|\mathbf{k}| \tag{2.69}$$

is the dispersion relation for low energy electrons and holes where $v_f \approx c/300$ is the Fermi velocity and c is the speed of light in a vacuum.

2.2.2 Mean-Field Analysis

In this section we derive equations similar to those derived in Sec. 2.1.2 but for a system composed of two layers of graphene, one separated from the other by a dielectric film of thickness d, where the upper contains electrons as charge carriers and the lower layer contains holes as charge carrier. Graphene is a very versatile material in the sense that it does not require doping at the time of manufacturing in order to adjust the polarity and concentration of charge carriers. We are able to adjust the carrier concentrations, in a continuous manner, from being hole doped to neutral to being electron doped through the use of applied voltages.

We begin, as we did in Sec. 2.1.2, by writing the non-interacting components of the Hamiltonian for such a system in which the spacing between the two graphene layers is such that we can neglect the tunneling between the layers. Recalling the

Hamiltonian for a single layer of graphene Eq. (2.55) and using the small momentum approximation Eq. (2.68) around the Dirac points we have

$$\hat{H}_0 = \sum_{\mathbf{k},\tau,\nu} \psi^\dagger_{\tau,\nu}(\mathbf{k})\mathcal{K}(\mathbf{k})\psi_{\tau,\nu}(\mathbf{k}) \tag{2.70}$$

where

$$\mathcal{K}(\mathbf{k}) = \begin{bmatrix} 0 & ke^{i\theta_k} & 0 & 0 \\ ke^{-i\theta_k} & 0 & 0 & 0 \\ 0 & 0 & 0 & ke^{-i\theta_k} \\ 0 & 0 & ke^{i\theta_k} & 0 \end{bmatrix} \tag{2.71}$$

with $\theta_{\mathbf{k}}$ defined in Eq. (2.63), $\hbar\mathbf{k}$ is the momentum of the particle, $\nu \in \{A, B\}$ is the layer index and $\tau \in \{K, K'\}$ is the valley index. As in our previous discussion we noted that the spin is preserved so we have omitted the sum over the spin. In this basis $\psi^\dagger_{\tau,\nu}(\mathbf{k})$ has the following form

$$\psi^\dagger_{\tau,\nu}(\mathbf{k}) = \left(c^\dagger_{K,A}(\mathbf{k}) c^\dagger_{K,B}(\mathbf{k}) c^\dagger_{K',A}(\mathbf{k}) c^\dagger_{K',B}(\mathbf{k}) \right). \tag{2.72}$$

The small-k approximation for the band structure that we have used in writing our Hamiltonian matrix implies that we are focusing on momentum transfers in the interaction that are not capable of causing the electrons to scatter from one valley,**K**, to the other, $\mathbf{K}'$. As a consequence of this we can reduce our matrix from 4 × 4 to 2 × 2 and just like the spin case we will omit the factor of two which gives us

$$\mathcal{K}(\mathbf{k}) = \begin{bmatrix} 0 & ke^{i\theta_k} \\ ke^{-i\theta_k} & 0 \end{bmatrix} \tag{2.73}$$

and

$$\psi^\dagger_{\tau,\nu}(\mathbf{k}) = \psi^\dagger_{\nu}(\mathbf{k}) = \left(c^\dagger_{A}(\mathbf{k}) c^\dagger_{B}(\mathbf{k}) \right). \tag{2.74}$$

Unlike in Sec. 2.1.2, $\hat{H}_0$ is not diagonal in our chosen basis so we perform a basis transformation to obtain

$$\hat{H}_0 = \sum_{\mathbf{k},\nu} \psi_\nu^\dagger(\mathbf{k})\mathcal{M}(\mathbf{k})\mathcal{E}(\mathbf{k})\mathcal{M}^\dagger(\mathbf{k})\psi_\nu(\mathbf{k}) \tag{2.75}$$

where

$$\mathcal{E}(\mathbf{k}) = \begin{bmatrix} -v_F\hbar k & 0 \\ 0 & v_F\hbar k \end{bmatrix} \text{ and } \mathcal{M}(\mathbf{k}) = \frac{1}{\sqrt{2}}\begin{bmatrix} 1 & 1 \\ -e^{-i\theta_k} & e^{-i\theta_k} \end{bmatrix}. \tag{2.76}$$

We now define our new states as a superposition of our previous operators as

$$c_s(\mathbf{k}) = \frac{c_A(\mathbf{k}) + sc_B(\mathbf{k})e^{i\theta_\mathbf{k}}}{\sqrt{2}} \quad \Rightarrow \quad |\mathbf{k}, s\rangle = \frac{1}{\sqrt{2}}\begin{pmatrix} 1 \\ se^{i\theta_\mathbf{k}} \end{pmatrix} \tag{2.77}$$

where $s \in \{-1, 1\}$ represents the electron, $s = -1$, and hole, $s = 1$, bands. The vast majority of the calculation of the mean field hamiltonian in the case of double layer graphene is the same as that for double quantum well systems and as such we will not repeat it here. There is a difference though and that arises when we need to calculate the interaction matrix elements $\langle \mathbf{k}_4, s_4, \mathbf{k}_3, s_3|V|\mathbf{k}_2, s_2, \mathbf{k}_1, s_1\rangle$. By inserting four complete sets of states we have

$$\begin{aligned} \langle \mathbf{k}_4, s_4, \mathbf{k}_3, s_3|V|\mathbf{k}_2, s_2, \mathbf{k}_1, s_1\rangle = \int d\mathbf{r}_4\, d\mathbf{r}_3\, d\mathbf{r}_2\, d\mathbf{r}_1\, \langle \mathbf{k}_4|\mathbf{r}_4\rangle\langle \mathbf{k}_3|\mathbf{r}_3\rangle\times \\ \langle \mathbf{r}_4\mathbf{r}_3|V|\mathbf{r}_2\mathbf{r}_1\rangle\langle \mathbf{r}_2|\mathbf{k}_2\rangle\langle \mathbf{r}_1|\mathbf{k}_1\rangle\langle s_4|s_1\rangle\langle s_3|s_2\rangle \end{aligned} \tag{2.78}$$

Due to the form of the interaction we know that $\mathbf{r}_4 = \mathbf{r}_1$ and $\mathbf{r}_3 = \mathbf{r}_2$ which means

$$\begin{aligned} \langle \mathbf{k}_4, s_4, \mathbf{k}_3, s_3|V|\mathbf{k}_2, s_2, \mathbf{k}_1, s_1\rangle = \int d\mathbf{r}_2\, d\mathbf{r}_1\, \langle \mathbf{k}_4|\mathbf{r}_1\rangle\langle \mathbf{k}_3|\mathbf{r}_2\rangle\times \\ V(|\mathbf{r}_1 - \mathbf{r}_2|))\langle \mathbf{r}_2|\mathbf{k}_2\rangle\langle \mathbf{r}_1|\mathbf{k}_1\rangle\langle s_4|s_1\rangle\langle s_3|s_2\rangle. \end{aligned} \tag{2.79}$$

We are interested in evaluating the product $\langle s_4|s_1\rangle\langle s_3|s_2\rangle$ which is the additional component, compared to the double quantum well case, that we have gained due to the spinor nature of the single particle wave function. This product is

$$\begin{aligned}4\langle s_4|s_1\rangle\langle s_3|s_2\rangle =& \left[1+s_4s_1e^{-i(\theta_{\mathbf{k}_4}-\theta_{\mathbf{k}_1})}\right]\left[1+s_3s_2e^{-i(\theta_{\mathbf{k}_3}-\theta_{\mathbf{k}_2})}\right]\\ =&1+s_4s_1e^{-i(\theta_{\mathbf{k}_4}-\theta_{\mathbf{k}_1})}+s_3s_2e^{-i(\theta_{\mathbf{k}_3}-\theta_{\mathbf{k}_2})}+s_4s_3s_2s_1e^{-i(\theta_{\mathbf{k}_4}-\theta_{\mathbf{k}_1}+\theta_{\mathbf{k}_3}-\theta_{\mathbf{k}_2})}\end{aligned} \tag{2.80}$$

Due to momentum conservation we have, $\theta_{\mathbf{k}_4}-\theta_{\mathbf{k}_1}=-\theta_{\mathbf{k}_3}+\theta_{\mathbf{k}_2}$,

$$4\langle s_4|s_1\rangle\langle s_3|s_2\rangle = 1+s_4s_1\left(e^{i\theta_{\mathbf{k}}}+\frac{s_3s_2}{s_4s_1}e^{-i\theta_{\mathbf{k}}}\right)+s_4s_3s_2s_1 \tag{2.81}$$

where $\Delta\theta_{\mathbf{k}}=\theta_{\mathbf{k}_3}-\theta_{\mathbf{k}_2}$ which leads to

$$\langle s_4|s_1\rangle\langle s_3|s_2\rangle = \begin{cases}\frac{1}{2}\left(1-\cos\theta_{\mathbf{k}}\right) & s_4s_1=-1 \quad s_3s_2=-1\\ \frac{1}{2}\left(1+\cos\theta_{\mathbf{k}}\right) & s_4s_1=+1 \quad s_3s_2=+1\\ \frac{i}{2}\sin\theta_{\mathbf{k}} & s_4s_1=+1 \quad s_3s_2=-1\\ -\frac{i}{2}\sin\theta_{\mathbf{k}} & s_4s_1=-1 \quad s_3s_2=+1\end{cases} \tag{2.82}$$

A particle that is flipped from an electron band to a hole band or vice versa, is represented by $s_is_j=-1$, which requires a momentum transfer of $2\pi/a$ which we have already said we are not considering since this would not preserve the valley index as a good quantum number. With this consideration the only effect of the spinor nature of the single particle wavefunction is to modify the equation for the order parameter Eq. (2.41) to

$$\Delta(\mathbf{k}) = -\frac{1}{2}\sum_{\mathbf{k}'}V_{eh}(|\mathbf{k}-\mathbf{k}'|)(1+\cos\phi_{\mathbf{k}'})\frac{\Delta(\mathbf{k}')}{\sqrt{\xi^2(\mathbf{k}')+\Delta^2(\mathbf{k}')}}. \tag{2.83}$$

Using this mean field approximation the MacDonald group recently published a paper [50] discussing the possibility of observing exciton condensation in double layer graphene at room temperature. Gilbert and Shumway followed a very different path in their paper [51] but arrived at a similar conclusion. The possibility of observing quantum effects at high temperatures is of course very interesting. But, at about the same time that the MacDonald group published their work Kharitonov and Efetov published their work [52] showing essentially different results. Their claim is that once you take into account the effects of electron-electron screening in the system, the critical temperature, T_c, is reduced from room temperature to mK. In the following section we turn to the problem of including the effect of electron-electron screening on the formation of an exciton condensate in our double layer graphene system using the mean field approximation.

2.3 Electron Screening

> I used to wonder how it comes about that the electron is negative. Negative-positive–these are perfectly symmetric in physics. There is no reason whatever to prefer one to the other. Then why is the electron negative? I thought about this for a long time and at last all I could think was 'It won the fight!' (Albert Einstein)

Electron screening is a fundamental effect in condensed matter physics. If we begin with a homogenous electron gas and we place a negative test charge in the gas the electrons in the gas will be forced away from the test charge due to Coulomb repulsion which results in a positively charged screening cloud around the test charge due to the positive background. As the test charge moves through the gas the screening cloud moves with it. This means that mutual repulsion between our test charge and the gas helps to move the electrons in the gas out of they way of our test charge. A result of this screening cloud is to change the normally long range Coulomb interaction to a shorter ranged one. The simplest model for electron screening, the Thomas-Fermi model, changes the algebraic Coulomb interaction into an exponential interaction. Although this model overestimates the strength of the screening effect it provides a relatively simple illustration of how to approach the problem of electron screening.

To include the effects of screening in a condensed matter system essentially means that we must calculate the dynamic dielectric response function, $\epsilon(\mathbf{q}, \omega)$, of our material. In the following sections we will show the calculation of ϵ for the Thomas-Fermi model, since it is the simplest and easiest to understand, and for the random phase approximation (RPA). After obtaining the expression for the dielectric response function using RPA we will conclude with a discussion of its use in the literature as it applies to the formation of an exciton condensate in double layer graphene [52].

2.3.1 Basic Theory

Dielectric Response Function

In order to derive the expression for the dielectric response function we begin with the equations governing the displacement field, **D**, and the electric field, **E**, inside a polarizable medium,

$$\nabla \cdot \mathbf{D}(\mathbf{r}) = 4\pi\rho_i(\mathbf{r}), \tag{2.84}$$

$$\nabla \cdot \mathbf{E}(\mathbf{r}) = 4\pi[\rho_i(\mathbf{r}) + \rho_s(\mathbf{r}). \tag{2.85}$$

Here $\rho_i(\mathbf{r})$ is an impurity charge density which contains a net charge of $\mathcal{Q}_i = \int d\mathbf{r}\rho_i(\mathbf{r})$ and $\rho_s(\mathbf{r})$ is the resulting screening charge density containing $-\mathcal{Q}_i$ surrounding $\rho_i(\mathbf{r})$ such that at large distances from impurity position the net electric field is zero. By considering a translationally invariant system the Fourier transforms of Eq. (2.84) and Eq. (2.85) become

$$i\mathbf{k} \cdot \mathbf{D}(\mathbf{k}) = 4\pi\rho_i(\mathbf{k}), \tag{2.86}$$

$$i\mathbf{k} \cdot \mathbf{E}(\mathbf{k}) = 4\pi[\rho_i(\mathbf{k}) + \rho_s(\mathbf{k})]. \tag{2.87}$$

Since our goal is to understand the effects of electronic screening in relation to excitonic condensation in graphene we shall concern ourselves with the longitudinal components of Eq. (2.86) and Eq. (2.87)

$$D_l(\mathbf{k}) = \frac{4\pi}{ik}\rho_i(\mathbf{k}) \tag{2.88}$$

$$E_l(\mathbf{k}) = \frac{4\pi}{ik}[\rho_i(\mathbf{k}) + \rho_s(\mathbf{k})] \tag{2.89}$$

$$\phi(\mathbf{k}) = \frac{4\pi}{k^2}[\rho_i(\mathbf{k}) + \rho_s(\mathbf{k})] \tag{2.90}$$

where $\phi(\mathbf{k})$ is the scalar potential defined by $E = -\nabla\phi$, or equivalently $\phi(\mathbf{k}) = iE_l(\mathbf{k})/k$. The dielectric response function, $\epsilon(\mathbf{k})$, is then defined as the ratio of $D_l(k)/E_l(k)$ in the limit of $\rho_i \to 0$

$$\epsilon(\mathbf{k}) = \lim_{\rho_i\to 0} \frac{D_l(\mathbf{k})}{E_l(\mathbf{k})} = \lim_{\rho_i\to 0} \left[\frac{\rho_i(\mathbf{k})}{\rho_i(\mathbf{k}) + \rho_s(\mathbf{k})}\right]. \tag{2.91}$$

By rewriting Eq. (2.90) in terms of Eq. (2.91) we have, for nonzero $\rho_i(\mathbf{k})$,

$$\phi(\mathbf{k}) = \frac{4\pi}{k^2}\frac{\rho_i(\mathbf{k})}{\epsilon(\mathbf{k})} \tag{2.92}$$

$$\phi(\mathbf{r}) = \int \frac{d\mathbf{k}}{(2\pi)^3}\frac{4\pi}{k^2}\frac{\rho_i(\mathbf{k})}{\epsilon(\mathbf{k})}e^{i\mathbf{k}\cdot\mathbf{r}} \tag{2.93}$$

the total potential which includes the the potential from the impurity charge as well as the the screening charge. Although no one has yet been able to find the exact solution to Eq. (2.91) there are have been many approximations that have been developed. In the following sections we will discuss in detail two of them.

Thomas-Fermi

The Thomas-Fermi approximation was discovered independently by Thomas in 1927 [53] and Fermi in 1928 [54]. We begin by assuming we have an impurity charge, Q, located at the origin such that in the absence of the electron gas an electron at a distance of r from the origin would feel a potential of $\phi(\mathbf{r}) = Q/r$. Its potential energy, U, is given by

$$U(\mathbf{r}) = -e\phi(\mathbf{r}) = -e\frac{Q}{r}. \tag{2.94}$$

When the electron gas is included the potential ϕ will be screened. The screening charge is the difference between the charge density of the electron gas with and without Q. If we let this difference be $-e\delta n(\mathbf{r})$ then Poisson's equation for the total charge density is

$$-\nabla^2\phi_{eff}(\mathbf{r}) = 4\pi[Q\delta(\mathbf{r}) - e\delta n(\mathbf{r})], \tag{2.95}$$

where $\phi_{eff}(\mathbf{r})$ is the true potential of Q in the presence of the electron gas which depends on the screening charge $-e\delta n(\mathbf{r})$. By using the Fourier transform on Eq. (2.95) we find

$$k^2 U_{eff}(\mathbf{k}) = -4\pi eQ + 4\pi e^2\delta n(\mathbf{k}). \tag{2.96}$$

In order to proceed we must make some approximation for the screening charge. In the Thomas-Fermi approximation the electron gas is assumed to behave locally as if it were a free electron gas. What this means is that we are assuming that the potential is a slowly varying function of distance whose scale is set by the Fermi wavelength. The consequence of this assumption is that the chemical potential for the system is locally shifted by $U_{eff}(\mathbf{r})$, $\mu \to \mu + U_{eff}(\mathbf{r})$. Next, we define a new single-particle energy

$$\varepsilon_{\mathbf{k}}(\mathbf{r}) = \frac{\hbar^2 k^2}{2m} + U_{eff}(\mathbf{r}) \tag{2.97}$$

which gives us an effective Fermi-Dirac distribution of $n_{\mathbf{k}}(\mathbf{r}) = 1/(1 + e^{\beta(\varepsilon_{\mathbf{k}}(\mathbf{r})-\mu)})$ and gives an effective electron number density at $\mathbf{r}$

$$\begin{aligned}\langle n(\mathbf{r})\rangle =& 2\int \frac{d\mathbf{k}}{(2\pi)^3} n_{\mathbf{k}}(\mathbf{r}) \\ =& n_e - 2\int \frac{d\mathbf{k}}{(2\pi)^3}\frac{1}{1 + e^{\beta(\varepsilon_{\mathbf{k}}(\mathbf{r})-\mu)}} \\ \simeq& n_e - \frac{\partial n_e}{\partial \mu} U_{eff}(\mathbf{r}),\end{aligned} \tag{2.98}$$

where we have included a spin factor of 2 and we have retained only the term linear in $U_{eff}(\mathbf{r})$ in the last line. This is valid if $\varepsilon \gg U_{eff}(\mathbf{r})$. Using Eq. (2.98) we are now able to calculate the screening charge because

$$\delta n(\mathbf{r}) = \langle n(\mathbf{r})\rangle - n_e = -\frac{\partial n_e}{\partial \mu} U_{eff}(\mathbf{r}) \tag{2.99}$$

which gives

$$k^2 U_{eff}(\mathbf{k}) = -4\pi e \left(Q + e\frac{\partial n_e}{\partial \mu} \right) \tag{2.100}$$

or

$$U_{eff}(\mathbf{k}) = \frac{-4\pi e Q}{k^2 + k_{TF}^2}, \tag{2.101}$$

where $k_{TF}^2 = 4\pi e^2 \partial n_e / \partial \mu$ is the Thomas-Fermi screening wave vector. Taking the inverse Fourier transform of $U_{eff}(\mathbf{k})$, we obtain the real space potential energy $U_{eff}(\mathbf{r})$ of an electron with a charge Q located at the origin,

$$\begin{aligned} U_{eff}(\mathbf{r}) &= -\, e \int \frac{d\mathbf{k}}{(2\pi)^3} \frac{4\pi}{k^2} \frac{\rho_i(k)}{1 + k_{TF}^2/k^2}, && (2.102) \\ &= -\, \frac{eQ}{i\pi r} \int_{-\infty}^{\infty} dk \frac{k^2 e^{ikr}}{k^2 + k_{TF}^2} \\ U_{eff}(\mathbf{r}) &= -\, \frac{eQ}{r} e^{-k_{TF} r} && (2.103) \end{aligned}$$

where $\rho_i(k) = Q$. Comparing Eq. (2.102) to Eq. (2.93) we find that for the Thomas-Fermi approximation the dielectric function is given by

$$\epsilon(k) = 1 + \frac{k_{TF}^2}{k^2} \tag{2.104}$$

For metals the Thomas-Fermi wave vector is typically on the order of 1 Å. We can express k_{TF} in terms of atomic units by using

$$a_0 k_{TF} = \left(\frac{4}{\pi} k_F a_0 \right)^{1/2} \approx \frac{1.5632}{\sqrt{r_s}}, \tag{2.105}$$

where $a_0 = 4\pi\epsilon_0\hbar^2/m_e e^2$ is the Bohr radius, and $r_s^3 = 3/4\pi n_0 a_0^3$. This result for screening is only valid in describing the long range falloff of the potential surrounding the impurity charge and only models a static dielectric function in three dimensions. For distance comparable to the inter-particle spacing and a dynamic response a more accurate approximation is required. One such improvement is discussed in the next section.

Random Phase Approximation

The random phase approximation (RPA), also known as Lindhard dielectric function [55], is used to model both a static or dynamic dielectric function. We will start with a basic introduction to the RPA and then move on to how it has been applied to problem of excitonic condensation in graphene. We begin our derivation with

$$U_{eff}(\mathbf{r}, t) = U(\mathbf{r}) + \int d\mathbf{r}' e^2 \frac{\delta n(\mathbf{r}', t)}{|\mathbf{r} - \mathbf{r}'|}, \tag{2.106}$$

where $U(r)$ is the local potential energy due to a charge Q located at the origin. By taking the Fourier transform we have

$$U_{eff}(\mathbf{k}, \omega) = U(\mathbf{k}) + U(\mathbf{k})\delta n(\mathbf{k}, \omega), \tag{2.107}$$

where $U(\mathbf{k}) = 4\pi e^2/k^2$ for three dimensions. By using linear response theory [16] we can express the density fluctuation as $\delta n(\mathbf{r}, t)\rangle = \langle n(\mathbf{r}, t) - n_e = \int d\mathbf{r}' \chi_{sc}(\mathbf{r}, \mathbf{r}', t) U_{eff}(\mathbf{r}')$ which defines the screening function $\chi_{sc}(\mathbf{k}, \omega)$. Using this definition in Eq. (2.107) we get

$$U_{eff}(\mathbf{k}, \omega) = [1 - U(\mathbf{k})\chi_{sc}(\mathbf{k}, \omega)]^{-1} U(\mathbf{k}) \tag{2.108}$$

or alternatively

$$U_{eff}(\mathbf{k}, \omega) = U(\mathbf{k}) + U(\mathbf{k})\chi_{sc}(\mathbf{k}, \omega)U(\mathbf{k}) + U(\mathbf{k})\chi_{sc}(\mathbf{k}, \omega)U(\mathbf{k})\chi_{sc}(\mathbf{k}, \omega)U(\mathbf{k}) + \cdots . \tag{2.109}$$

We can represent Eq. (2.109) as a sum of Feynman diagrams as shown in Fig. 2.23. In each diagram $V(q)$ is bare Coulomb interaction which is decoupled from the momentum summation at each particle-hole bubble since it carriers away only the momentum exchanged in the bubble.

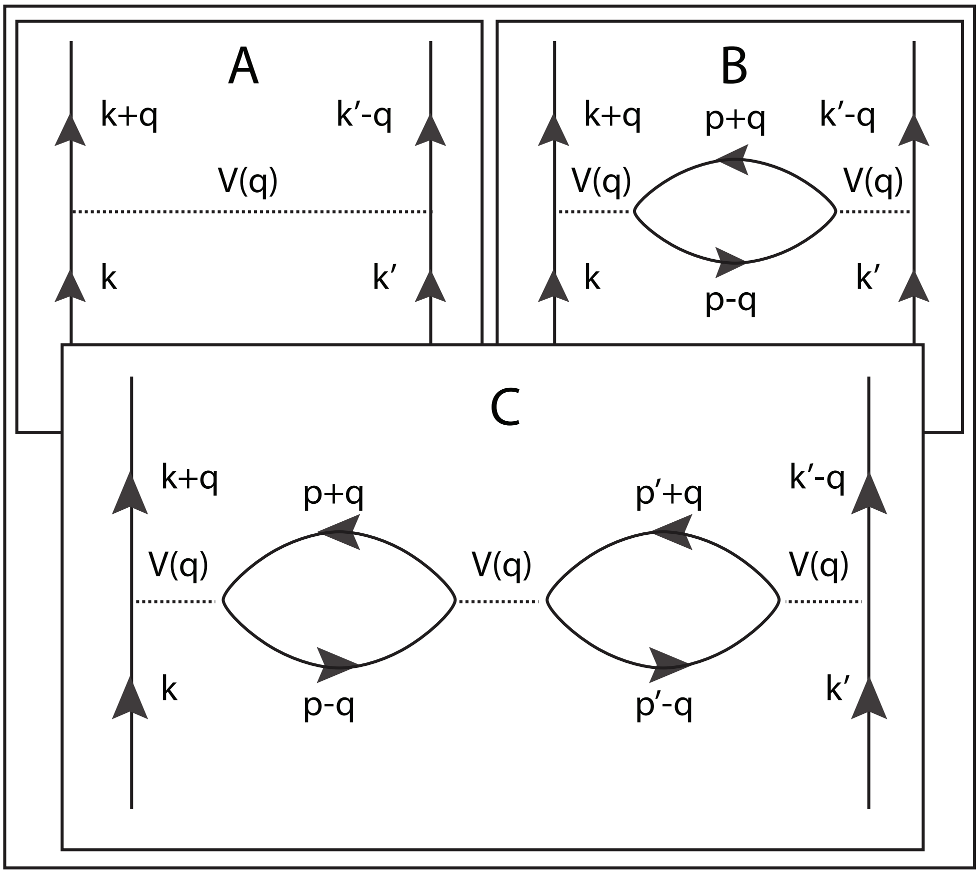

Fig. 2.23.: The random phase approximation is a summation of an infinite number of terms, three of which are shown. (A) is the bare Coulomb interaction, (B) the interaction containing one particle-hole bubble, (C) containing two particle-hole bubbles. The decoupling of the Coulomb interaction from the momentum summation at each bubble is what allows the approximation to be summed exactly to Eq. (2.108).

Remembering that our goal is to calculate the dielectric response function in the RPA framework we start with the result for the screening function

$$\chi_{sc}(\mathbf{k},\omega) = \lim_{\eta\to 0}\int_{-\infty}^{\infty}\frac{d\omega'}{2\pi\hbar}\frac{n_e S_0(k,\omega')(1-e^{-\beta\hbar\omega'})}{\omega-\omega'+i\eta}, \tag{2.110}$$

where $S_0(\mathbf{k},\omega')$ is the dynamic structure factor given by

$$n_e S_0(\mathbf{k},\omega) = \begin{cases} \frac{m^2\omega}{\pi\hbar^2 k} & 0<\omega<\omega_1 \\ \frac{m}{2\pi k\hbar^3\left[(mv_F)^2-\left(\frac{m}{\hbar k}\left(\hbar\omega-\frac{(\hbar k)^2}{2m}\right)\right)^2\right]} & \omega_1<\omega<\omega_2 \\ 0 & \omega<\omega_2 \end{cases} \tag{2.111}$$

with $\omega_1 = \hbar k v_F - (\hbar k)^2/2m$ and $\omega_2 = \hbar k v_F + (\hbar k)^2/2m$ [16] where k is measured from the Fermi surface. Remembering that $\epsilon(\mathbf{k},\omega) = 1 - 4\pi e^2\chi_{sc}(\mathbf{k},\omega)/k^2$ we find, due to Eq. (2.111), that

$$1+\epsilon_R(\mathbf{k},\omega) = 1-\frac{4\pi e^2}{k^2}\mathcal{P}\int_{-\infty}^{\infty}\frac{d\omega'}{2\pi\hbar}\frac{n_e S_0(\mathbf{k},\omega')(1-e^{-\beta\hbar\omega'})}{(\omega-\omega')} \tag{2.112}$$

and

$$\epsilon_I(\mathbf{k},\omega) = \frac{2\pi e^2}{k^2\hbar}n_e S_0(\mathbf{k},\omega)(1-e^{-\beta\hbar\omega}) \tag{2.113}$$

where ϵ_R (ϵ_I) is the real (imaginary) component of the dielectric function and $\mathcal{P}$ denotes the Cauchy principle value. These components are of course related through the Kramers-Kronig relation [56] [57]

$$\begin{aligned} \epsilon_R(\mathbf{k},\omega) =& \frac{\mathcal{P}}{\pi}\int_{-\infty}^{\infty}\frac{d\omega'\epsilon_I(\mathbf{k},\omega')}{\omega'-\omega} && (2.114)\\ \epsilon_I(\mathbf{k},\omega) =& -\frac{\mathcal{P}}{\pi}\int_{-\infty}^{\infty}\frac{d\omega'\epsilon_R(\mathbf{k},\omega')}{\omega'-\omega}. && (2.115) \end{aligned}$$

For $T=0$ Lindhard [55] showed that the real component to the dielectric function is given by

$$\begin{aligned} \epsilon_R = \frac{k_{TF}^2}{k^2}\Bigg\{\frac{1}{2}+\frac{k_F}{4k}\Bigg[&\left(1-\frac{(\omega-\hbar k^2/2m)^2}{\hbar^2k^2v_F^2}\right)\ln\left|\frac{\omega-kv_F-\hbar k^2/2m}{\omega+kv_F-\hbar k^2/2m}\right| \\ &+\left(1-\frac{(\omega+\hbar k^2/2m)^2}{\hbar^2k^2v_F^2}\right)\ln\left|\frac{\omega+kv_F+\hbar k^2/2m}{\omega-kv_F+\hbar k^2/2m}\right|\Bigg]\Bigg\}. \end{aligned} \tag{2.116}$$

In order to see the connection between what we have just derived, the RPA, and the previous Thomas-Fermi model we consider the static limit of Eq. (2.116),

$$\epsilon(x, \omega = 0) = 1 + \frac{k_{TF}^2}{k^2}\left[\frac{1}{2} + \frac{1-x^2}{4x}\ln\left|\frac{1+x}{1-x}\right|\right], \tag{2.117}$$

where $x = k/2k_F$. In the limit that $x \to 0$ we find that $\epsilon(x, \omega = 0) = 1 + k_{TF}^2/k^2$ which is exactly the result for the Thomas-Fermi approximation. Using the relationship $U_{eff}(\mathbf{k}, \omega) = U(\mathbf{k}, \omega)/\epsilon(\mathbf{k}, \omega)$ we find for the electron gas, $U(\mathbf{k}, \omega = 0) = 4\pi e^2/k^2$, that the effective potential is given by

$$\phi_{eff}(\mathbf{r}) = 4\pi e \int \frac{d\mathbf{k}}{(2\pi)^3} \frac{e^{-i\mathbf{k}\cdot\mathbf{r}}}{k^2 + k_{TF}^2\left[\frac{1}{2} + \frac{1-x^2}{4x}\ln\left|\frac{1+x}{1-x}\right|\right]}. \tag{2.118}$$

When $k \to 2k_F$ or $x \to 1$ the term in brackets in the denominator is logarithmically divergent and leads to a potential of the form

$$\phi_{eff}(\mathbf{r}) \sim \frac{\cos(2k_F r)}{r^3} \tag{2.119}$$

which shows that for $r \geq 1/2k_F$ the potential oscillates. These oscillations are known as Friedel oscillations [58]. We also see that the effect of screening is not large enough to give rise to the exponential decay predicted by the Thomas-Fermi model. Both Kohn and Luttinger [59] established that the negative contributions from the effective potential would give rise to superconducting instability at $T = 0$. What this implies is that the electron gas can become superconducting without the assistance of phonons which are required in the Bardeen-Cooper-Schrieffer (BCS) theory. Now that we have a basic understanding of the role of electron screening we turn to its application to exciton condensation in double layer graphene.

2.3.2 RPA in Double Layer Graphene

The possibility of room temperature exciton condensation in double layer graphene systems has been the focus of some research in recent years [34] [50] [51] [52]. MacDonald *et. al.* [50] argue that the possibility of nearly room temperature condensation is a result of the interaction between electrons and holes over the entire band as opposed to being a phonon-mediated interaction that only occurs within a small shell centered at the Fermi surface. In addition to this, due to graphene's linear dispersion at the Dirac points the charge carrier density that can be induced by applying external electric fields varies much more rapidly than is the case for a typical semi-conductor with a quadratic dispersion and a band gap allowing for a larger carrier density with a lower external field. In the limit of unscreened interactions MacDonald *et. al.* were able to show that if the Fermi energy was raised to $\sim 0.3\,\mathrm{eV}$, corresponding to a carrier density of $\sim 10^{13}\,\mathrm{cm}^2$, with a separation distance between layers of $\sim 2\,\mathrm{nm}$ that T_c would be $\sim 0.1E_F$. They also acknowledge that the addition of electron screening to the problem has the potential to significantly reduce the critical temperature.

We have seen multiple reports that suggest that the possibility of creating an exciton condensate for high temperature, if not room temperature, exists for the double layer graphene system. The opposite view is taken by Kharitonov and Efetov [52]. Their argument is that when screening is accounted for, the highest possible critical temperature is on the order of mK. To arrive at this conclusion they have made a few assumptions in order to be able to analytically solve the mean field equations. One such assumption is that the presence of the in-plane exchange interaction reduces the strength of the condensate order parameter. In order to investigate this assumption we have solved the mean-field equations, Eq. (2.40)-Eq. (2.42), for both a Coulomb and a Gaussian interaction with and without the in-plane exchange term. Figure 2.24(a) shows the result of this calculation for the Coulomb interaction where the upper curve is the order parameter without in-plane exchange contribution and the lower curve is with it. This result is further confirmed by Fig. 2.24(b) where we have used a Gaussian interaction, $V(\mathbf{q}) = e^{-q/2}$, in place of the Coulomb interaction. Once again, we see a reduction in the strength of the order parameter for the upper curve, containing no in-plane exchange interaction, to the lower curve that does contain the interaction. Due to these results it seems reasonable to conclude that the only consequence of the in-plane exchange contribution is to lower the critical temperature.

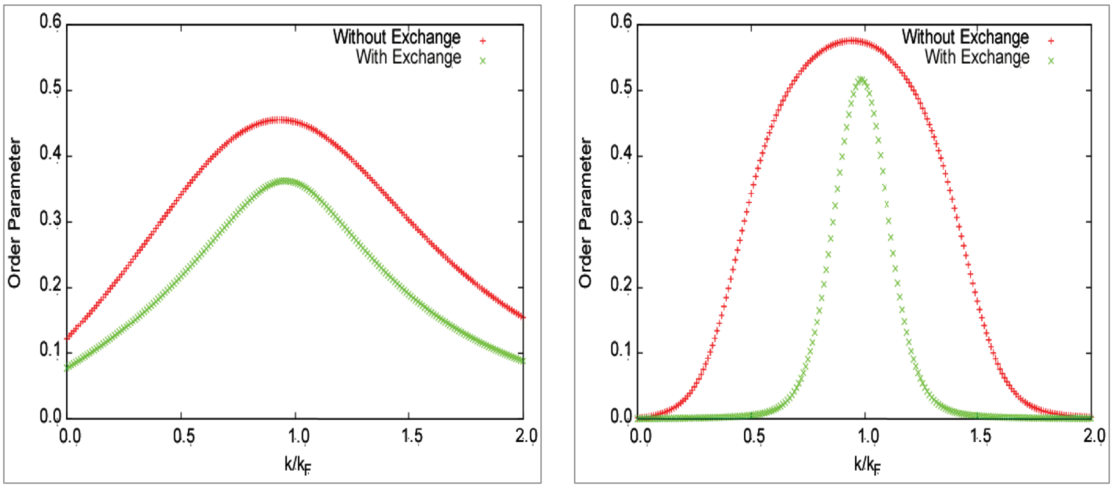

(a) (b)

Fig. 2.24.: Curves showing the exciton order parameter in double layer graphene with (lower) and without (upper) the inclusion of in-plane exchange interaction. In (a) the in-plane interaction is Coulomb, $V(\mathbf{q}) = 1/q$, and in (b) it is Gaussian, $V(\mathbf{q}) = e^{-q/2}$. For both figures the interlayer separation, $dk_F = 1$ and the length scale, $\alpha/k_F = 1$.

We next turn to the second assumption in [52]. It is that the number of electron species in the double layer graphene system is large enough that the interaction strength is reduced by a significant enough amount to warrant the application of a weak-coupling BCS approach to the problem. What this means is that they assume the order parameter is constant and non-zero only for an area that is centered on the Fermi surface and extends only by an amount equal to the Debye screening length as shown, schematically, in Fig. 2.25 by the black line.

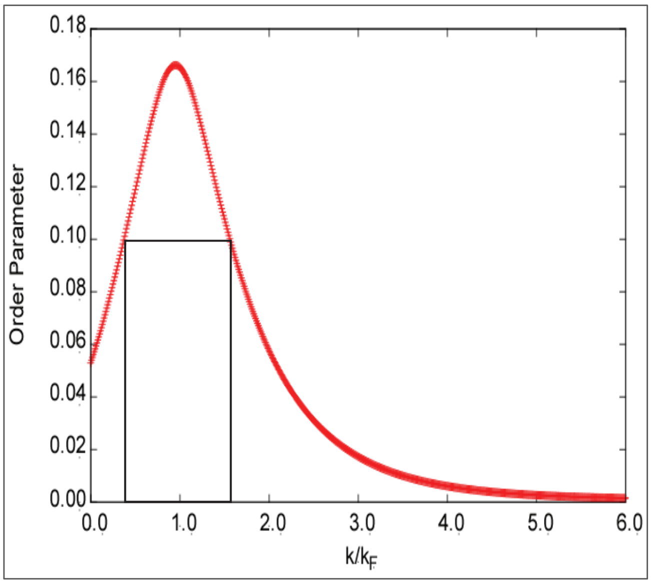

Fig. 2.25.: The curve shows a typical result for the exciton order parameter in the self-consistent mean-field approximation. The black rectangle shows the approximation to the order parameter used by Efetov [52] in order to analytically derive the effect of electron-electron screening in double layer graphene. The assumption is that the order parameter is constant and non-zero only for values of $\mathbf{k}$ symmetric about k_F and extending to the inverse Debye screening length.

The figure shows a typical result, the curve, for the order parameter obtained by using the mean-field approach and a representation of the BCS approach by the column. As we can see there is significant differences between the two. The constant order parameter assumption means that the maximum of the order parameter should vary exponentially with the electron degeneracy, g, as $\Delta \sim e^{-g}$. In order to investigate this we have performed the calculation of the order parameter, once again in the mean-field approach, as a function of electron degeneracy. Figure 2.26 shows the results of such a calculation. While it is true the effect of increasing electron degeneracy does suppress the condensate, this suppression is *not exponential*.

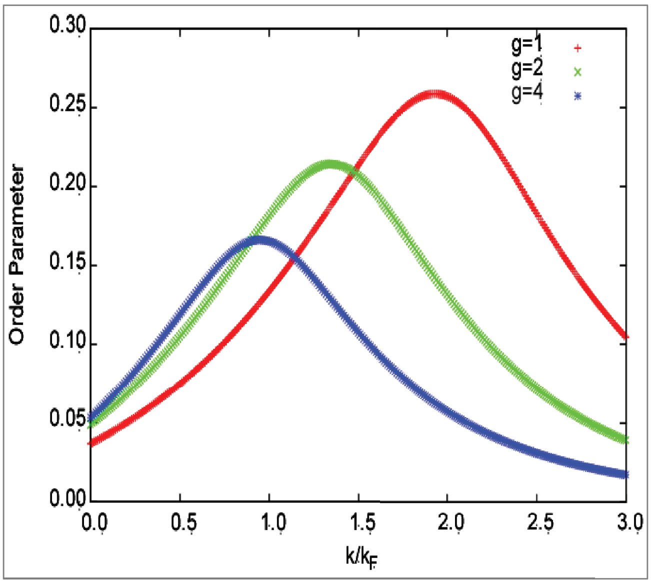

Fig. 2.26.: Curves showing the exciton order parameter in double layer graphene without an in-plane interaction, obtained by and using the RPA screened potential $V_{sc}(\mathbf{q}) = e^{-qd}/(q+2\chi+\chi^2[1-exp[-2qd]]/q)$ obtained in Efetov [52] for three different values of the electron degeneracy, g. The interlayer separation is $dk_F = 1$, the length scale $\alpha/k_F = 1$ and $\chi = \alpha g$.

2.4 Conclusions

> The true laboratory is the mind, where behind illusions we uncover the laws of truth. (Jagadish Chandra Bose)

In this chapter we have presented the development of a set of self-consistent mean field equations, for both double quantum well systems with quadratically dispersing charge carriers and double layer graphene with linearly dispersion charge carriers, that are used to explore the properties of exciton condensation in these systems. In addition to this we have discussed the single exciton problem in the context of double quantum well systems and provided a means for determining, on the basis of the density parameter $r_s = \sqrt{1/(\pi a_0 n)}$, whether the excitons can be considered to be non-interacting. Finally we have discussed the role that electron-electron screening plays on the formation of a condensate in double layer graphene. Our results indicate that the condensate does not decay exponentially with the number of electron species.

As was noted above, these results depended upon our solving the Schrödinger equation, for analytically untractable potentials, in momentum space. This idea opens up the possibility of expanding the number of potentials that we present in a quantum mechanics course by providing us with a fairly simple means of computationally solving the Schrödinger equation for a class of potentials that have no analytically solution. In the following chapter we present the basic formulism for this approach and several different implementations of it.

3. SCHRÖDINGER EQUATION IN MOMENTUM SPACE

> I don't like it, and I'm sorry I ever had anything to do with it.
>
> (Erwin Schrödinger)

We begin of course, as most, if not all, introductory courses in quantum mechanics [60] [61] do, with the one-dimensional (1D) time-independent Schrödinger equation written in real space representation,

$$-\frac{\hbar^2}{2m}\frac{d^2}{dx^2}\psi_\alpha(x) + V(x)\psi_\alpha(x) = E_\alpha\psi_\alpha(x). \tag{3.1}$$

This equation provides the eigenvalues, E_α, and eigenfunctions, $\psi_\alpha(x)$, for a non-relativistic particle of mass m in the presence of an external potential, $V(x)$, and for most students this is their first introduction to the Sturm-Liouville problem [62] [63] as well as their first major exposure the the fundamental ideas of quantization [60]. As with most differential and partial differential equations the number of exactly solvable models is small and depends on the form of the potential $V(x)$. The analytically solvable potentials in one dimension, and therefore the potentials introduced in courses, are the quantum well, the step, the harmonic oscillator, the delta function, or some combination of the above [60]. In higher dimensions, the number of analytically solvable potentials is even smaller.

One approach to solving Eq. (3.1) is by using the Wentzel-Kramers-Brillouin (WKB) approximation [61] which provides a means for determining the quantized energy levels through a semi-classical picture. A second means for solving Eq. (3.1) is through discretization to obtain a matrix equation

$$\sum_{j=-N}^{N}\left[-\frac{\hbar^2}{2m}D_{ij} + V(x_i)\delta_{ij}\right]\psi_\alpha(x_j) = \sum_{j=-N}^{N} H_{ij}\psi_\alpha(x_j) = E_\alpha\psi_\alpha(x_i) \tag{3.2}$$

where $x_j = j\Delta x, \Delta x$ is the spacing between adjacent points along the x-axis, N is the total number of discrete points, and $N\Delta x = X_c$ is the spatial cutoff which is chosen such that $X_c \gg a$ where a is the characteristic length scale associated with the potential $V(x)$. The matrix D_{ij} is a discrete second derivative which is of tridiagonal form with entries $D_{ij} = [\delta_{i,j-1} - 2\delta_{ij} + \delta_{i,j+1}]/(\Delta x)^2$. As $X_c \to \infty$ and $\Delta x \to 0$ the eigenvalues and eigenvectors of H_{ij} approach the continuum result. The problems associated with this approach are due to the fact that the factor $(\Delta x)^{-2}$ is diverging and the error in the D_{ij} matrix at the $\pm X_c$ end points lead to instability in the results. One way around this problem is to employ the Numerov method to obtain the spectrum and eigenfunctions [64] [65]. And one other solution is to use an eigenfunction expansion [66] in which we use the method of undetermined coefficients on the resulting coefficients matrix.

In the following sections we will provide a method for solving Eq. (3.1) for a class of potentials that do not lend themselves to an analytical solution, and bypasses the stability and convergence issues that we have previously discussed.

3.1 One Dimensional Case

> For the wise man looks into space and he knows there is no limited dimensions. (Laozi)

We begin by taking the Fourier transform of the 1D Schrödinger equation, Eq. (3.1),

$$\epsilon_p \psi_\alpha(p) + \int_{-\infty}^{\infty} \frac{dp'}{2\pi\hbar} V(p-p')\psi_\alpha(p') = E_\alpha \psi_\alpha(p), \tag{3.3}$$

where $\psi_\alpha(p)$ is the momentum-space wavefunction, $\epsilon_{\mathbf{p}} = p^2/2m$ is the non-relativistic kinetic energy of the particle, and $V(p-p')$ is the Fourier transform of the potential $V(x)$. Equation (3.3) has been used to study the the scattering problem [67] [68] and the bound state in a δ-function potential [69]. It is Eq. (3.3) which provides the restriction on the class of potentials we are able to use in this method. In order for us to be able solve Eq. (3.3) the Fourier transform of $V(x)$ must be well defined. This of course means that in principle we will be unable to use this method to solve the problem, for all energies and eigenstates, for well known, and analytically solvable, potentials such as the infinite quantum well and harmonic oscillator where the Fourier transform does not exist. Although, if we are interested in only the behavior of the low lying eigenstates we will be able to use this method. To explore Eq. (3.3) numerically we start by converting it into a unitless equation where a_0 is the unit of length, $\hbar/a_0$ is the momentum scale, and $E_0 = \hbar^2/2ma_0^2$ is the unit of energy. Using these dimensionless quantities Eq. (3.3) becomes

$$\sum_n \left[u_n^2 \delta_{mn} + \widetilde{V}_{mn}\right] \psi_\alpha(u_n) = \widetilde{E}_\alpha \psi_\alpha(u_m) \tag{3.4}$$

where $u_n = n\Delta u = n\Delta p a_0/\hbar$ is the dimensionless momentum, Δu is the momentum points spacing, $\widetilde{E}_\alpha = E_\alpha/E_0$ is the dimensionless eigenvalue, and $\widetilde{V}_{mn} = V(p_m - p_n)\Delta u/(2\pi E_0 a_0)$ is the dimensionless potential containing the measure $\Delta u/(2\pi)$. With this discretization we have taken the integral Schrödinger equation, Eq. (3.3), and transformed it into a matrix equation, Eq. (3.4).

The size of our Hamiltonian matrix H_{mn} is determined by the ultraviolet cutoff $U_c = P_c a_0/\hbar$, where P_c is the upper limit of integration in Eq. (3.3), and the spacing Δu. It is important to understand that $2\pi a_0/\Delta u$ ($2\pi a_0/U_c$) determine the upper (lower) limit on the real-space bound-state wavefunction which means that they must be chosen carefully for a given potential in order to obtain results that are valid in the continuum limit, $U_c \to \infty$ and $\Delta u \to 0$. If the external potential $V(x)$ is even, the Hamiltonian H_{mn} is real. Therefore, the eigenfunctions $\psi_\alpha(p)$ have a definite parity and are real [61]. In this case it is sufficient to restrict ourselves to positive momenta $m, n \geq 0$.

The first potential we will consider is a quantum well with depth, V_0, and width, a, centered at the origin, $V(x) = -V_0\theta(a - 2|x|) = V(-x)$ where $\theta(x)$ is the Heavy-side function [62] [63]. For this potential the Hamiltonian matrix is given by

$$H_{mn} = u_n^2 \delta_{mn} - \frac{\Delta u}{2\pi} \frac{2aV_0}{a_0 E_0} \frac{\sin[(u_n - u_m)a/a_0]}{[(u_n - u_m)a/a_0]} = H_{nm}. \tag{3.5}$$

When $a \to 0$ and $V_0 \to \infty$ with $aV_0 = \lambda_1$, where λ_1 is a constant, Eq. (3.5) takes the form of the Hamiltonian for a one dimensional δ-function. For this case we know that there should be one exponentially bound state $\psi_b(x) = \sqrt{\kappa} \exp(-\kappa|x|)$ with size $\kappa^{-1} = \hbar^2/m\lambda_1$ and energy $E_b = -m\lambda_1^2/2\hbar^2$ for $\lambda_1 < 0$ [60] [61].

We obtained the eigenvalues and eigenvectors of the matrix H_{mn} for $0 \leq |\lambda_1/E_0 a_0| \leq 1$ with two different values of $\Delta u = \{0.01, 0.005\}$ and two different cutoffs $U_c = \{10, 20\}$. The corresponding matrix dimensions $N = U_c/\Delta u$ in these four cases varies from 1000×1000 to 4000×4000. We found that the energy spectrum has one negative eigenvalue and the positive eigenvalues form a quadratic band representative of a free particle. (The positive energy stares are not accessible via the Numerov method [64].) Figure 3.1 shows that the bound state energy $E_b(\lambda_1)$ matches the analytical result.

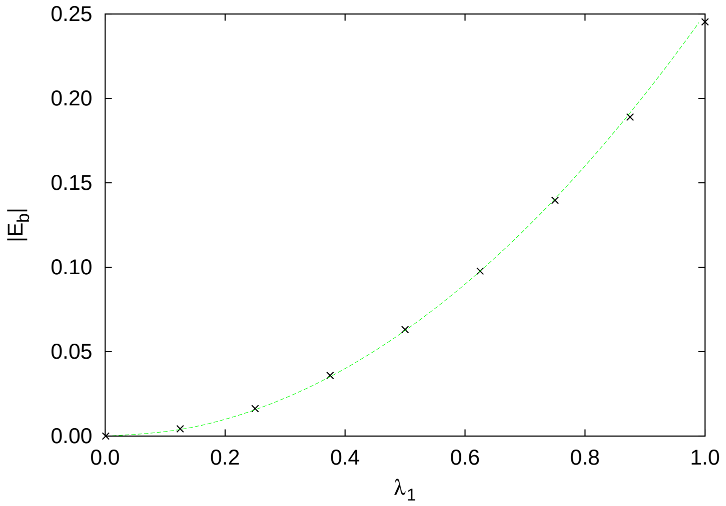

Fig. 3.1.: Dependence of the magnitude of the bound state energy $|E_b|$ obtained from the matrix H_{mn}, Eq. (3.5), on the strength λ_1 of the one-dimensional attractive δ-function potential. The energy is in units of $E_0 = \hbar^2/2ma_0^2$ and λ_1 is in units of $E_0 a_0$. The numerical results (cross) are in excellent agreement with the analytical result [60] [61] $|E_b|/E_0 = \lambda_1^2/4(E_0 a_0)^2$ (dashed line).

Figure 3.2 shows a typical momentum space wavefunction for the bound state $\psi_b(p)$ and a state with positive energy.

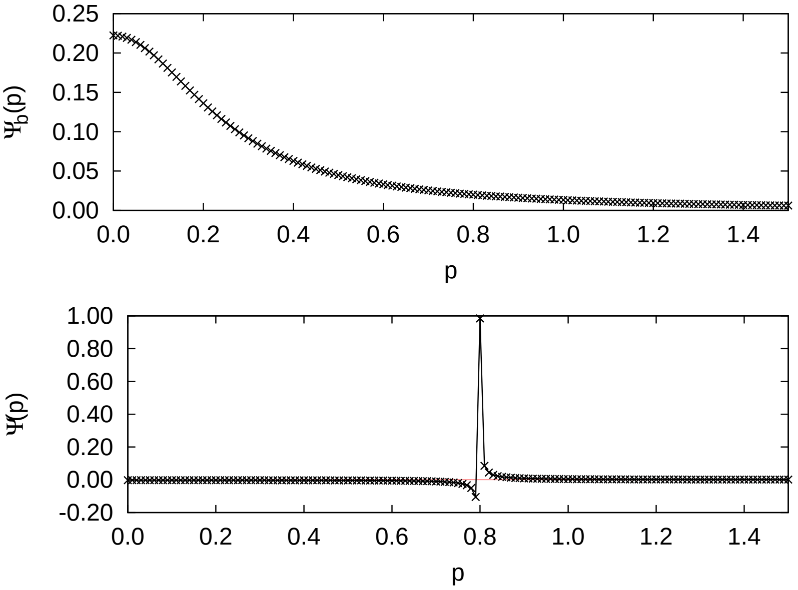

Fig. 3.2.: Typical momentum space wavefunctions for the bound state (top curve) and a positive energy state (bottom curve) for $\lambda_1/E_0a_0 = 0.5$. The momentum p is in units of $a_0/\hbar$ and the wavefunction is in units of $\sqrt{a_0}$. The width of the bound state wavefunction $\psi_b(p)$ is given by $\hbar\kappa = m\lambda_1/\hbar$. The positive energy wavefunction is, as expected, sharply localized in momentum space.

As expected, we see that the bound state wavefunction is sharply peaked near a single momentum value. We check that the bound state results are independent of U_c and Δu. (The smallest momentum cutoff is chosen such that the contribution from momenta $p > P_c = U_c\hbar/a_0$ to the bound state wavefunction is negligible.) Increasing U_c affects the eigenvalues and eigenvectors near the highest energy $E_c/E_0 = U_c^2$, whereas reducing Δu sharpens the momentum space eigenfunctions at positive energies. Thus, this numerical approach is particularly suited to study bound states, and may not handle the unbound positive energy states equally well.

Next, we consider the problem of a deep quantum well $V_0/E_a \gg 1$. We diagonalize the matrix H_{mn}, Eq. (3.4), with $V_0/E_0 = 1, U_c = 300, \Delta u = 0.1$ and $a/a_0 = \{20, 25\}$.

Figure 3.3 shows that the numerically obtained spectrum of the bound state energies measured from the bottom of the quantum well is quadratic, $E_n = n^2\pi^2\eta$. This dependence is expected because for an infinite quantum well of size a the eigenvalues are given by $E_n = n^2\pi^2 E_a$. The prefactor $\eta(U_c, \Delta u, V_0) \neq E_a$, and a systematic exploration with increasing U_c and a, are decreasing Δu shows that this discrepancy is due only to discretization.

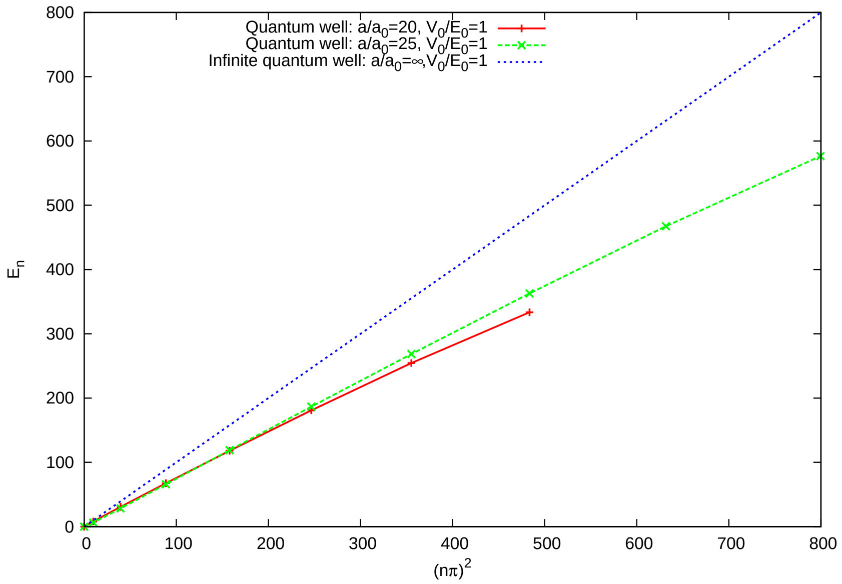

Fig. 3.3.: Energies E_n of bound states in a deep quantum well $V_0/E_a \gg 1$ obtained from Eq. (3.4). The bound-state energies E_n are positive because they are measured from the bottom of the well. The energies are in units $E_a = \hbar^2/2ma^2 = E_0(a_0/a)^2$ instead of the customary unit E_0. The solid and the dashed lines represent results for $V_0/E_a = (a/a_0)^2 = 400$ and 625 respectively. The dotted line shows the analytical result for an infinite quantum well of width $a, E_n = (n\pi)^2 E_a$.

We next consider the case of an attractive Gaussian potential $V_1(x) = -V_0 \exp(-x^2/2a^2)$. In this case a closed form solution for the eigenvalues and eigenfunctions is unknown. The dimensionless Hamiltonian becomes

$$H^{(1)}_{mn} = u_n^2 \delta_{mn} - \frac{\Delta u}{\sqrt{2\pi}} \frac{2V_0 a}{E_0 a_0} \exp\left[\frac{(u_m - u_n)^2 a^2}{2a_0^2}\right] = H^{(1)}_{nm}. \tag{3.6}$$

Figure 3.4 shows the a-dependence of the magnitude of the ground state energy $E_b < 0$ obtained by using $V_0/E_0 = 1, \Delta u = 0.01$, and $U_c = 30$. The inset shows the ground state momentum space wavefunction $\psi_G(p)$ for $a/a_0 = \{0.1, 0.5\}$. As a/a_0 increases, the effective value of V_0/E_a increases. Thus, the ground state becomes more localized in real space, and the spread of the wavefunction in momentum space increases.

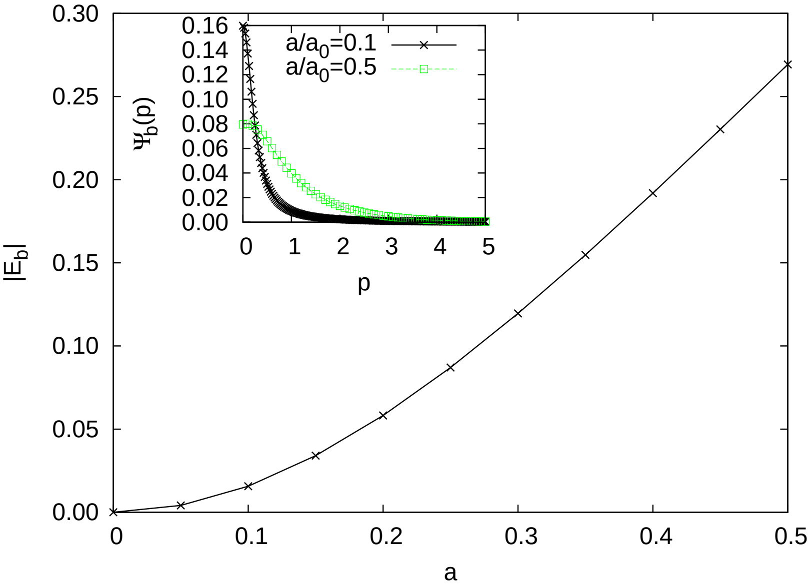

Fig. 3.4.: Magnitude of the ground state energy $|E_b|$ for a Gaussian potential $V(x) = -V_0 \exp(-x^2/2a^2)$ as a function of a for a fixed depth of $V_0/E_0 = 1$. The energies are in units of E_0, the length is in units of a_0, and the momentum in the inset is in units of $\hbar/a_0$. The inset shows the ground state momentum space wavefunction in units of $\sqrt{a_0}$. As a increases, the ground state wavefunction becomes increasingly localized in real space, and is reflected in the broadening of the momentum space wavefunction.

We emphasize that the bound state eigenvalues and eigenfunctions obtained from the diagonalization of the discrete matrix H_{mn} should be essentially independent of the cutoff $U_c \gg 1$ and the spacing $\Delta u \ll 1$, to verify that they are valid in the continuum limit $U_c \to \infty, \Delta u \to 0$. Note that even in the limit $\Delta u \to 0$, a finite momentum cutoff P_c leads to a real space potential that is not the same as the original one:

$$V_c(x) = \int_{-P_c}^{P_c} \frac{dp}{2\pi\hbar} V(p) e^{ipx/\hbar} \neq V(x). \tag{3.7}$$

Thus the discretization parameters need to be so chosen that the difference between $V_c(x)$ and $V(x)$ is negligible. Two typical indicators that the continuum limit has not been reached are that some eigenvalues are lower than the depth of the potential well, $E_\alpha < -V_0$, and the ground state momentum space wavefunction is linear, instead of quadratic, near $p = 0$. In one dimension we can choose the ground state wavefunction $\psi_G(x)$ to be positive [60] [61], so that, for an even potential the momentum space wavefunction is parabolic at the origin, $\psi_G(p) - \psi_G(0) \propto -p^2$. Therefore, a linearly varying $\psi_G(p)$ is a clear indication that the bound state eigenvalues and eigenfunctions do not represent the continuum results. In the following we show that the verification of the continuum limit is more subtle in two dimensions and requires careful treatment.

3.2 Higher Dimensional Case

> In order to more fully understand this reality, we must take into account other dimensions of a broader reality. (John Archibald Wheeler)

For a particle in two or more dimensions, a naive discretization of the integral Schrödinger equation in Cartesian co-ordinates implies that the Hamiltonian matrix has a size $\sim N^D \times N^D$ where $N = U_c/\Delta u$ is the number of discrete points along a single axis and D is the dimension. Thus, even in two dimensions, this results in $10^6 \times 10^6$ or larger matrices that are impossible to treat numerically. For a central potential in two dimensions, the rotational invariance of the Hamiltonian implies that the angular momentum is a good quantum number and the eigenfunctions can be labeled by an integer angular momentum label $l, \psi_{\alpha l}(\mathbf{p}) = \psi_{\alpha l}(p)\exp(il\theta_p)$, where

$\mathbf{p} = (p, \theta_p)$ is the 2D momentum [60] [61] [67]. The Schrödinger equation for a given value of l becomes [65]

$$\frac{p^2}{2m}\psi_{\alpha l}(p) + \int \frac{p' dp' d\theta_{p'}}{(2\pi\hbar)^2} V(p, p'; \theta_p - \theta_{p'}) e^{-il(\theta_p - \theta_{p'})} \psi_{\alpha l}(p') = E_{\alpha l}\psi_{\alpha l}(p) \tag{3.8}$$

where $V(p, p'; \theta_p - \theta_{p'}) = V(|\mathbf{p} - \mathbf{p}'|)$ is the momentum space potential and depends only on the relative angle between $\mathbf{p}$ and $\mathbf{p}$' due to the central nature of the potential. The corresponding dimensionless Hamiltonian matrix becomes $H_{mn}(l) = u_n^2\delta_{mn} + \tilde{V}_{mn}(l)$, where the angular averaged potential matrix is given by

$$\tilde{V}_{mn}(l) = \frac{u_n \Delta u}{2\pi E_0 a_0^2} \int_0^{2\pi} \frac{d\theta}{2\pi} V(u_m, u_n; -\theta) e^{il\theta}. \tag{3.9}$$

Here, $0 \leq u_n \leq U_c$ denotes the magnitude of the dimensionless momentum and matrix $H_{mn}(l)$ has size $\sim N \times N$. Due to the prefactor $u_n \Delta u$ from the 2D area element in polar coordinates, the Hamiltonian obeys $H_{nm}(l) = (u_m/u_n)H^*_{mn}(l)$. Thus, the discretized Hamiltonian matrix is not Hermitian with respect to the transpose of the matrix plus complex conjugation. It is Hermitian with respect to the inner product defined via the 2D measure. We focus on the $l = 0$ case because for a time-reversal invariant Hamiltonian, the ground state has zero angular momentum [61] [67].

As an illustration, we consider an attractive δ-function in two dimensions, $V(\mathbf{r}) = -\lambda_2\delta^2(\mathbf{r})$. Although a trivial extension of the 1D problem, it is rarely discussed [70] in introductory courses, perhaps because the bound-state real-space wavefunction is logarithmically divergent [71] in the vicinity of the δ-function. The bound-state energy $E_b(\lambda_2, U_c)$ depends on the ultraviolet cutoff U_c and has a non-analytic dependence on the strength of the potential, $E_b/E_0 = -U_c^2 \exp(-4\pi E_0 a_0^2/\lambda_2)$ [70] [72]. The momentum space Schrödinger equation in this case is analytically tractable and provides a good test [72]. Because the Fourier transform of this potential is a constant, the Hamiltonian matrix becomes

$$H_{mn}(l) = u_n^2 \delta mn - \frac{u_n \Delta u}{2\pi} \frac{\lambda_2}{E_0 a_0^2} \delta_{l0} = \frac{u_n}{u_m} H_{nm}(l). \tag{3.10}$$

The δ-function potential affects only the $l = 0$ sector of the Hilbert space because wavefunctions with $l \neq 0$ vanish at the position of the δ-function due to the centripetal barrier. We verify that there is a single bound state for an attractive potential ($\lambda_2 > 0$) and none for a repulsive potential ($\lambda_2 < 0$). Figure 3.5 shows the magnitude of the bound state energy $E_b(\lambda_2)$ as a function of $4\pi E_0 a_0^2/\lambda_2$ for $2 \leq \lambda_2/E_0 a_0^2 \leq 20$. We use $\Delta u = 0.01$ and two ultraviolet cutoffs $U_c = \{10, 20\}$.

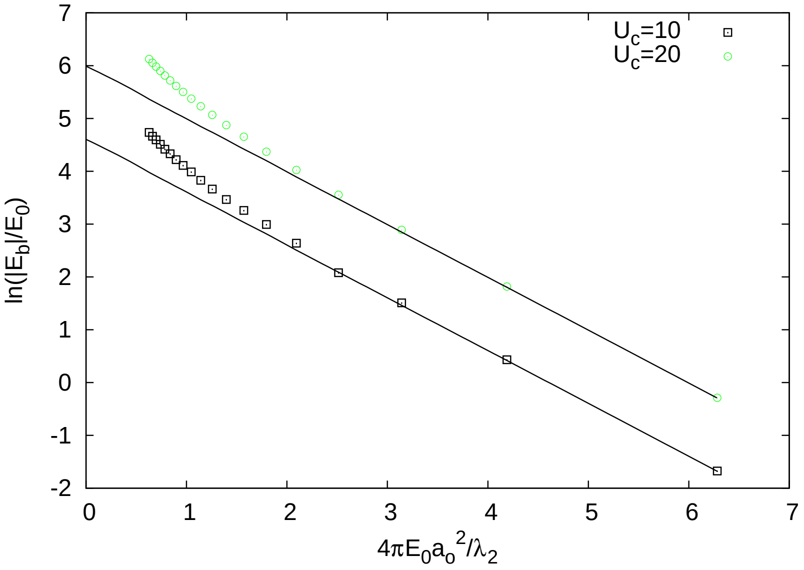

Fig. 3.5.: Dependence of $|E_b|$ on the strength λ_2 of the attractive two-dimensional δ-function potential for ultraviolet momentum cutoffs $U_c = 10$ (squares) and $U_c = 20$ (circles). The energy is in units of E_0 and λ_2 is in units of $E_0 a_0^2$; $\Delta u = 0.01$ and $2 \leq \lambda_2/E_0 a_0^2 \leq 20$. The solid lines represent the analytical result, $\ln(|E_b|/E_0) = -4\pi E_0 a_0^2 + \ln(U_c^2)$ for $U_c = 10$ (bottom curve) and $U_c = 20$ (top curve). The corresponding y-intercepts are $\ln(10^2) \approx 4.6$ and $\ln(20^2) \approx 6$. The discrepancy between the numerical and analytical results for large $\lambda_2/E_0 a_0^2 \sim U_c$ is decreased when Δu is reduced.

At large values of $\lambda_2/E_0 a_0^2 \sim U_c$, the numerical results deviate from the expected straight line behavior due to discretization. This deviation is systematically suppressed by reduction of Δu. Note that for an attractive δ-potential in both one and two dimensions the bound state wavefunction has the same functional form, $\psi_b(p) \propto 1/(p^2 + \hbar^2\kappa^2)$. However, because the bound-state energy $E_{b2} \propto \exp(-1/\lambda_2)$ in two dimensions [70], in contrast to the bound-state energy $E_{b1} \propto \lambda_1^2$ in one dimension [60] [61], the size of the wavefunction in momentum space in two dimensions is much smaller than that in one dimension, $\hbar\kappa_2 = \sqrt{2|E_{b2}|} \ll \hbar\kappa_1 = \sqrt{2m|E_{b1}|}$. We emphasize that the dependence of E_b on the cutoff U_c is a peculiar property of the weakly bound state in the 2D δ-function potential and arises due to the absence of an energy scale in a problem characterized by $(\hbar, m, \lambda_2)$. For a general potential, including the attractive Coulomb interaction $V(r) = -e^2/r$, we numerically obtain multiple bound states with energies that are independent of the cutoff [73].

For a central potential it is straightforward to extend this method to higher dimensions. In D-dimensions we represent a vector using hyperspherical coordinates, $\mathbf{p} = (p, \phi, \theta_1, \theta_2, \ldots, \theta_{D-2}$ where $\phi \in [0, 2\pi]$ and $\theta_i \in [0, \pi]$ [74]. The Hamiltonian is then block diagonalized into blocks with different angular momenta. The effective potential in the block (l, l_z) is obtained by performing an integral over angular variables, similar to that in Eq. (3.9). It is not always possible to analytically carry out this integration. The resulting Hamiltonian matrix satisfies $H_{mn}(l, l_z) = (u_m/u_n)^{D-1} H^*_{nm}(l, l_z)$, and the resulting eigenvectors $\psi_\alpha(u_k)$ are orthogonal with respect to the D-dimensional inner product

$$\langle \psi_\alpha | \psi_\beta \rangle = \frac{\Delta u}{2\pi} \sum_{k=0}^{N} \psi^*_\alpha(u_k) \psi_\beta(u_k) u_k^{D-1} = 0 \quad (\alpha \neq \beta). \tag{3.11}$$

The exploration of the Hamiltonian matrix $H_{mn}(l, l_z)$ in $D \geq 2$ dimensions emphasizes two important points. First, by explicit construction, it generates a set of matrices, each element of which appears non-Hermitian and still has a purely real eigenvalue spectrum. Second, it explicitly demonstrates that the notion of orthonormality and Hermiticity are intimately connected to the inner-product used to construct the Hilbert space of wavefunctions [60]. In Appendix B we show two different means of obtaining these results that would be more accessible to students with little to no programming experience.

3.3 Conclusions

> I am not so much convinced of our ignorance by those phenomena that do exist and of whom we ignore the reason, as by those that do not exist and for whom we find a reason. (Fontenelle)

In this chapter we have presented an approach to solving the Schrodinger equation by properly discretizing the Hamiltonian matrix in momentum space [65]. As we have discussed, this approach does not suffer from instabilities [64] that are introduced by discretizing the real-space equation which is do to the fact that in momentum space, the differential operator is diagonal and for most potentials of interest, the matrix elements for scattering from p to p' decay for large $|\mathbf{p} - \mathbf{p}'|$.

This method of course can not be used in all cases. The restriction is that the Fourier transform of the potential must be well-defined. This restriction seems to rule out the use of this method to solve a few well known potentials such as the harmonic oscillator and the infinite quantum well. However, as was discussed in the this chapter, since we are most usually interested in the first few lowest energy states this approach can still be used for a sufficiently deep well.

In addition to detailing the procedure for using the momentum space Hamiltonian matrix to solve these equations we have also provided practical demonstrations on how to use this procedure in conjunction with a couple of different numerical programs in Appendix B. Although this approach is very easy to implement in existing software packages such as *Mathematica*, it also affords an excellent opportunity to introduce students to programming in general. To further this goal we have developed a program in which users are able to write their own modules which will then allow them to choose which potential to solve for and at the same time introduce them to mainstream programming.

In the following chapter we will develop the theory and numerical procedure for solving the problem of finding bound states using real-space lattice models.

4. REAL SPACE LATTICE MODELS

> I seem to have been only like a boy playing on the seashore, and diverting myself in now and then finding a smoother pebble or a prettier shell than ordinary, whilst the great ocean of truth lay all undiscovered before me.
>
> (Sir Isaac Newton)

In the previous chapters we have shown how to apply the mean-field approximation to the problem of exciton condensation in double quantum wells and graphene and explored the dilute exciton limit. The common theme in these chapters was that all of these calculations were performed in momentum space. In this chapter we will develop a complementary approach to both of these problems by modeling them in real space.

4.1 Exciton Condensation

> There are no physicists in the hottest parts of hell, because the existence of a 'hottest part' implies a temperature difference, and any marginally competent physicist would immediately use this to run a heat engine and make some other part of hell comfortably cool. This is obviously impossible.
>
> (Richard Davisson)

By using the mean-field approximation in real space we trade ease of calculation for an increase in information. In momentum space, we derived the equations, Eqs. (2.40)-(2.42), that we must iterate to obtain self-consistent values for $\xi(\mathbf{k})$, $\Delta(\mathbf{k})$ and $E(\mathbf{k})$ while in real space we need to calculate each element of the density matrix per iteration. As usual we begin with the non-interacting components of our tight binding Hamiltonian for a system consisting of two graphene sheets, one stacked on top of the other separated by a distance d,

$$\begin{aligned} H_0 = -t_T \sum_{T_i} \sum_{<>_{T_i}} \left[c^\dagger_{T_i} c_{<>_{T_i}} + c^\dagger_{<>_{T_i}} c_{T_i} \right] - \mu_T \sum_{T_i} c^\dagger_{T_i} c_{T_i} \\ - t_B \sum_{B_i} \sum_{<>_{B_i}} \left[c^\dagger_{B_i} c_{<>_{B_i}} + c^\dagger_{<>_{B_i}} c_{B_i} \right] - \mu_B \sum_{B_i} c^\dagger_{B_i} c_{B_i} \end{aligned} \tag{4.1}$$

where the first and third terms represent the non-interacting Hamiltonian that we have seen previously and μ_T and μ_B represent the chemical potentials in the top and bottom layer respectively. The label $T(B)$ in Eq. (4.1) stand for the top (bottom) layer where the index i ranges over all lattice points within a layer. Next we have the interaction terms

$$H_{int} = \frac{1}{2} \sum_{T_i,T_j} V_{T_i,T_j} \rho_{T,i} \rho_{T,j} + \frac{1}{2} \sum_{B_i,B_j} V_{B_i,B_j} \rho_{B,i} \rho_{B,j} + \sum_{T_i,B_j} V_{T_i,B_j} \rho_{T,i} \rho_{B,j} \tag{4.2}$$

where V_{TT} (V_{BB}) are the top (bottom) intra-plane interactions, V_{TB} is the inter-plane interaction, and ρ_T (ρ_B) are the on site density for the top (bottom) layers. Once again to proceed, we need to perform the Hartree-Fock approximation just as we did in the previous chapters. By doing so we find the interaction components to be

$$\begin{aligned} H^{MF}_{int} = \sum_{T_i,T_j,B_j} \left[\left(V_{T_i,T_j} \langle c^\dagger_{T_j} c_{T_j} \rangle + V_{T_i,B_j} \langle c^\dagger_{B_j} c_{B_j} \rangle \right) c^\dagger_{T_i} c_{T_i} - V_{T_i,T_j} \langle c^\dagger_{T_i} c_{T_j} \rangle c^\dagger_{T_j} c_{T_i} \right] \\ + \sum_{B_i,B_j,T_j} \left[\left(V_{B_i,B_j} \langle c^\dagger_{B_j} c_{B_j} \rangle + V_{T_i,B_j} \langle c^\dagger_{T_j} c_{T_j} \rangle \right) c^\dagger_{B_i} c_{B_i} - V_{B_i,B_j} \langle c^\dagger_{B_i} c_{B_j} \rangle c^\dagger_{B_j} c_{B_i} \right] \\ + \sum_{T_i B_j} V_{T_i,B_j} \left[\langle c^\dagger_{T_i} c_{B_j} \rangle c^\dagger_{B_j} c_{T_i} + \langle c^\dagger_{B_j} c_{T_i} \rangle c^\dagger_{T_i} c_{B_j} \right]. \end{aligned} \tag{4.3}$$

In Eq. (4.3) the density matrix element $\rho_{\alpha,\beta} = \langle c^\dagger_\alpha c_\beta \rangle$ is obtained by the change of basis

$$\rho_{i,j} = V_{j,i'} O_{i,i'} \left(V^\dagger \right)_{i',i} \tag{4.4}$$

where V is a matrix whose columns are the eigenvectors of our mean-field Hamiltonian matrix, H^{MF}, and the occupation matrix, $O_{i,i'}$ is given by

$$O_{i,i'} = \frac{1}{e^{k_b E_i} + 1} \delta_{i,i'} \tag{4.5}$$

where E_i is the i^{th} eigenvalue.

The procedure is to use the non-interacting Hamiltonian to create an initial density matrix, $\rho_{i,j}(0)$, and from this initial matrix we obtain the starting electron density, $n_e(0) = \frac{1}{N} \sum_i \rho_{i,i}(0)$ where i ranges over all lattice points within the top layer, and starting hole density, $n_h(0) = \frac{1}{N} \sum_j \rho_{j,j}(0)$ where j ranges over all lattice points within the bottom layer with both layers containing a total of N lattice points. From here we include the effect of interaction by adding to the non-interacting Hamiltonian the appropriate elements from the density matrix according to Eq. (4.3). Once we have constructed our new Hamiltonian matrix, then find its corresponding density matrix and determine whether the electron and hole densities are greater or less than the initial densities. We use this procedure to tune the chemical potentials to return them to their initial values. This procedure is performed until a convergence criterion is met such as the difference between the previous and current eigenvalues and density matrices is less than a given tolerance. In Fig. 4.1 we see a contour representation of an initial Hamiltonian matrix for a system of two graphene sheets.

The matrix is divided into four major quadrants and each quadrant is itself divided into four more quadrants. The major divisions divide the matrix into top-top (TT), top-bottom (TB), bottom-top (BT), and bottom-bottom (BB) areas. In the TT and BB sections we have the chemical potentials for the top, $\mu_T = 0.50$, and bottom, $\mu_B = -0.50$, layers along the diagonal and the off-diagonal elements represent the hopping from one lattice site to another within a layer with an amplitude of $t = -1$. The TB and BT quadrants represent the interactions that are responsible for creating the excitons. In order to break the symmetry between the top and bottom layers we manually input a tunneling amplitude between a lattice site in the top layer and its nearest neighbor in the bottom layer of $t_\perp = 0.1$. Within each of these quadrants the

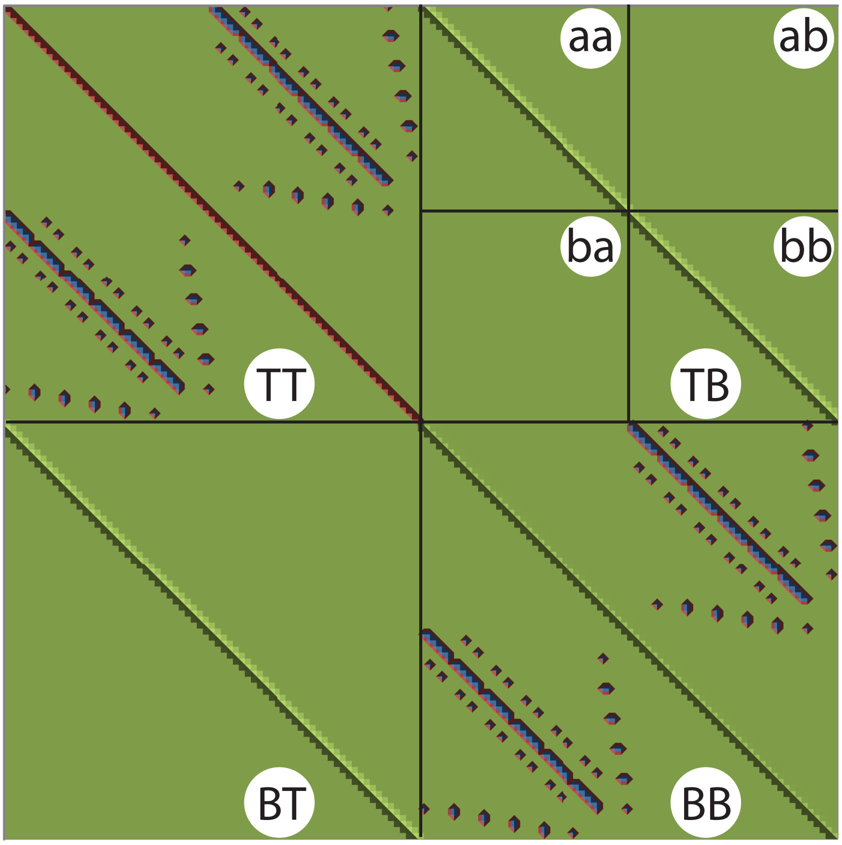

Fig. 4.1.: Hamiltonian matrix for a double layer system of graphene. The matrix is divided into quadrants where the label T stands for the top layer and B the bottom layer. Each quadrant is then subdivided into four sections where the label “a” stands for the A sub-lattice and the label “b” stands for the B sub-lattice in each layer of graphene. The TT and BB quadrants represent the non-interacting Hamiltonians for the top and bottom layers respectively with a hopping amplitude $t = -1$, and with the inclusion of the chemical potentials, $\mu_T = 0.50$, for the top layer on the diagonal in the TT quadrant and, $\mu_B = -0.50$, for the bottom layer on the diagonal in the BB quadrant. The TB and BT quadrants represent the exciton symmetry breaking elements. Since there is tunneling only between the sites that are directly above one another the elements within these quadrants are non-zero only on the diagonal with a tunneling amplitude $t_\perp = 0.1$.

further subdivisions are created by having the lattice points within a layer labeled such that all the A sub-lattice points are listed first followed by all the B sub-lattice points.

In Fig. 4.2(a) a contour plot of the density matrix, $\rho_{ij}(0)$, is shown which is calculated from the initial non-interacting Hamiltonian shown in Fig. 4.1.

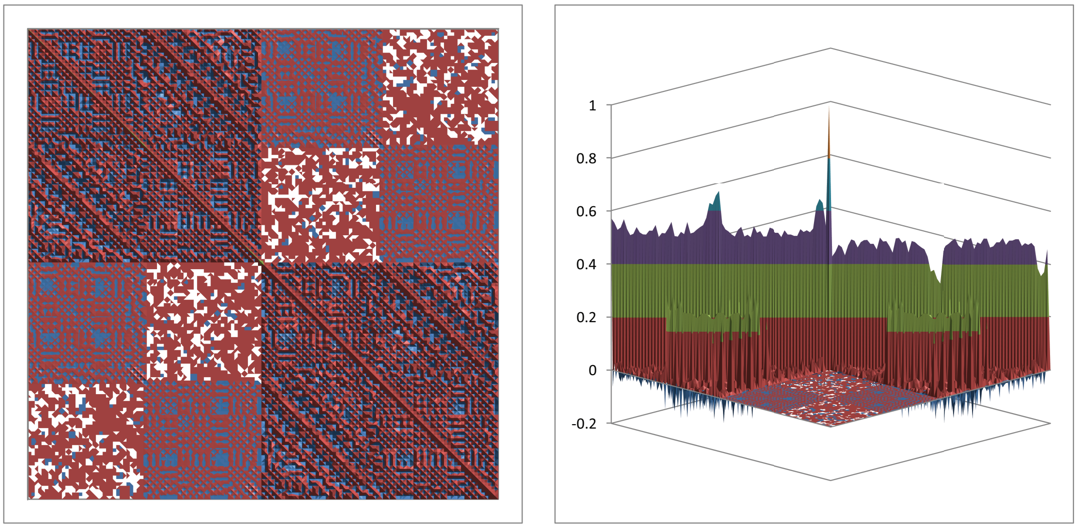

(a)

(b)

Fig. 4.2.: (a) This image shows the density matrix with zero interaction and finite inter-plane tunneling. The effect of the tunneling can be seen in the upper-right and lower-left quadrants. For zero tunneling these quadrants would be identically zero. The on-site exciton densities scale proportionally to the inter-plane tunneling amplitude as expected. (b) This image shows the profile of the density matrix. We are able to see that the diagonal of the matrix consists of two fairly constant values. The first half correspond to the on site electron densities and the second half corresponds to the on site hole densities. The major features are do to edge effects which are exaggerate by the small size of the corresponding Hamiltonian matrix. For these figures the top layer chemical potential $\mu_T = 0.5$, bottom layer chemical potential $\mu_B = -0.5$, intra-plane hopping $t = -1$, and inter-plane tunneling $t_\perp = 0.1$.

For zero inter-layer tunneling the upper-right and lower-left quadrants would be identically zero. We have also verified that the on-site exciton densities scale proportionally with the tunneling amplitude. In Fig. 4.2(b) is a plot of the same density matrix seen in profile. What we see is a relative constant density for both the electrons in the top layer and electrons in the bottom layer. The top layer electron densities are the higher values and the bottom layer electron densities are the lower values.

4.2 Bound States

> A new scientific truth does not triumph by convincing its opponents and making them see the light, but rather because its opponents eventually die, and a new generation grows up that is familiar with it.
>
> (Max Planck)

We begin with a tight binding Hamiltonian on an infinite one-dimensional (1D) lattice given by

$$\hat{H} = \sum_i \left[-t \left(c_i^\dagger c_{i+1} + c_{i+1}^\dagger c_i \right) + V_i c_i^\dagger c_i \right], \tag{4.6}$$

where $c_i^\dagger (c_i)$ are the creation and (annihilation) operators at site i and V_i is the on site interaction. Starting with an energy eigenstate $|\psi^n\rangle = \sum_j f_j^n |j\rangle$ by definition we need to solve the following equation

$$\hat{H} \sum_j f_j^n |j\rangle = E^n \sum_j f_j^n |j\rangle, \tag{4.7}$$

where E^n is the energy eigenvalue for state $|\psi^n\rangle$ and f_j^n is the amplitude of the eigenvector n^{th} at position j. Again, by definition we have $|j\rangle = c_j^\dagger |0\rangle$ which gives

$$\sum_{i,j} f_j^n \left[-t \left(c_i^\dagger c_{i+1} + c_{i+1}^\dagger c_i \right) + V_i c_i^\dagger c_i \right] c_j^\dagger |0\rangle = E^n \sum_j f_j^n c_j^\dagger |0\rangle. \tag{4.8}$$

By using the commutation relation $c_i c_j^\dagger = \zeta c_j^\dagger c_i + \delta_{i,j}$ where $\zeta = -1$ for fermions and $\zeta = 1$ for bosons we find $c_i^\dagger c_{i+1} c_j^\dagger|0\rangle = \delta_{i+1,j} c_i^\dagger|0\rangle$, $c_{i+1}^\dagger c_i c_j^\dagger|0\rangle = \delta_{i,j} c_{i+1}^\dagger|0\rangle$, and $c_i^\dagger c_i c_j^\dagger|0\rangle = \delta_{i,j} c_i^\dagger|0\rangle$ which when we substitute into Eq. (4.8) gives

$$\sum_{i,j} f_j^n \left[-t\left(\delta_{i+1,j} c_i^\dagger + \delta_{i,j} c_{i+1}^\dagger\right) + V_i \delta_{i,j} c_i^\dagger\right]|0\rangle = E^n \sum_j f_j^\alpha c_j^\dagger|0\rangle. \tag{4.9}$$

By shifting the index of the Kronecker δ-function and creation operator in the first term we have

$$\sum_j \left[-t\left(f_j^n|j-1\rangle + f_j^n|j+1\rangle\right) + f_j^n V_j|j\rangle\right] = E^n \sum_j f_j^n|j\rangle. \tag{4.10}$$

Once again we shift indices to arrive at

$$\sum_j \left[-t\left(f_{j+1}^n + f_{j-1}^n\right) + (V_j - E^n) f_j^n\right]|j\rangle = 0. \tag{4.11}$$

Because the eigenstates localized at different sites are orthogonal, this equation must be true for every j

$$-t\left(f_{j+1}^n + f_{j-1}^n\right) + (V_j - E^n) f_j^n = 0. \tag{4.12}$$

By adding and subtracting appropriately we arrive at a central difference equation for our eigenfunctions

$$\frac{f_{j+1}^n - 2f_j^n + f_{j-1}^n}{a^2} + k_{n,j} f_j^n = 0, \tag{4.13}$$

where $k_{n,j}a^2 = \frac{2t+E^n-V_j}{t}$. If V_j is constant $\forall j$ and $E^n - V_j + 2t \geq 0$ then $f_j^n = \sin(k_n x_j)$, where $x_j = ja$ and

$$E^n = -2t\left(1 - \frac{k_n^2 a^2}{2}\right). \tag{4.14}$$

In the continuum limit, $t \to \infty$ as $a \to 0$ such that $ta^2 \to \hbar^2/2m$, we have

$$E = \frac{\hbar^2 k^2}{2m} - 2t. \tag{4.15}$$

This expression for the energy is only valid for $k \ll 1$. To find an expression valid for the entire band we return to Eq. (4.12) where our goal is to solve for E^n where once again we consider $V_j = 0\ \forall j$. We start by looking for eigenfunctions that obey $f_{i+j} = f_i f_j$. Once we assume this then we know $f_0^n = 1$, $f_{-i} = (f_i^n)^{-1}$, and $\frac{\delta f_j^n}{\delta j} = \alpha_n f_j^n$ which tells us that $f_j^n = e^{i\alpha_n j}$. Equation (4.12) can now be written as

$$E^n = -t\left(e^{i\alpha_n} + e^{-i\alpha_n}\right) = -2t\cos(\alpha_n). \tag{4.16}$$

To determine what α_n is we turn back to Eq. (4.14)

$$-2t\left(1 - \frac{\alpha_n^2}{2}\right) = -2t\left(1 - \frac{k_n^2 a^2}{2}\right) \Rightarrow \alpha_n = k_n a. \tag{4.17}$$

As a closely related problem we now look at what are the properties of a staggered state which is defined by $|\phi^n\rangle = \sum_j f_j^n (-1)^j |j\rangle$. By following the same procedure we find the recursion relation for this state to be

$$t\left(f_{j+1}^n + f_{j-1}^n\right) - E^n f_j^n = 0. \tag{4.18}$$

Where we have set $V_j = 0$ and once again we find $f_j^n = \sin(k_n j)$ and $E^n = 2t\cos(k_n a)$ where for this case $E^n \le 2t$. The extension to higher dimensions is straight forward. In the following sections we will solve Eq. (4.11) with two different potentials that depend on the lattice position in a non-trivial manner. In the first section we will return the problem of the single exciton and we will show that our results confirm our previous results from momentum space where as the separation distance between the layers increases the exciton wave function spreads out. In the second section we will deal with the creation of bound states using a repulsive potential.

4.2.1 Single Exciton

> That theory is worthless. It isn't even wrong! (Wolfgang Pauli)

To address the problem of a single exciton on a lattice we will consider a square lattice where an electron can hop from one lattice point to another. We will then have a second lattice positioned directly under the first, separated by a distance d, with an attractive potential centered at the middle of the lattice. The attractive potential, that we will use in Eq. (4.11), is the Coulomb potential given by

$$V_i = -\frac{1}{\sqrt{|\mathbf{r}_i - \mathbf{r}_c| + d^2}}, \tag{4.19}$$

where $\mathbf{r}_i$ is the position vector of site i, $\mathbf{r}_c$ is the position vector for the center of the lattice. In Fig. 4.3 we show the result of the calculation of the single exciton for two values of the separation distance, d. Each calculation is performed on a lattice that contains 31 × 31 lattice points. What these images show is that as the separation distance is increased the width of the bound state wave-function increases. This behavior was already shown in the previous chapter where the momentum space wave-function became narrower as the distance was increased.

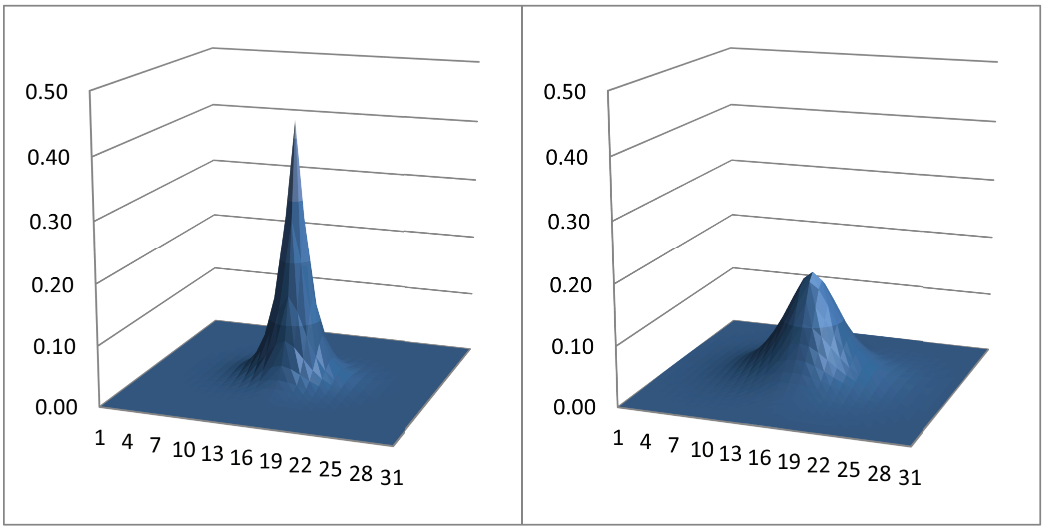

Fig. 4.3.: Plots of the normalized and dimensionless single exciton bound state wave-function for a lattice of 31 × 31 points where the attractive potential is located at the center of the lattice but displaced by a distance d perpendicular to the lattice. The left panel shows the wave-function for $d = 0.5$ and the right for $d = 2.0$. As is expected for increasing values of d the width of the bound state wave-function increases in a agreement with the momentum space results of the previous chapter.

4.2.2 Repulsive Potential Bound States

> A science is any discipline in which the fool of this generation can go beyond the point reached by the genius of the last generation.
>
> (Max Gluckman)

An interesting consequence of the presence of the lattice, or in other words the presence of a periodic potential, is the possible existence of one or more bound states for a repulsive potential. In Fig. 4.4 we show the results of the real space lattice calculations for a lattice of 31 × 31 points, using Eq. (4.11), for both an attractive and repulsive on-site interaction. This type of interaction models a single lattice point impurity and as such corresponds to the problem of a single 2D delta function potential in the continuum limit for the attractive interaction. There is of course no corresponding bound state for the repulsive interaction in the continuum limit since there is no energy band to impose an upper limit on the particle energies. The left hand panel shows the results for the attractive interaction and the right hand side shows the results for the repulsive interaction. Both plots show a slice through the bound state where the center position is the maximum of the state. As can be seen when comparing the states is that the bound state of the repulsive potential is bounded by an envelope that is identical to the bound state for the attractive potential.

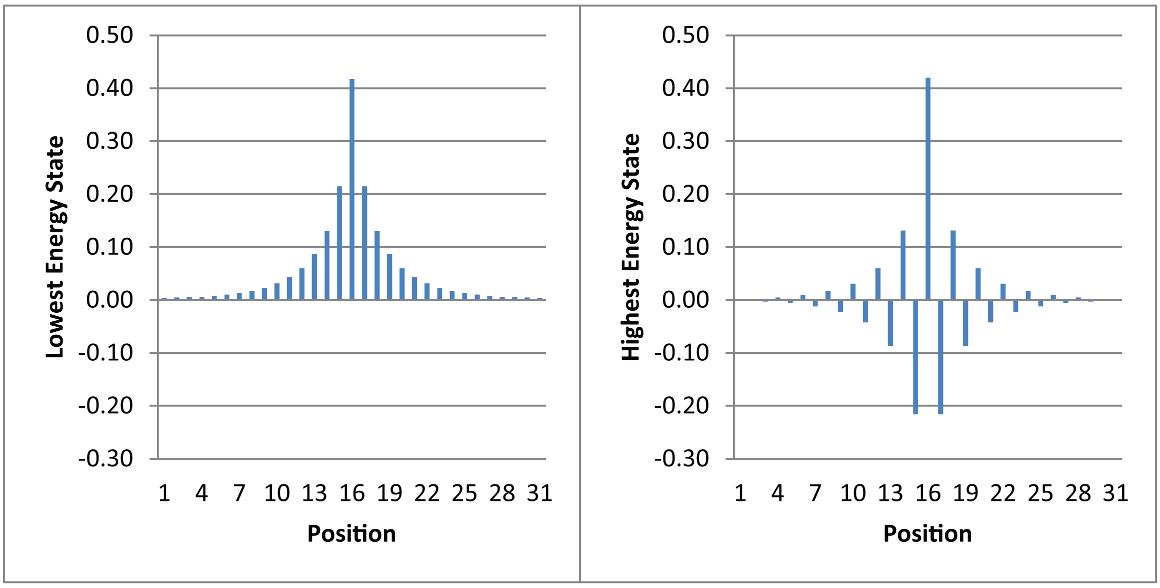

Fig. 4.4.: Results for a real space square lattice of 31×31 points and an attractive (left) and repulsive (right) on-site interaction showing that the highest energy state for the repulsive potential (right) is bounded by an envelope that is identical to the lowest energy state for the attractive potential. For both images the interlayer tunneling is $t = -1.0$ and the magnitude of the on-site interaction is $|\lambda| = 2.0$.

4.3 Conclusions

> The most exciting phrase to hear in science, the one that heralds new discoveries, is not "Eureka!" ("I found it!") but rather "hmm....that's funny..." (Isaac Asimov)

In this chapter we have derived the equations and discussed/presented the procedure for performing the Hartree-Fock approximation in the context of a system consisting of two planes of graphene separated by a distance d. By using these equations we have have presented the results of calculations for a non-interacting system with a finite but non-zero tunneling between layers. As is expected we find that the exciton density scales proportionally to the interlayer tunneling amplitude $t_{\perp}$.

We have also shown that the real space wave function for a single exciton spreads out as the separation distance between the layers is increased in agreement with our momentum space calculations.

Finally we have shown that by including a periodic potential a repulsive on-site interaction may produce one or more bound states. This bound states has an energy that is equal to $-E_b$ where E_b is the bound state energy for the attractive potential with the same strength.

5. SUMMARY

> If we knew what it was we were doing, it would not be called research, would it? (Albert Einstein)

In this thesis we have presented complementary solutions to the problems of exciton condensation and bound states. We began, in chapter 2, by deriving the mean-field equations for exciton condensation in a system of two layers of quadratically dispersing charge carriers. While doing this we noted that the iterative equation used to determine the renormalized single particle energy is essentially the Schrödinger equation in momentum space. We next extended the solution for the two dimensional hydrogen atom to the double layer exciton problem with layer separations greater than zero. By doing this we are able to give a quantitative measure of when a system of excitons is dilute enough to be considered non-interacting.

In the following sections we turned to considering exciton condensation in double layer graphene. Our goal here was to better understand the role that electron-electron screening plays in suppressing the condensate. The literature contains calculations that have been performed in the absence of screening that indicate that excitons in graphene could condense at room temperature. At the same time there are calculations that show that under certain assumptions the effects of screening should suppress the condensate critical temperature to mK. As a result of these assumptions the condensate is shown to be exponential suppressed by the number of species of electrons in the system. By using the mean-field equations, in the context of the random phase approximation, we have shown that while the condensate is suppressed by increasing the number of species of electrons the suppression is not exponential in nature.

In chapter 3 we presented the procedure for using momentum space to solve the Schrödinger equation with potentials that are not typically included in quantum mechanics courses. In addition to increasing the class of potentials that are solvable, this procedure also avoids the problems of stability that are present in trying to discretize the equation in real space. Finally we presented demonstrations of how to use this method with the mathematics program Mathematica as well as we have developed a modular program that attempts to expose students to programming while at the same time removing the technical numerical details that are not essential to the understanding of the underlying physics.

Finally in the last chapter we once again return the problems of exciton condensation and bound states but this time we solve the equations in real space. In the first section we develop the equations and procedures to perform the Hartree-Fock approximation for double layer graphene. As a first step we have shown the results of the calculations of a non-interacting system with a finite non-zero tunneling between the layers. As is expected, we find that our solutions show that the on-site exciton density scales proportionally with the interlayer tunneling amplitude. Future work will include the interactions within each layer as well as between the layers. We then turned to the single exciton case. In agreement with the momentum space calculations, presented in Chapter 2, we find that the bound state wave function spreads out as the distance between the layers is increased. In the last section we show that when the physical system contains a periodic potential, then there is a one-to-one correspondence between the bound states for an attractive and repulsive on-site interaction.

LIST OF REFERENCES

LIST OF REFERENCES

[1] S. N. Bose, "Plancks Gesetz und Lichtquantenhypothese," *Z. Phys.*, vol. **26**, 1924.

[2] A. Einstein, "Quantentheorie des einatomigen idealen gases," *Sitzungsberichte der Preussischen Akademie der Wissenschaften*, vol. **1**, 1925.

[3] M. H. Anderson, J. R. Ensher, M. R. Matthews, C. E. Wieman, and E. A. Cornell, "Observation of Bose-Einstein Condensation in a Dilute Atomic Vapor," *Science*, vol. **269**, no. 5221, pp. 198–201, 1995.

[4] K. B. Davis, M. O. Mewes, M. R. Andrews, N. J. van Druten, D. S. Durfee, D. M. Kurn, and W. Ketterle, "Bose-Einstein Condensation in a Gas of Sodium Atoms," *Phys. Rev. Lett.*, vol. **75**, no. 22, pp. 3969–3973, 1995.

[5] C. C. Bradley, C. A. Sackett, and R. G. Hulet, "Bose-Einstein Condensation of Lithium: Observation of Limited Condensate Number," *Phys. Rev. Lett.*, vol. **78**, no. 6, pp. 985–989, 1997.

[6] D. G. Fried, T. C. Killian, L. Willmann, D. Landhuis, S. C. Moss, D. Kleppner, and T. J. Greytak, "Bose-Einstein Condensation of Atomic Hydrogen," *Phys. Rev. Lett.*, vol. **81**, no. 18, pp. 3811–3814, 1998.

[7] M. R. Andrews, D. M. Kurn, H. J. Miesner, D. S. Durfee, C. G. Townsend, S. Inouye, and W. Ketterle, "Propagation of Sound in a Bose-Einstein Condensate," *Phys. Rev. Lett.*, vol. **79**, no. 4, pp. 553–556, 1997.

[8] H. J. Miesner, D. M. Stamper-Kurn, M. R. Andrews, D. S. Durfee, S. Inouye, and W. Ketterle, "Bosonic Stimulation in the Formation of a Bose-Einstein Condensate," *Science*, vol. **279**, no. 5353, pp. 1005–1007, 1998.

[9] D. M. Stamper-Kurn, A. P. Chikkatur, A. Gorlitz, S. Inouye, S. Gupta, D. E. Pritchard, and W. Ketterle, "Excitation of Phonons in a Bose-Einstein Condensate by Light Scattering," *Phys. Rev. Lett.*, vol. **83**, no. 15, pp. 2876–2879, 1999.

[10] S. L. Cornish and D. Cassettari, "Recent progress in Bose-Einstein condensation experiments," *Phil. Trans. R. Soc. Lond. A*, vol. **361**, pp. 2699–2713, 2003.

[11] E. A. Donley, N. R. Claussen, S. L. Cornish, J. L. Roberts, E. A. Cornell, and C. E. Wieman, "Dynamics of collapsing and exploding Bose-Einstein condensates," *Nature*, vol. **412**, pp. 295–299, 2001.

[12] K. E. Strecker, G. B. Patridge, A. G. Truscott, and R. G. Hulet, "Formation and Propagation of Matter Wave Soliton Trains," *Nature*, vol. **417**, pp. 150–153, 2002.

[13] L. Khaykovich, F. Schreck, G. Ferrari, T. Bourdel, J. Cubizolles, L. D. Carr, Y. Castin, and C. Salomon, "Formation of a Matter-Wave Bright Soliton," *Science*, vol. **296**, no. 5571, pp. 1290–1293, 2002.

[14] L. Deng, E. W. Hagley, J. Wen, M. Trippenbach, Y. Band, P. S. Julienne, J. E. Simsarian, K. Helmerson, S. L. Rolston, and W. D. Phillips, "Four-wave mixing with matter waves," *Nature*, vol. **398**, pp. 218–220, 1999.

[15] J. Stenger, S. Inouye, A. P. Chikkatur, D. M. Stamper-Kurn, D. E. Pritchard, and W. Ketterle, "Bragg Spectroscopy of a Bose-Einstein Condensate," *Phys. Rev. Lett.*, vol. **82**, no. 23, pp. 4569–4573, 1999.

[16] P. W. Phillips, *Advanced solid state physics*. Boulder, CO: Westview Press, 2003.

[17] W. Ketterle, D. S. Durfee, and D. M. Stamper-Kurn, "Making, probing and understanding Bose-Einstein condensates," in *Proceedings of the International School of Physics* (M. Inguscio, S. Stringari, and C. E. Wieman, eds.), (Amsterdam), pp. 67–176, IOS Press, 1999.

[18] W. Y. Liang, "Excitons," *Phys. Educ.*, vol. **5**, no. 4, pp. 226–228, 1970.

[19] J. Frankel, "On the Transformation of light into Heat in Solids. i," *Phy. Rev.*, vol. **37**, no. 1, 1931.

[20] W. Kohn, *Advanced Solid State Physics*. New York, NY: Academic, 1957.

[21] L. J. Sham and T. M. Rice, "Many-Particle Derivation of the Effective-Mass Equation for the Wannier Exciton," *Phys. Rev.*, vol. **144**, no. 2, pp. 708–714, 1966.

[22] R. S. Knox, *Theory of Excitons*. New York, NY: Academic Press, 1963.

[23] K. Matsuda, T. Saiki, S. Nomura, M. Mihara, Y. Aoyagi, S. Nair, and T. Takagahara, "Near-Field Optical Mapping of Exciton Wave Function in a GaAs Quantum Dot," *Phys. Rev. Lett.*, vol. **91**, no. 17, p. 177401, 2003.

[24] A. A. High, E. E. Novitskaya, L. V. Butov, M. Hanson, and A. C. Gossard, "Control of Exciton Fluxes in an Excitonic Integrated Circuit," *Science*, vol. **321**, no. 5886, pp. 229–231, 2008.

[25] S. J. Moss and A. Ledwith, *The Chemistry of the Semiconductor Industry*. New York, NY: Chapman and Hall, 1987.

[26] Benjah-bmm27, "http://en.wikipedia.org/wiki/file:gallium-arsenide-unit-cell-3d-balls.png," 2007.

[27] Inductiveload, "http://en.wikipedia.org/wiki/file:brillouin_zone_(1st,_fcc).svg," 2008.

[28] S. Adachi, "GaAs, AlAs, and AlxGa1-xAs@B: Material parameters for use in research and device applications," *J. Appl. Phys*, vol. **58**, no. 3, pp. R1–R30, 1985.

[29] W. Kohn and L. J. Sham, "Self-consistent equations including exchange and correlation effects," *Phys. Rev.*, vol. **140**, no. 4A, pp. A1133–A1138, 1965.

[30] M. Schluter and L. J. Sham, "Density functional theory," *Phys. Today*, vol. **35**, no. 2, pp. 36–43, 1982.

[31] R. O. Jones and O. Gunnarsson, "The density functional formalism, its applications and prospects," *Rev. Mod. Phys.*, vol. **61**, no. 3, pp. 689–746, 1989.

[32] J. W. Negele and H. Orland, *Quantum Many-Particle Systems.* Westview Press, 1998.

[33] P. B. Littlewood and X. Zhu, "Possibilities for exciton condensation in semiconductor quantum-well structures," *Phy. Scrip.*, vol. **56**, no. T68, pp. 56–67, 1996.

[34] C. H. Zhang and Y. N. Joglekar, "Exciton condensation of massless fermions in graphene," *Phys. Rev. B*, vol. **77**, no. 23, p. 233405, 2008.

[35] X. L. Yang, M. Lieber, and F. T. Chan, "The Runge-Lenz vector for the two dimensional hydrogen atom," *Am. J. Phys.*, vol. **59**, pp. 231–232, 1991.

[36] L. D. Landau and E. Lifshitz, *Quantum Mechanics.* New York, NY: Pergamon, 1981.

[37] W. A. Karr, C. R. Jamell, and Y. N. Joglekar, "Numerical approach to the Schrödinger equation in momentum space," *Am. J. Phys.*, vol. **78**, no. 4, pp. 407–411, 2010.

[38] H. Petroski, *The Pencil: A History of Design and Circumstance.* New York, NY: Knopf, 1989.

[39] P. R. Wallace, "The Band Theory of Graphite," *Phy. Rev.*, vol. **71**, no. 9, pp. 622–634, 1947.

[40] A. K. Geim and P. Kim, "Carbon Wonderland," *Scientific American*, April 2008.

[41] K. S. Novoselov, A. K. Geim, S. V. Morozov, D. Jiang, Y. Zhang, S. V. Dubonos, I. V. Grigorieva, and A. A. Firsov, "Electric field effect in atomically thin carbon films," *Science*, vol. **306**, no. 5296, pp. 666–669, 2004.

[42] N. D. Mermin, "Crystalline Order in Two Dimensions," *Phy. Rev.*, vol. **176**, no. 1, pp. 250–254, 1968.

[43] R. E. Peierls *Helv. Phys. Acta*, vol. **7**, no. 81, 1923.

[44] L. D. Landau, "Theory of phase transformation. I," *Phys. Z. Sowjet*, vol. **11**, no. 26, 1937.

[45] A. K. Geim and A. H. MacDonald, "Graphene: Exploring carbon flatland," *Physics Today*, vol. **60**, no. 35, pp. 35–41, 2007.

[46] G. W. Semenoff, "Condensed-Matter Simulation of a Three-Dimensional Anomaly," *Phys. Rev. Lett.*, vol. **53**, no. 26, pp. 2449–2452, 1984.

[47] P. Avouris, Z. Chen, and V. Perebeinos, "Carbon-based electronics," *Nature Nanotechnology*, vol. **2**, pp. 605–615, 2007.

[48] A. H. C. Neto, F. Guinea, and N. M. R. Peres, "Drawing conclusions from graphene," *Phys. World*, vol. **19**, no. 53, pp. 33–37, 2006.

[49] M. I. Katsnelson, K. S. Novoselov, and A. K. Geim, "Chiral tunnelling and the Klein paradox in graphene," *Nature Physics*, vol. **2**, pp. 620–625, 2006.

[50] H. Min, R. Bistritzer, J. Su, and A. H. MacDonald, "Room-temperature superfluidity in graphene bilayers," *Phys. Rev. B*, vol. **78**, no. 12, p. 121401, 2008.

[51] M. J. Gilbert and J. Shumway, "Probing quantum coherent states in bilayer graphene," *Journal of Computational Electronics*, vol. **8**, no. 2, pp. 51–59, 2009.

[52] M. Y. Kharitonov and K. B. Efetov, "Electron screening and excitonic condensation in double-layer graphene systems," *Phys. Rev. B*, vol. **78**, no. 24, p. 241401, 2008.

[53] L. H. Thomas in *Proc. Cambridge Philos. Soc.*, vol. **23**, 1927.

[54] E. Fermi *Z. Phys.*, vol. **48**, no. 73, 1928.

[55] J. K. Lindhard *Dan. Vidensk. Selsk. Mat.-Fys. Medd.*, vol. **28**, no. 8, 1954.

[56] H. A. Kramers, "La diffusion de la lumiere par les atomes," in *Atti Cong. Intern. Fisica*, vol. **2**, 1927.

[57] R. de L. Kronig, "On the theory of the dispersion of X-rays.," *J. Opt. Soc. Am.*, vol. **12**, 1926.

[58] H. Friedel *Adv. Phys.*, vol. **3**, 1954.

[59] W. Kohn and J. M. Luttinger, "New Mechanism for Superconductivity," *Phys. Rev. Lett.*, vol. **15**, no. 12, pp. 524–526, 1965.

[60] D. J. Griffiths, *Introduction to Quantum Mechanics.* Englewood Cliffs, NJ: Prentice Hall, 2004.

[61] E. Merzbacher, *Quantum Mechanics.* Hoboken, NJ: John Wiley & Sons, 1998.

[62] E. Kreyszig, *Advanced Engineering Mathematics.* Hoboken, NJ: John Wiley & Sons, 2006.

[63] P. Dennery and A. Krzywicki, *Mathematics for Physicists.* Mineola, NY: Dover, 1995.

[64] P. C. Chow, "Computer solutions to the Schrödinger equation," *Am. J. Phys.*, vol. **40**, no. 5, pp. 730–734, 1972.

[65] R. H. Landau, M. J. Paez, and C. C. Bordeianu, *A Survey of Computational Physics.* Princeton, NJ: Princeton University Press, 2008.

[66] E. C. Titchmarsh, "Some eigenfunction expansion formulae," *Proc. London Math. Soc.*, vol. 11, pp. 159–168, 1960.

[67] J. J. Sakurai, *Modern Quantum Mechanics.* Reading, MA: Addison-Wesley, 1995.

[68] A. Goldberg, H. M. Schey, and J. L. Schwartz, “One-dimensional scattering in configuration space and momentum space,” *Am. J. Phys.*, vol. **36**, no. 5, pp. 454–455, 1968.

[69] M. Lieber, “Quantum mechanics in momentum space: An illustration,” *Am. J. Phys.*, vol. **43**, no. 6, pp. 486–491, 1975.

[70] L. D. Landau and E. M. Lifshitz, *Quantum Mechanics(Non-Relatavistic Theory)*. Burlington, MA: Butterworth-Heinemann, 2005.

[71] J. F. Perez and F. A. B. Coutinho, “Schrodinger equation in two dimensions for zero range potential and a uniform magentic field: An exactly solvable model,” *Am. J. Phys.*, vol. **59**, pp. 52–54, 1991.

[72] S. Nyeo, “Regularization methods for delta-function potential in two-dimensional quantum mechanics,” *Am. J. Phys.*, vol. **68**, no. 6, pp. 571–575, 2000.

[73] J. W. Huang and A. Kozycki, “Hydrogen atom in two dimensions,” *Am. J. Phys.*, vol. **47**, no. 11, pp. 1005–1006, 1979.

[74] L. E. Blumenson, “A derivation of n-dimensional spherical coordinates,” *Am. Math. Monthly*, vol. **67**, no. 1, pp. 63–66, 1960.

APPENDICES

A. APPENDIX

The graphical user interface that was developed for all the calculations for the problem of exciton condensation in momentum space that were presented in this thesis is shown in Fig. A.1.

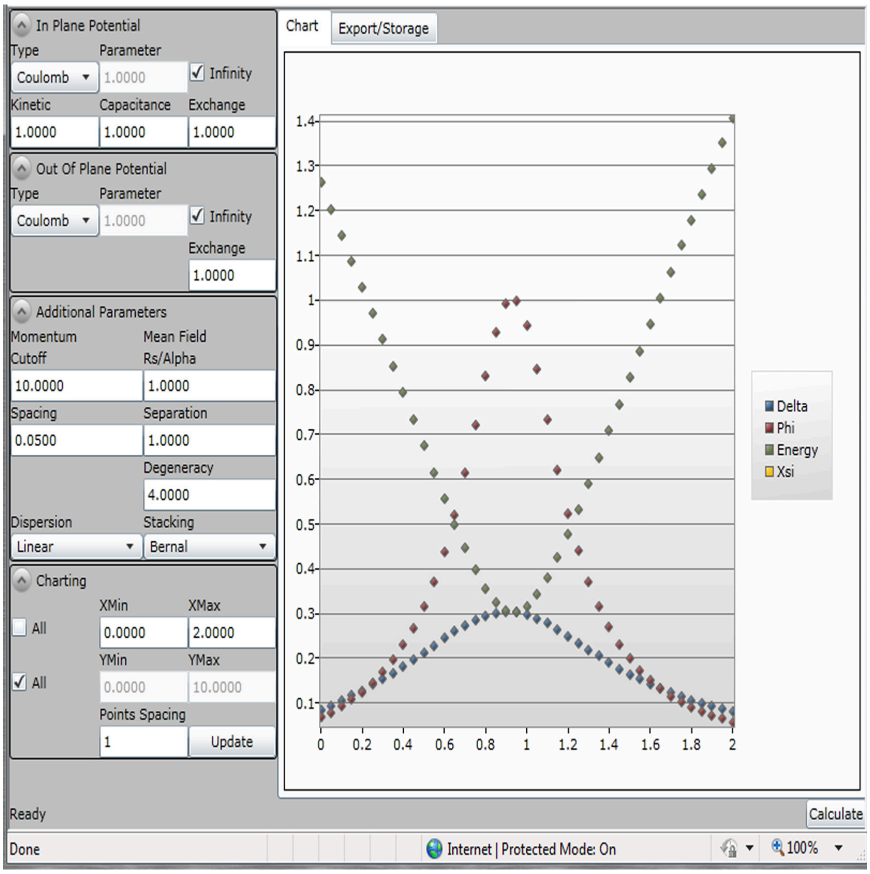

In Plane Potential
Type: Coulomb
Parameter: 1.0000
☑ Infinity
Kinetic: 1.0000
Capacitance: 1.0000
Exchange: 1.0000

Out Of Plane Potential
Type: Coulomb
Parameter: 1.0000
☑ Infinity
Exchange: 1.0000

Additional Parameters
Momentum Cutoff: 10.0000
Mean Field Rs/Alpha: 1.0000
Spacing: 0.0500
Separation: 1.0000
Degeneracy: 4.0000
Dispersion: Linear
Stacking: Bernal

Charting
☐ All XMin: 0.0000 XMax: 2.0000
☑ All YMin: 0.0000 YMax: 10.0000
Points Spacing: 1

Ready
Done
Internet | Protected Mode: On
100%

Fig. A.1.: Image of the graphical user interface used for the calculations of exciton condensation in momentum space. The interface provides a way to change between linear and quadratic dispersions, the type of stacking for the linear case, and several potentials to account for the effects of screening.

The interface allows for the user to change a fair number of parameters and to graphically explore the results before exporting for use in plotting programs such as GnuPlot. The application itself is a Silverlight web browser plugin which allows for it to be used cross-platform on both Windows and Mac machines and the underlying code used for the calculations is written in C#.

Some of the major parameters that the user is able to adjust are changing from calculations for the quadratically dispersing case, which is applicable to double quantum wells, to the linearly dispersing case for graphene. For the linearly dispersing case the user is also able to specify the type of stacking where the choices are either Bernal or hexagonal. In addition to these specifications the user is also able to choose the type of in-plane and interlayer interaction and a length parameter associated with that interaction so that the calculation can be performed for the bare Coulomb as well as screened potentials. In Fig. A.1 the output on the right shows the self-consistent exciton energy gap $\Delta_{\mathbf{k}}$, quasiparticle energy $E_{\mathbf{k}}$, the Wannier exciton wavefunction $\psi_{\mathbf{k}} = \Delta_{\mathbf{k}}/E_{\mathbf{k}}$ and the single particle energy $\xi_{\mathbf{k}}$. As was mentioned in the Introduction, the use of an interface allows the calculations to be performed by a user who is not yet ready to understand how to derive the equations and implement them in code but is nevertheless capable of understanding and analyzing the solutions. Full help documentation is included with the source code and executable contained in the accompanying media.

B. APPENDIX

In this appendix we show a program written for the purpose of involving students in the development of modules to solve the momentum space Schrödinger equation for a given potential through discretization. The underlying language of the program is C# and the interface is created using Windows Presentation Foundation. Shown in Fig. B.1 is the code, written in C#, with a single line highlighted by a yellow arrow.

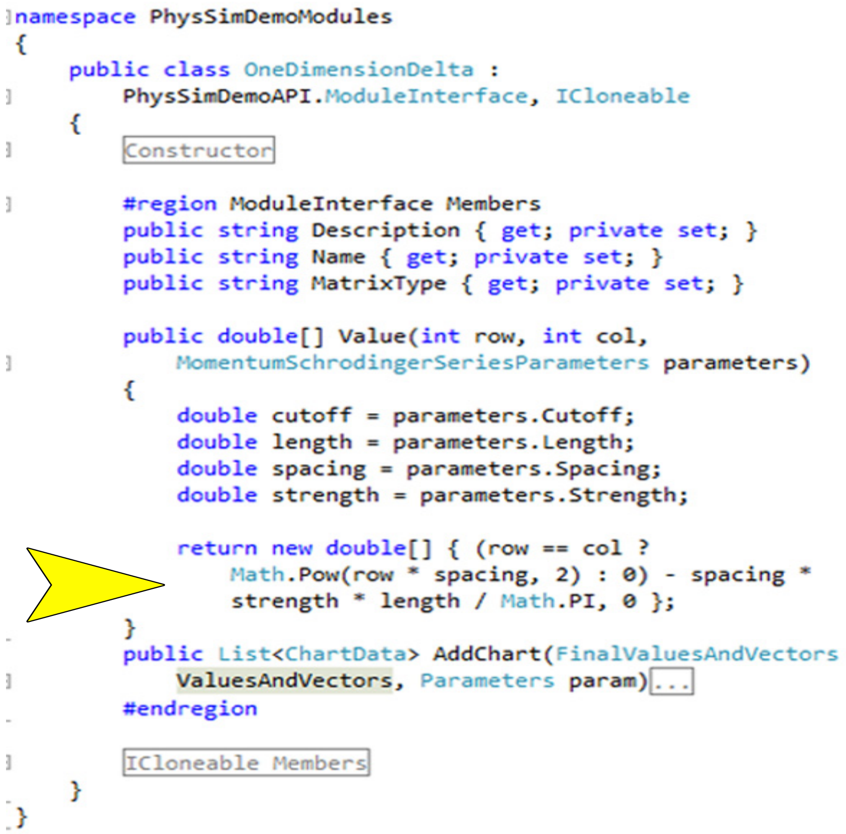

```
namespace PhysSimDemoModules
{
    public class OneDimensionDelta :
        PhysSimDemoAPI.ModuleInterface, ICloneable
    {
        Constructor

        #region ModuleInterface Members
        public string Description { get; private set; }
        public string Name { get; private set; }
        public string MatrixType { get; private set; }

        public double[] Value(int row, int col,
            MomentumSchrodingerSeriesParameters parameters)
        {
            double cutoff = parameters.Cutoff;
            double length = parameters.Length;
            double spacing = parameters.Spacing;
            double strength = parameters.Strength;

            return new double[] { (row == col ?
                Math.Pow(row * spacing, 2) : 0) - spacing *
                strength * length / Math.PI, 0 };
        }
        public List<ChartData> AddChart(FinalValuesAndVectors
            ValuesAndVectors, Parameters param)...
        #endregion

        ICloneable Members
    }
}
```

Fig. B.1.: Figure showing the single line of code required to implement a module to calculate the eigenvalues and eigenvectors for the Schrödinger equation for a one dimensional δ-function written in C#.

The highlighted line is the single line of numerical code that is required in order to change the calculation from one potential to another. In this example the code results in the calculations being performed for a one dimensional δ-function. The process for creating a new module would be to first start with the provided module template and then add a name and description for the new module followed by then editing the highlighted line. In addition to allowing the user to determine the form of the matrix to be used during calculations there is a mechanism provided for the user to analyze, through code, the results of the calculation. In order for any numerical calculation to be of any use there must be a way to input parameters and to visualize the results.

Figure B.2 shows the home screen for a physics simulation program that we have developed.

Momentum Space

1D Delta Momentum Space ▾

	Min	Max	Inc
Cutoff	10	10	1
Length	1	1	1
Spacing	0.05	0.05	1
Strength	1	1	1

Fig. B.2.: Home screen of the physics simulation program that we have developed. In this image we see the module interface, located approximately center screen, as well as the screen selection buttons located at the bottom of the screen.

Situated approximately at the center of the image is the module interface. This is where we are able to specify potential that we will use in our calculations by choosing one of the loaded modules in the drop-down menu. Below the drop-down menu is the area for the input of parameters. For our current discussion this includes the ultraviolet cutoff, U_c, the momentum space point spacing, Δ_u, the strength of the potential, λ, and the characteristic length, l, which is optional depending on the type of potential specified. In addition to being able to input one value for these parameters the user is also able to indicate a minimum, maximum, and increment value for any or all of them which will result in the program automatically looping to perform the calculation for the desired values.

The following two figures show the output of our demonstration program for a one dimensional δ-function with $U_c = 10, \Delta u = 0.05, \lambda_1 = 1$, and $a = 1$. Figure B.3 shows the eigenvalues screen where we see, as before, that the positive energy states form a quadratic band as they should. Next we see in Fig. B.4(a) the image of the bound state eigenfunction for the one dimensional δ-function which is analogous to the bound state shown in Fig. 3.2. And finally Fig. B.4(b) shows that the eigenfunction belonging to a positive energy eigenvalue is localized in momentum space which is in agreement with Fig. 3.2.

In the beginning we mentioned that it is possible for the creator of a module to implement code that would perform data analysis on the data after the calculations were completed. Figure B.5 shows the result of just such a data analysis code. To create this image the parameters that were used were $U_c = 10, \Delta u = 0.05$, and $a = 1$, which are the same as before except that in place of a single value for the strength we use $0 \leq \lambda \leq 10$ with an increment of $\Delta\lambda = 1$. This results in the code be run ten times after which the data analysis code looks through the results and selects the bound state eigenvalues so that their magnitude can be plotted against the strength of the δ-function which is in agreement with Fig. 3.1.

Full help documentation is included with the source code and executable contained in the accompanying media.

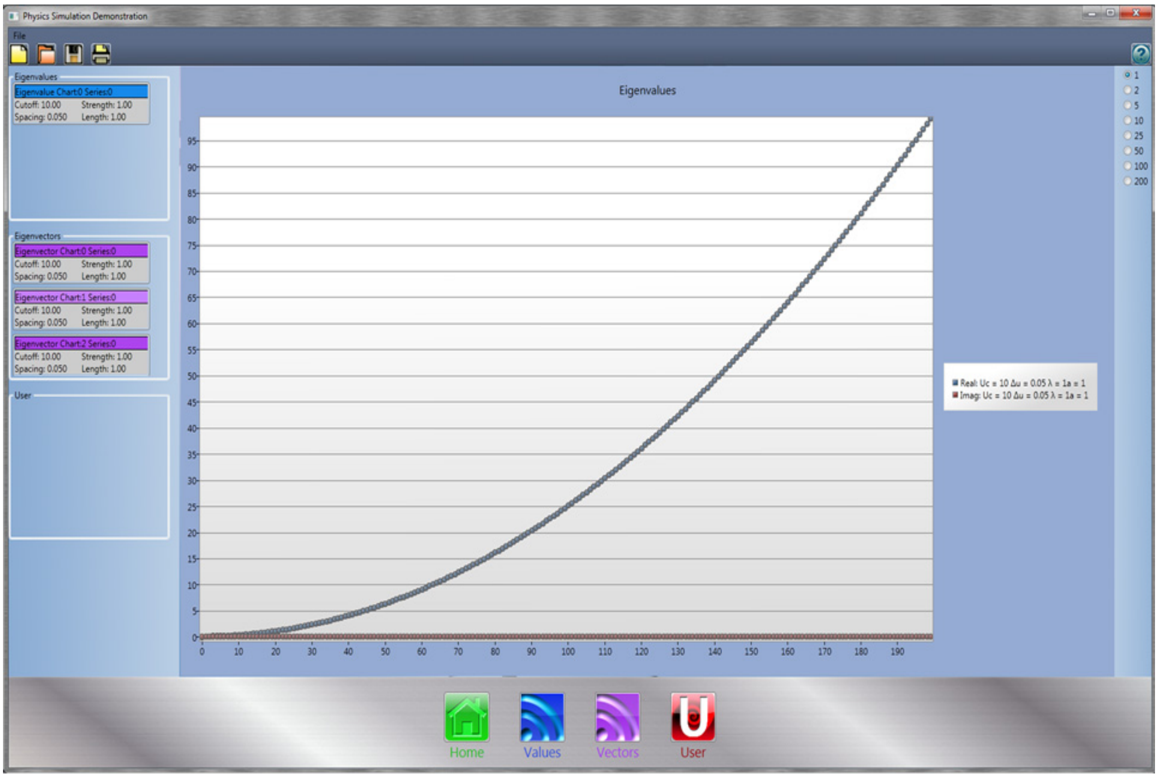

Eigenvalue Chart:0 Series:0
Cutoff: 10.00 Strength: 1.00
Spacing: 0.050 Length: 1.00

Eigenvector Chart:0 Series:0
Cutoff: 10.00 Strength: 1.00
Spacing: 0.050 Length: 1.00

Eigenvector Chart:1 Series:0
Cutoff: 10.00 Strength: 1.00
Spacing: 0.050 Length: 1.00

Eigenvector Chart:2 Series:0
Cutoff: 10.00 Strength: 1.00
Spacing: 0.050 Length: 1.00

Real: Uc = 10 Δu = 0.05 λ = 1a = 1
Imag: Uc = 10 Δu = 0.05 λ = 1a = 1

Fig. B.3.: Image showing the eigenvalues for a one dimensional δ-function with $U_c = 10, \Delta u = 0.05, \lambda_1 = 1$, and $a = 1$ parameters. As we have seen before we note that the positive energy eigenvalues form a quadratically dispersing band which is indicative of a free particle.

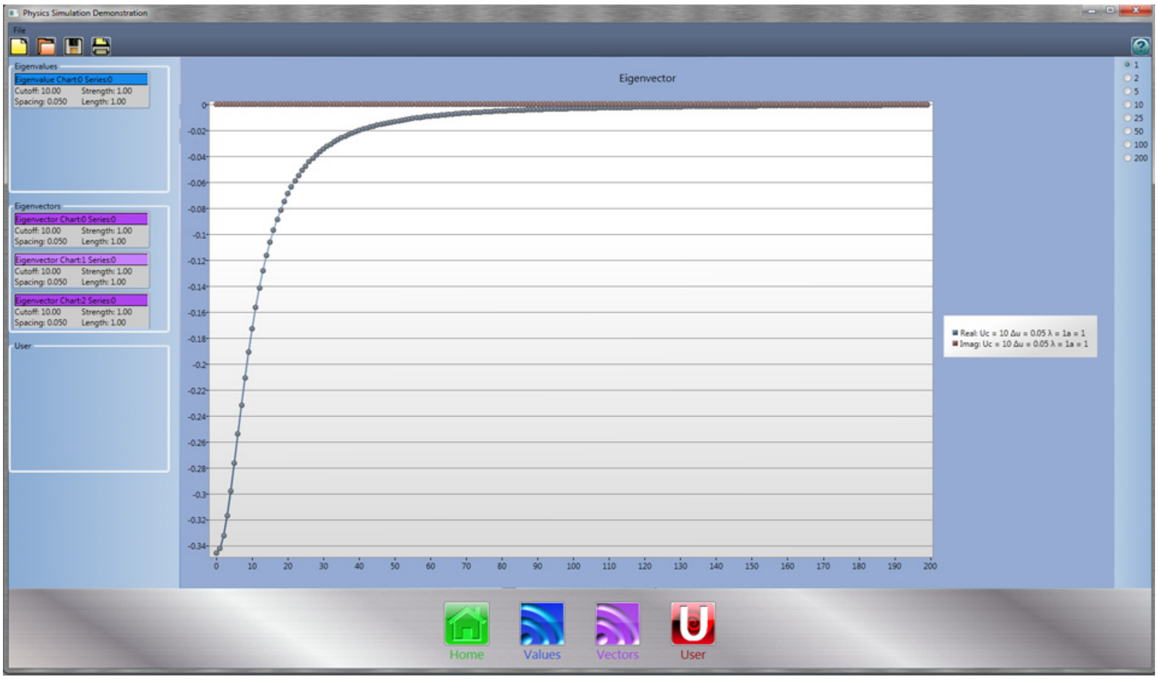

Eigenvalue Chart:0 Series:0
Cutoff: 10.00 Strength: 1.00
Spacing: 0.050 Length: 1.00

Eigenvector Chart:0 Series:0
Cutoff: 10.00 Strength: 1.00
Spacing: 0.050 Length: 1.00

Eigenvector Chart:1 Series:0
Cutoff: 10.00 Strength: 1.00
Spacing: 0.050 Length: 1.00

Eigenvector Chart:2 Series:0
Cutoff: 10.00 Strength: 1.00
Spacing: 0.050 Length: 1.00

(a)

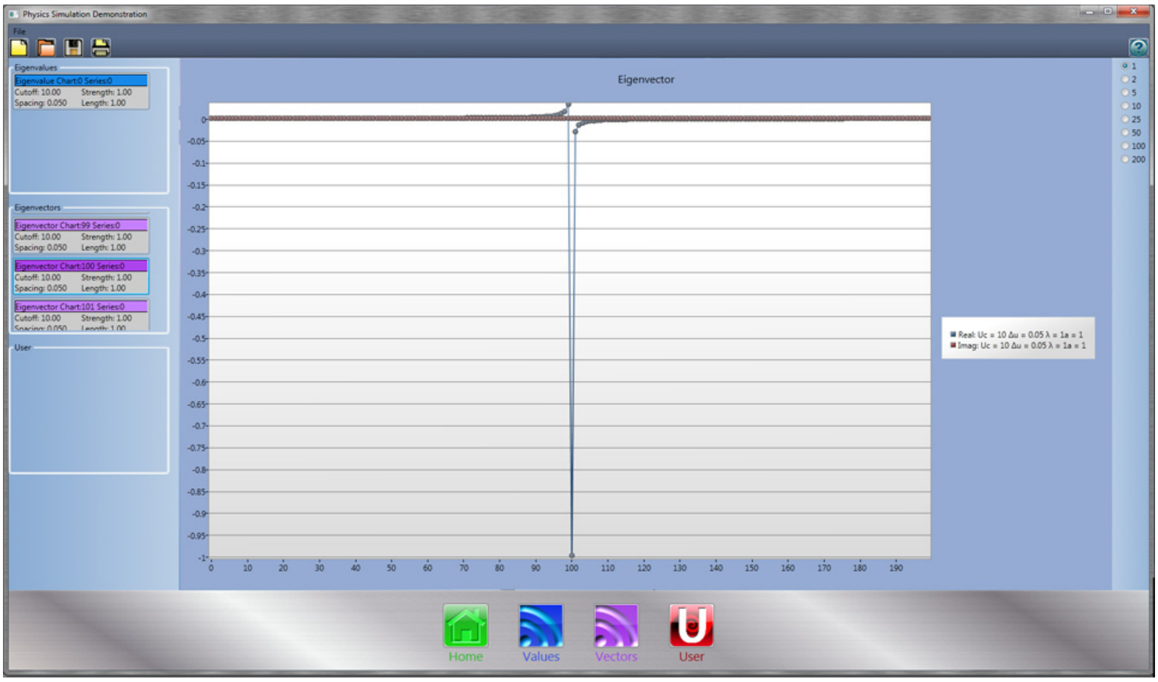

Eigenvalue Chart:0 Series:0
Cutoff: 10.00 Strength: 1.00
Spacing: 0.050 Length: 1.00

Eigenvector Chart:99 Series:0
Cutoff: 10.00 Strength: 1.00
Spacing: 0.050 Length: 1.00

Eigenvector Chart:100 Series:0
Cutoff: 10.00 Strength: 1.00
Spacing: 0.050 Length: 1.00

Eigenvector Chart:101 Series:0
Cutoff: 10.00 Strength: 1.00
Spacing: 0.050 Length: 1.00

(b)

Fig. B.4.: Images showing the eigenfunction associated with the negative eigenvalue (a) and a positive eigenvalue (b) for a one dimensional δ-function with parameters $U_c = 10, \Delta u = 0.05, \lambda_1 = 1$, and $a = 1$.

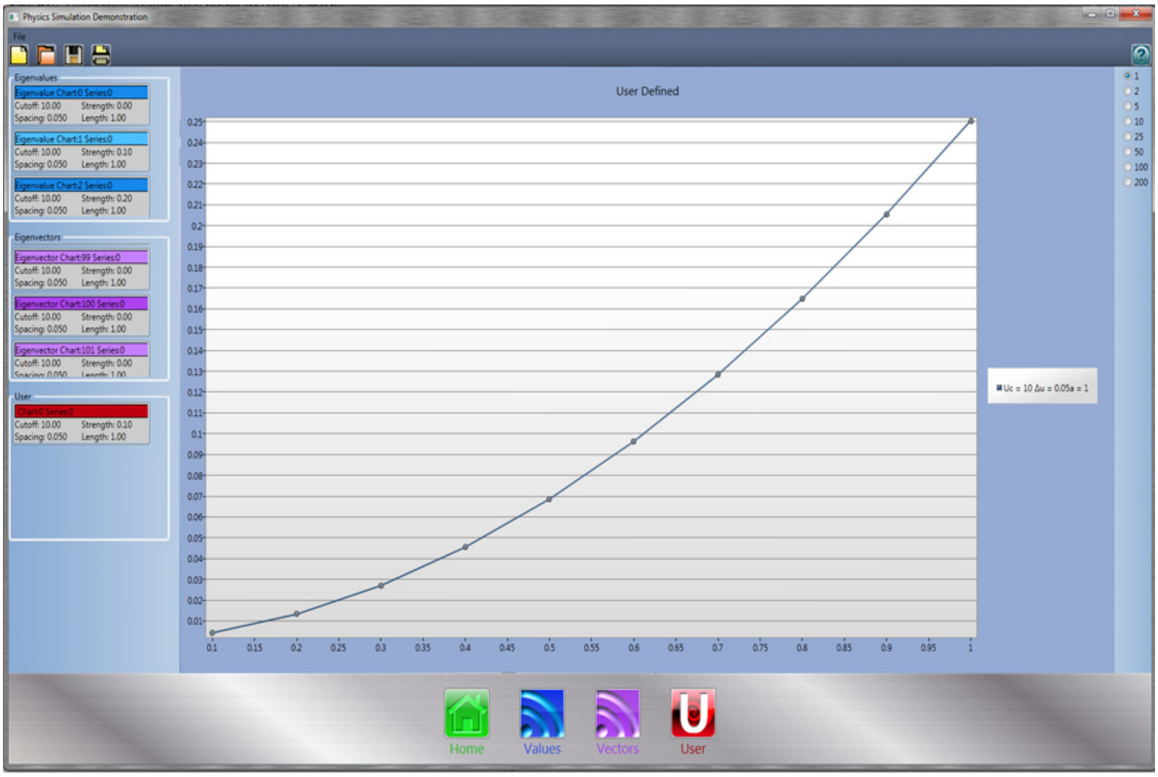

Eigenvalues

Eigenvalue Chart:0 Series:0
Cutoff: 10.00 Strength: 0.00
Spacing: 0.050 Length: 1.00

Eigenvalue Chart:1 Series:0
Cutoff: 10.00 Strength: 0.10
Spacing: 0.050 Length: 1.00

Eigenvalue Chart:2 Series:0
Cutoff: 10.00 Strength: 0.20
Spacing: 0.050 Length: 1.00

Eigenvectors

Eigenvector Chart:99 Series:0
Cutoff: 10.00 Strength: 0.00
Spacing: 0.050 Length: 1.00

Eigenvector Chart:100 Series:0
Cutoff: 10.00 Strength: 0.00
Spacing: 0.050 Length: 1.00

Eigenvector Chart:101 Series:0
Cutoff: 10.00 Strength: 0.00
Spacing: 0.050 Length: 1.00

User

Chart:0 Series:0
Cutoff: 10.00 Strength: 0.10
Spacing: 0.050 Length: 1.00

● 1
○ 2
○ 5
○ 10
○ 25
○ 50
○ 100
○ 200

Fig. B.5.: Image showing the bound state energy, $|E_b| \sim \lambda^2$, as a function of λ for $0 \leq \lambda \leq 10$ with an increment of $\Delta\lambda = 1$ for a one dimensional δ-function with $U_c = 10, \Delta u = 0.05$, and $a = 1$. The figure is a plot of the bound state energy as a function of the strength which is in agreement with Fig. 3.1

C. APPENDIX

The graphical user interface that was developed for the problem of exciton condensation in graphene double-layer systems in real space is shown in Fig. C.1.

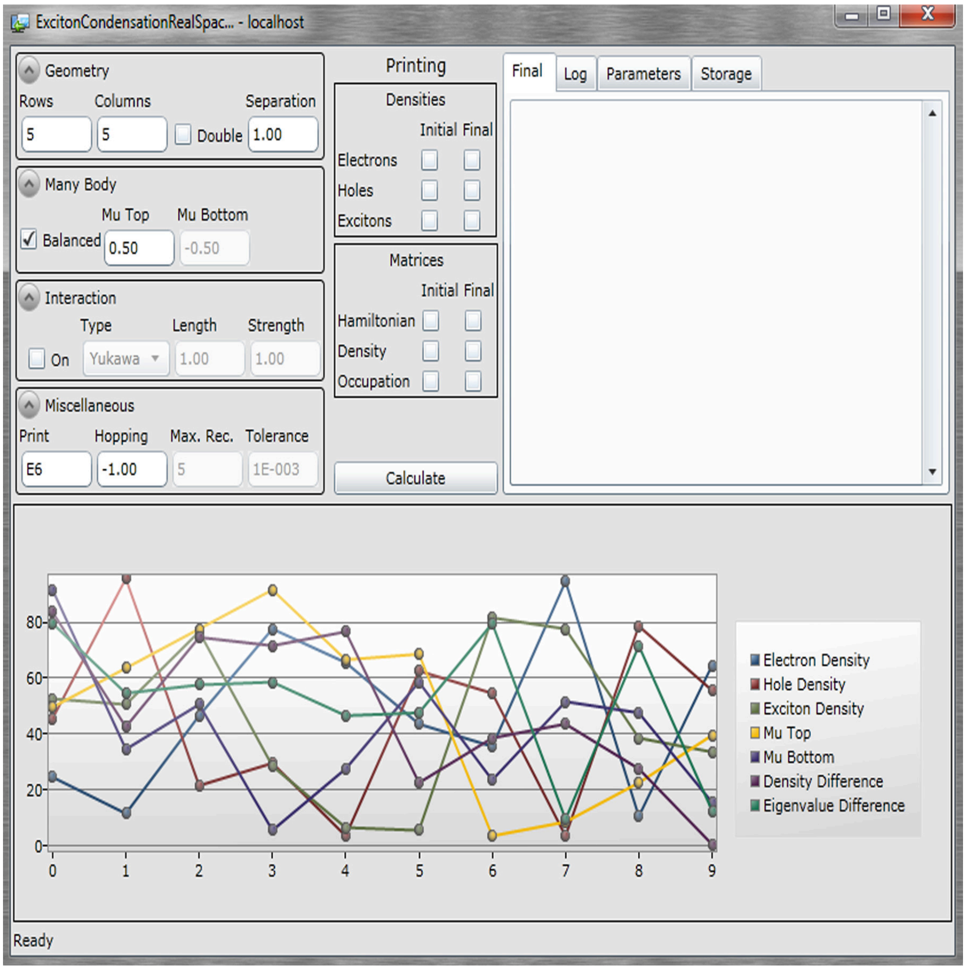

Rows 5
Columns 5
☐ Double
Separation 1.00
☑ Balanced
Mu Top 0.50
Mu Bottom -0.50
☐ On
Type Yukawa
Length 1.00
Strength 1.00
Print E6
Hopping -1.00
Max. Rec. 5
Tolerance 1E-003

Fig. C.1.: Image of the graphical user interface used for the calculations of exciton condensation in real space.

The interface allows for the user to change a fair number of parameters and export the results for use in plotting programs such as GnuPlot. The application itself is a

Silverlight web browser plugin which allows for it to be used cross-platform on both Windows and Mac machines.

Some of parameters that the user is able to adjust are the number of rows and columns in a graphene layer, the chemical potentials in each layer and the type of in-plane and interlayer interactions. The code outputs the self-consistent density matrix, $\rho_{ij}^{\alpha\beta}$, the electron density, $n_e = \frac{1}{N}\sum_i \rho_{ii}^{TT}$, the hole density, $n_e = \frac{1}{N}\sum_i \rho_{ii}^{BB}$, and the on-site exciton order parameter ρ_{ii}^{TB}. Full help documentation is included with the source code and executable contained in the accompanying media.

VITA

VITA

Christopher Jamell

EDUCATION:

- **Ph.D. in Physics**, Purdue University, Indianapolis, Indiana, anticipated Dec. 2010. DISSERTATION: *Lattice and Momentum Space Approach to Bound States and Excitonic Condensation Via User Friendly Interfaces.*
- **Master of Science in Physics**, Indiana University-Purdue University Indianapolis, IN, 2007.
- **Bachelor of Science in Physics and Mathematics**, Indiana University-Purdue University Indianapolis, IN, 2004

ACADEMIC HONORS AND AWARDS:

- **Outstanding Physics Graduate Student**: Indiana University-Purdue University Indianapolis (2010)
- **Outstanding Teaching Assistant Award**: American Association of Physics Teachers (2008)
- **Forrest Meiere Prize for Outstanding Undergraduate Physics Major**: Indiana University-Purdue University Indianapolis (2004)
- **Chancellor's Award for Outstanding Undergraduate Research**: Indiana University-Purdue University Indianapolis (2004)

TEACHING EXPERIENCE:

- **Laboratory Instructor**, **Recitation Instructor**, **Recitation Mentor**, **Mathematics Mentor**, Indiana University-Purdue University Indianapolis

PUBLICATIONS:

- **Christopher R. Jamell**, Chang-hua Zhang, Yogesh N. Joglekar. “Dilute” excitons in a double layer system: single-exciton and mean-field approach. arXiv:0910.2993 (2009)
- William A. Karr, **Christopher R. Jamell**, Yogesh N. Joglekar. Numerical approach to the Schrödinger equation in momentum space. Am. J. Phys. **78**(407) (2009)
- R. S. Decca, D. Lopez, H. B. Chan, E. Fischbach, D. E. Krause, **C. Jamell**. Constraining New Forces in the Casimir Regime Using the Isoelectronic Technique. Phys. Rev. Lett. 94 (2005)

PRESENTATIONS:

- **“The effect of screening on excitonic condensation in double-layer graphene”**. American Physical Society March Meeting 2010, Portland, Oregon
- **“Excitonic condensation with different pairing symmetries in double quantum wells”**. American Physical Society March Meeting 2009, Pittsburgh, Pennsylvania
- **“Excitons: What are they and why do we care?”**. Indiana Academy of Science Fall 2008, Evansville, Indiana
- **“Yukawa Corrections to the Gravitational Force: Effects of Finite Size Corrections”**. National Conference on Undergraduate Research 2004, Indianapolis, Indiana

INVITED DEMONSTRATION PROJECTS:

- **Bound-State Spectra for Two Delta Function Potentials**: http://demonstrations.wolfram.com/BoundStateSpectraForTwoDeltaFunctionPotentials/ (2009)

AFFILIATIONS:

- American Physical Society
- Society of Physics Students
- Golden Key International Honour Society